Biochemical and Structural Studies of Amyloid Proteins –

David Christopher Wirthensohn

Amyloidogenic neurodegenerative disorders such as Alzheimer's disease (AD) and Parkinson's disease (PD) are an important health issue. However, the underlying molecular mechanisms of the disease-related protein aggregates, that are present in humans, are only understood partially. I have used and developed biophysical methods to study the structural and biological properties of individual aggregates of Amyloid β peptide and α-Synuclein, proteins whose aggregation is associated with the development of Alzheimer's and Parkinson's disease respectively.

I expanded the single aggregate visualisation through enhancement (SAVE) technique, which is a method based on the fluorescent dye Thioflavin T (ThT) that reversibly bind to the aggregates and whose fluorescence increases upon binding. I firstly explored the use of other dyes for these experiments and found that a ThT dimer has higher affinity to α-Synuclein aggregates *in vitro*. I then applied the SAVE method to the cerebral spinal fluid (CSF) of a cohort of AD patients and control CSF and observed no clear difference in aggregate number. However, these experiments provided insights into how antibodies bind the aggregates in human CSF. I could show, that despite altering the Ca^{2+} influx into both cells and vesicles, the antibody did not measurably affect the aggregate structure.

To study the size specific effects of the Amyloid β 42 (Aβ42) peptide in more detail, I used and optimised gradient ultracentrifugation combined with single aggregate imaging to study the structural properties of the isolated aggregates. This aggregation kinetic independent method allowed me to compare the properties of fluorescently labelled and unlabelled Aβ42 and characterize the size dependent properties of aggregates in a single experiment. Since I could measure the relative concentration of different size aggregates it was also possible to compare the properties of single aggregates of different sizes. I then used biological assays to examine the ability of aggregates to permeabilise membranes resulting in the entry of calcium ions, and their ability to induce TNFα production in microglia cells. Both processes are thought to play key roles in the development of AD. I found that small soluble oligomers are most potent at inducing Ca2+ influx, whereas longer protofilaments are the most potent inducers of TNFα production. My results suggest that the mechanism by which aggregates damage cells changes as aggregation proceeds, as longer aggregates with different structures are formed. Protofilaments with a diameter of 1 nm or less have a structure that could make them particularly potent at causing the signalling of toll-like receptors, providing a molecular basis for their ability to induce TNFα production.

Biochemical and Structural Studies of Amyloid Proteins

David Christopher Wirthensohn

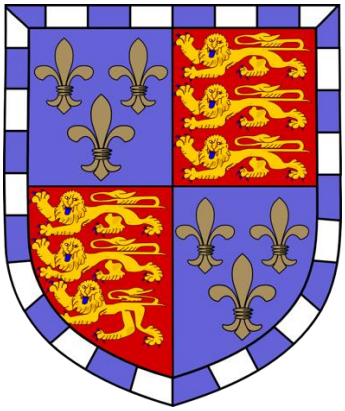

University of Cambridge

Christ's College

This dissertation is submitted for the degree of Doctor of Philosophy

Submitted July 2018

Declaration

This dissertation is the result of my own work and includes nothing which is the outcome of work done in collaboration except as declared in the Preface and specified in the text.

It is not substantially the same as any that I have submitted, or, is being concurrently submitted for a degree or diploma or other qualification at the University of Cambridge or any other University or similar institution except as declared in the Preface and specified in the text. I further state that no substantial part of my dissertation has already been submitted, or, is being concurrently submitted for any such degree, diploma or other qualification at the University of Cambridge or any other University or similar institution except as declared in the Preface and specified in the text

It does not exceed the prescribed word limit for the relevant Degree Committee of 60 000 words.

Cambridge, ...

.....

David Wirthensohn

Summary

Amyloidogenic neurodegenerative disorders such as Alzheimer's disease (AD) and Parkinson's disease (PD) are an important health issue. However, the underlying molecular mechanisms of the disease-related protein aggregates, that are present in humans, are only understood partially. I have used and developed biophysical methods to study the structural and biological properties of individual aggregates of Amyloid β peptide and α-Synuclein, proteins whose aggregation is associated with the development of Alzheimer's and Parkinson's disease respectively.

I expanded the single aggregate visualisation through enhancement (SAVE) technique, which is a method based on the fluorescent dye Thioflavin T (ThT) that reversibly bind to the aggregates and whose fluorescence increases upon binding. I firstly explored the use of other dyes for these experiments and found that a ThT dimer has higher affinity to α-Synuclein aggregates *in vitro*. I then applied the SAVE method to the cerebral spinal fluid (CSF) of a cohort of AD patients and control CSF and observed no clear difference in aggregate number. However, these experiments provided insights into how antibodies bind the aggregates in human CSF. I could show, that despite altering the Ca^{2+} influx into both cells and vesicles, the antibody did not measurably affect the aggregate structure.

To study the size specific effects of the Amyloid β 42 (Aβ42) peptide in more detail, I used and optimised gradient ultracentrifugation combined with single aggregate imaging to study the structural properties of the isolated aggregates. This aggregation kinetic independent method allowed me to compare the properties of fluorescently labelled and unlabelled Aβ42 and characterize the size dependent properties of aggregates in a single experiment. Since I could measure the relative concentration of different size aggregates it was also possible to compare the properties of single aggregates of different sizes. I then used biological assays to examine the ability of aggregates to permeabilise membranes resulting in the entry of calcium ions, and their ability to induce TNFα production in microglia cells. Both processes are thought to play key roles in the development of AD. I found that small soluble oligomers are most potent at inducing Ca^{2+} influx, whereas longer protofilaments are the most potent inducers of TNFα production. My results suggest that the mechanism by which aggregates damage cells changes as aggregation proceeds, as longer aggregates with different structures are formed. Protofilaments with a diameter of 1 nm or less have a structure that could make them particularly potent at causing the signalling of toll-like receptors, providing a molecular basis for their ability to induce TNFα production.

Acknowledgement

I would like to thank Prof. Dr. David Klenerman, FRS who made this project possible.

I would like to thank my parents Dr. Klaus and Dr. Gabi Wirthensohn and my partner Dr. Clare Henry for their support throughout. Clare, this thesis would have been infinitely harder without you.

Chapter 1 and 3 are based and are excerpts from work that I have published previously (see chapter 8) and all other acknowledgments and contributions are stated below.

I would like to acknowledge the work of Joseph Beckwith and Dr. Mike Devine who measured and helped testing new dyes and AD CSF samples with me. I would like to thank Dr. Seema Qumar, Prof. Peter St. George-Hyslop and Prof. Roger Barker for help and for providing facilities to test the CSF methods. Furthermore, I would like to acknowledge Dr. Suman De and Dr. Patrick Flagmeier who developed and preformed the single vesicle assays and provided recombinant protein. I would like to thank Dr. Anna Drews who measured the calcium influx into astrocytes. I would also like to thank Dr. Daniel Whiten who complemented some of the AD CSF SAVE measurements with. I would like to thank MedImmune, for providing antibodies to study their effects and Dr. Erwin DeGenst for the Nb3 Nanobodies and Dr. Janet Kumita and Dr. Daniel Whiten for providing clusterin. I would like to thank Dr. Damian Crowther, the director of Neuroscience, Innovative Medicines and Early Development, AstraZeneca, for discussion. I would like to thank Dr. Margarida Rodrigues for help with the immuno-depletion experiments. I would like to thank Dr. Craig Hughes for performing the TNFα measurements. I would like to thank Dr. Simone Ruggeri for the AFM measurements and AFM data analysis. I would like to acknowledge Dr. Franziska Kundel and Dr. Mathew Horrocks for advice throughout the project in all fluorescence and microscopy related issues. Dr. Mathew Horrocks furthermore provided microfluidic devices with cortical neurons in collaboration with Dr. Ragnhildur Thóra Káradótti and assisted with DNA-PAINT measurements

I would like to thank Dr. Rohan Rahnasinghe, Dr. Aleks Ponjavic and Dr. Juan Varela for invaluable and fruitful scientific and non-scientific discussions. I would like to thank all other group members not named for their support and help throughout.

1 Table of Contents

List of Abbreviations

AD	Alzheimer's Disease
µm	micro meter
AF488	Alexa Fluor 488
AF647	Alexa Fluor 647
AFM	Atomic force microscopy
ANOVA	Analysis of variance
Aß42	Amyloid beta 1-42 protein
BTA-1	2-(4'-Methylaminophenyl) benzothiazole
CR	Congo Red
CSF	Cerebral spinal fluid
DCVJ	9-(Dicyanovinyl)- julolidine
Di-ThT	Dimeric-thioflavin t
DNA-PAINT	Point accumulation for accumulation in nanoscale topography
E. coli	Escherichia coli
fov	Field of view
FRET	Förster resonance energy transfer
FTP	Frontotemporal dementia
FWHM	Full width half maximum
h	Hours(s)
IP	Immunoprecipitation
kDa	kilo Dalton
MCI	Mild cognitive impairment
min(s)	minute(s)
Nb3	Nanobody 3
NR	Nile Red
PAINT	Point accumulation for accumulation in nanoscale topography
PD	Parkinson's Disease
pFTAA	Luminescent conjugated oligothiophene
PK	Proteinase K
PLL	Poly- (L)- Lysine

POPC	1-palmitoyl-2-oleoyl-sn-glycero-3-phosphocholine
PrP	Prion protein
px	pixel
ROC	Receiver Operating Characteristic
SAVE	Single aggregate visualisation through enhancement
SBR	Signal to background ratio
SICM	Scanning ion conductance microscope
smFRET	Single molecule FRET
SN	supernatant
SR microscopy	Super resolution microscopy
ThT	Thioflavin T
TIRF	Total internal reflection fluorescence
αS	α-Synuclein

1 Introduction

An ever-ageing population has led to a great increase in neurodegenerative diseases such as Alzheimer's disease and other dementias, Parkinson's disease and others. These diseases have in common that they all adversely affect some part of the central nervous system, hence the term neurodegenerative diseases. Importantly in the last decade all these diseases have become much more common. This is accounted for by an increase in life expectancy, with age being the main risk factor for most of these neurodegenerative diseases. This obviously excludes hereditary disease as their risk factor is usually genetic and the onset is earlier than in sporadic cases of the diseases.

The WHO estimates worldwide, around 50 million people have dementia, with nearly 60 % living in low- and middle-income countries and nearly 10 million new cases every year. The total number of people with dementia is projected to reach 82 million in 2030 and 152 million in 2050 [1].

This poses a significant economic burden as these diseases require intensive nursing and care for often extended periods of time. Especially the memory impairment can not only be devastating for the patient but also for family and friends. In the case of PD, the nursing and care prospects are similar. Where PD is not associated with memory impairment the severe impairment in physical abilities calls for close supervision and help by the nursing staff.

Clinically the diagnosis in both cases is difficult and definitive only later in the progression of the disease which further complicates possible treatments. Often a definitive diagnosis of the specific clinical subtype of the disease can only be given post mortem. All these factors make the sporadic neurodegenerative diseases an ever-increasing problem in the population. This asks for better treatment and accurate diagnosis. Especially as many of the neurodegenerative diseases have very similar early clinical symptoms such as mild cognitive impairment, caused by various diseases similarly. To distinguish and recognise these symptoms and causes very early on and tailor treatment accordingly is as important as finding drugs that possible slow down, halt or even reverse progression of the disease.

The number one risk factor for non-hereditary forms of AD and PD is age. There have been some other events linked to the early onset of dementias as e.g. repeated

trauma to the head in FTD or APOε4 overexpression/ duplication in AD, but none of them can account for as much of cases other than age. The consequences, the wide spread and a generic main risk factor warrants the need for better treatment and diagnosis of these diseases.

1.1 Neurodegenerative Diseases and Amyloid Aggregation

One of the first accounts of AD and its underlying cause was the finding of amyloid plaques by Alois Alzheimer, a German physician, in 1907 [2]. He followed a patient with dementia and unique clinical symptoms and described the plaques he found on the post mortem stained brain slices [2]. The first description of Parkinson's disease was already in 1817 by James Parkinson in great detail with the identification of the Lewy-Bodies in 1912 by Fritz Heinrich Lewy who found these aggregates in some brain regions outside the substantia nigra [3,4].

With AD and PD first described over a century ago [2,3], it took over 75 years to identify the main proteinaceous components of the deposits found in these diseases: in 1985, the peptide amyloid-β (Aβ) was identified as main component of the extracellular plaques found in AD [5] and shortly thereafter neurofibrillary tangles (NFTs) were shown to primarily consist of the microtubule associated protein tau [6-9]. Subsequently, α-synuclein (αS) was identified as main component of Lewy bodies typically present in PD brains by Maria Spillantini and co-workers [10].

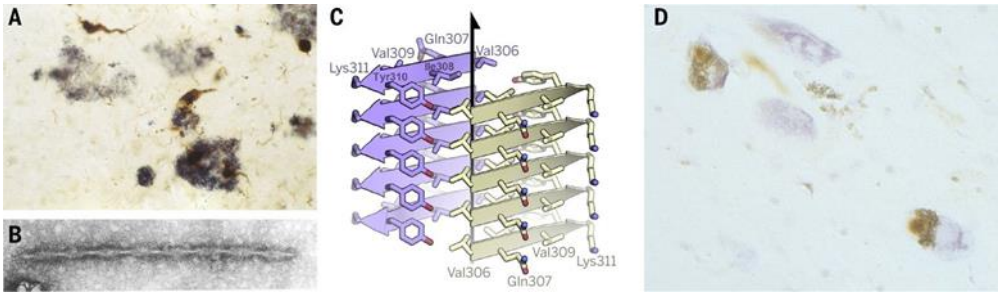

Figure 1 Histological and molecular representations of amyloid aggregates reproduced and modified from [11] (A) Light microscopic picture of Aβ plaques (blue) and neurofibrillary tau lesions (brown) in the cerebral cortex in AD. (B) Electron micrograph of a paired helical tau filament from AD. The cross-over spacing is ~80 nm. Paired helical filaments form the majority of tau filaments, with straight filaments being in the minority. [Reproduced from [12]] (C) Steric-zipper crystal structure of the hexapeptide VQIVYK (residues 306 to 311) from the core of tau filaments, which is required for aggregation. Two β-sheets are shown (gray and blue), with the β-strands being parallel within each sheet, and antiparallel between sheets (…). (D) Light microscopic picture of Lewy bodies and Lewy neurites made of α-synuclein (brown) in the substantia nigra in PD. [Reproduced from Spillantini et al. [10]

Histological sections of typical amyloid deposits of αS called Lewy bodies, of tau called neurofibrillary tangles and Aβ called amyloid plaques are shown in (Figure 1). The respective fibrillar accumulations are stained in dark blue or brown in all cases. They are all in the μm range 'growing' into substantial sizes from their monomeric components which are all below 50kDa.

These plaques and tangles contain aggregated protein. That means that a big number of monomer units are aggregated into large structures held together by hydrophobic interactions of their polypeptide chains. These aggregates usually consist of extended beta-sheet secondary structure elements in repetitive form, commonly in the shape of long fibrils. These beta-sheet structures where the ones Alois Alzheimer could stain and observe as they extend to μm dimensions.

The β-sheet aggregates have since been found to be a common occurrence in neurodegenerative diseases which exhibit progressive neuronal cell loss and the protein aggregates are present in the effected and surrounding brain areas. [4,13-15]. The presence of amyloid aggregates has been linked to more than just AD and PD since [16]. Protein aggregation has also been described as a general property of the polypeptide chain [17,18].

Amyloid aggregates typically consist of non-native protein with the unfolding or misfolding event as the start of the aggregation process. This unfolded state does not have the native configuration of the protein and is then able to self-interact. This state can be a misfolded native protein as e.g. in the case of PrP or it can be an unfolded non-native polypeptide product as e.g. in the case of Aβ. The process requires unfolding, which is facilitated in intrinsically disorder proteins such as αS and others, as they explore more conformations on their folding landscape and are hence more prone to aggregation. The aggregates then grow through monomer addition, once a nucleus is present. Further secondary processes can lead to the formation of additional nuclei. These processes could be secondary nucleation and fragmentation. Both processes have been included in mathematical models which could fit available data more accurately than a simple nucleation elongation process. [19–21] Fibril fragmentation, as the name suggests, is the process of fibrils breaking apart and form more fibrils which can then grow and fragment further. Secondary nucleation is the templated growth on a fibril acting as a nucleus which can provide additional surface for the aggregation. Both processes could potentially lead to an exponential increase in fibril mass which could facilitate disease spreading and progression.

For many of amyloid forming proteins the cellular function is not known. But there is also a lack of understanding of the precise molecular mechanisms underlying these diseases. I will introduce some modern techniques that have been used previously and are used in this dissertation to put the following results and techniques into context of the current state of research. Despite its important role in many neurodegenerative

disorders, including AD, I will not discuss the properties and molecular nature of the tau protein. The work in this thesis is focused on Aβ and αS and hence, the focus will be on the latter.

1.2 Biophysical Techniques to Study Protein Aggregates

I will give an overview over the use of advanced biophysical techniques to study protein aggregation with a focus on αS and Aß. Most recent *in vitro* studies have used recombinant or solid phase synthesised proteins that were incubated under conditions favouring aggregation [22,23,32,24–31]. Even though the *in vivo* fibrils are morphologically indistinguishable from the ones *in vitro* [33,34] their biological states could still differ and this has only been shown for fibrils. The aggregation reaction varies greatly between proteins and conditions. However, it is commonly separated in three phases: a lag phase in which no or very little fibril formation is observed, the elongation phase in which the fibrils grow and the final plateau phase in which the reaction reaches an equilibrium with no observable changes [35]. Of particular interest is the lag and elongation phase as in these two phases most of the crucial molecular processes take place. The formation of aggregation nuclei happens in the lag phase while in the elongation phase a multitude of mechanistically different elongation processes can happen which will be discussed in more detail later.

In protein purification insolubility would often be described as a negative trait, nonetheless in the case of amyloid proteins this might have helped to describe the amyloid fibrils first, of all the occurring protein aggregate forms [36,37]. In recent years much evidence suggests that the more soluble aggregates are more toxic [38–46]. These are highly heterogeneous, rare and transient in nature, and so are difficult to study. This is why many modern techniques have been developed and adapted to study these early soluble aggregates.

1.2.1 Bulk techniques

One of the most common techniques to observe *in vitro* fibril-formation is the use of the molecular rotor dye thioflavin-T (ThT) [47]. The fluorescence quantum yield drastically increases upon binding to beta-sheet rich protein structures which are a main feature of amyloid fibrils [48]. The increase in fluorescence which correlates with the presence of amyloid fibrils can either be measured continuously with the dye present (e.g.in a plate-reader) or at given time point with the aggregation occurring in absence of the dye (e.g. in a conventional fluorimeter). This distinction is important as it allows to control for interference of the dye with the aggregation reaction. These methods are easily implemented and used routinely to control aggregation reactions of many amyloid proteins. The fitting of mathematical models of fibril formation

reactions has led to insights into the kinetics of the process. The main rate limiting steps were determined from kinetic data through the models and determine the contribution of primary nucleation, elongation, secondary nucleation and fibril fragmentation [49-51].

The fluorescence from the aggregation is only measured for the ensemble of the system which is the main limitation of these techniques. We cannot observe individual species with these methods, but moreover we might not detect species that are important for the disease progression as they might not contain sufficient beta-sheet content to effectively bind ThT. This is where new dyes have been developed and tested to detect a wider range of aggregates [52,53].

To get insight into the actual size of the species present, other techniques such as dynamic light scattering (DLS) and analytical ultracentrifugation (AUC) can be used. DLS uses the light scattering properties of small insoluble particles to infer a size distribution and is commonly used in protein aggregation studies(Figure 2) [54]. Again, DLS is an ensemble method, which means for any given measurement it will only give an average size of the aggregates. It has a resolution limit of about 1 nm with a bias towards larger species, which scatter the light better [54].

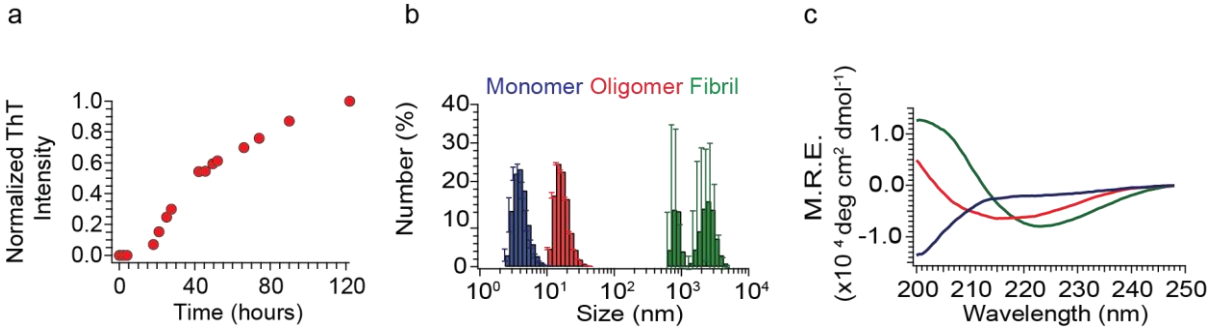

Figure 2 Commonly used bulk techniques to characterise protein aggregation. (A) ThT fluorescence trace measured in bulk with a fluorimeter or a plate reader with increased fluorescence due to the aggregation of αS (B) Size distributions of monomeric, oligomeric and fibrillar populations of αS, measured by DLS (C) CD traces of CD traces of αS monomers (blue trace), oligomers (red trace) and fibrils (green trace). The figure has been reproduced from Kundel et al. [37]

Structural information about the protein backbone can be measured with circular dichroism (CD). Amino acid secondary and tertiary structure elements rotate the polarisation of light differentially in their absence or presence. Hence, CD can give information about the average structural composition of the aggregates. This is particularly useful as aggregates undergo a structural transition from an unfolded state via possible intermediate or native conformations to amyloid fibrils which can all have different secondary structures [55].

1.2.2 Fluorescence based single-molecule techniques

The protein aggregation process is highly heterogeneous, which demands for techniques to characterise individual aggregates such as the highly heterogeneous oligomers all the way to fibrils. Single molecule fluorescence methodologies have therefore revealed much about the non-homogeneous processes in protein aggregation. In fluorescence microscopy, even with a fluorophore attached to the protein of interest, it is still important to achieve a high signal-to-noise ratio to visualise single molecules. This can either be achieved by increasing the signal, which is often limited by the available fluorophores. The second method is to reduce the background by reducing the excitation volume. The two most common techniques this is achieved are: confocal microscopy and total internal reflection fluorescence (TIRF) microscopy.

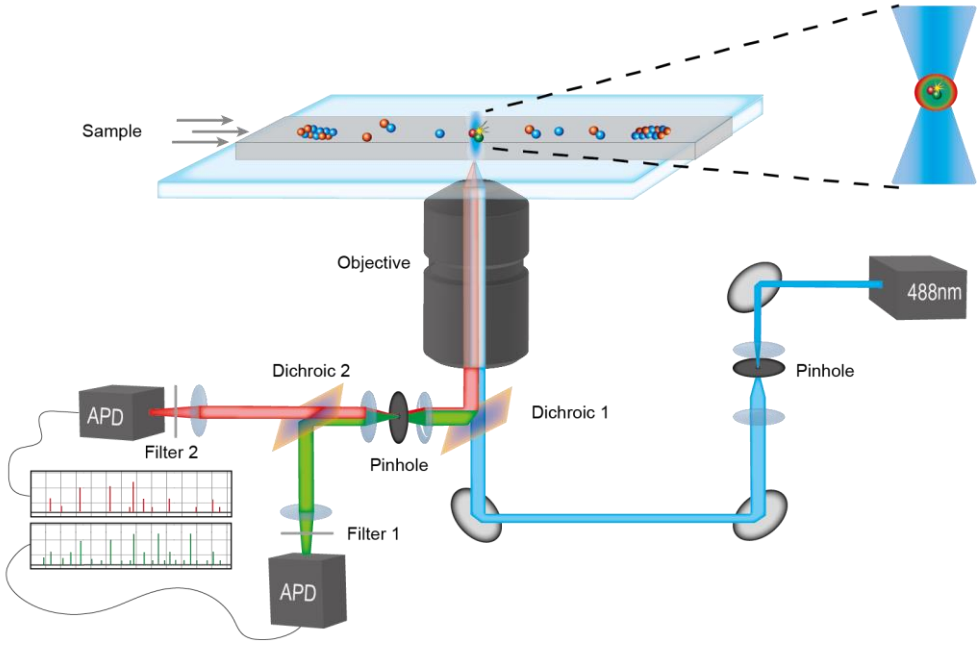

Figure 3 Schematic of the working principle of a confocal microscope for smFRET and TCCD. In a confocal microscope the excitation light is focused onto the back aperture of a high numerical aperture lens to form a diffraction limited spot to excite the fluorophores. The emission light is then filtered from the excitation light and focused onto an APD. For TCCD a second excitation wavelength is overlapped with the first one. The microfluidic channel is shown schematically. The details of the filters and dichroic mirrors are given in chapter 3.2.

Confocal microscopy uses a collimated laser beam that is focused by a high numerical aperture lens to a diffraction limited spot to excite the fluorophore. The fluorescence of the excited fluorophores is then focused and collected on a highly sensitive avalanche photo detector (APD).

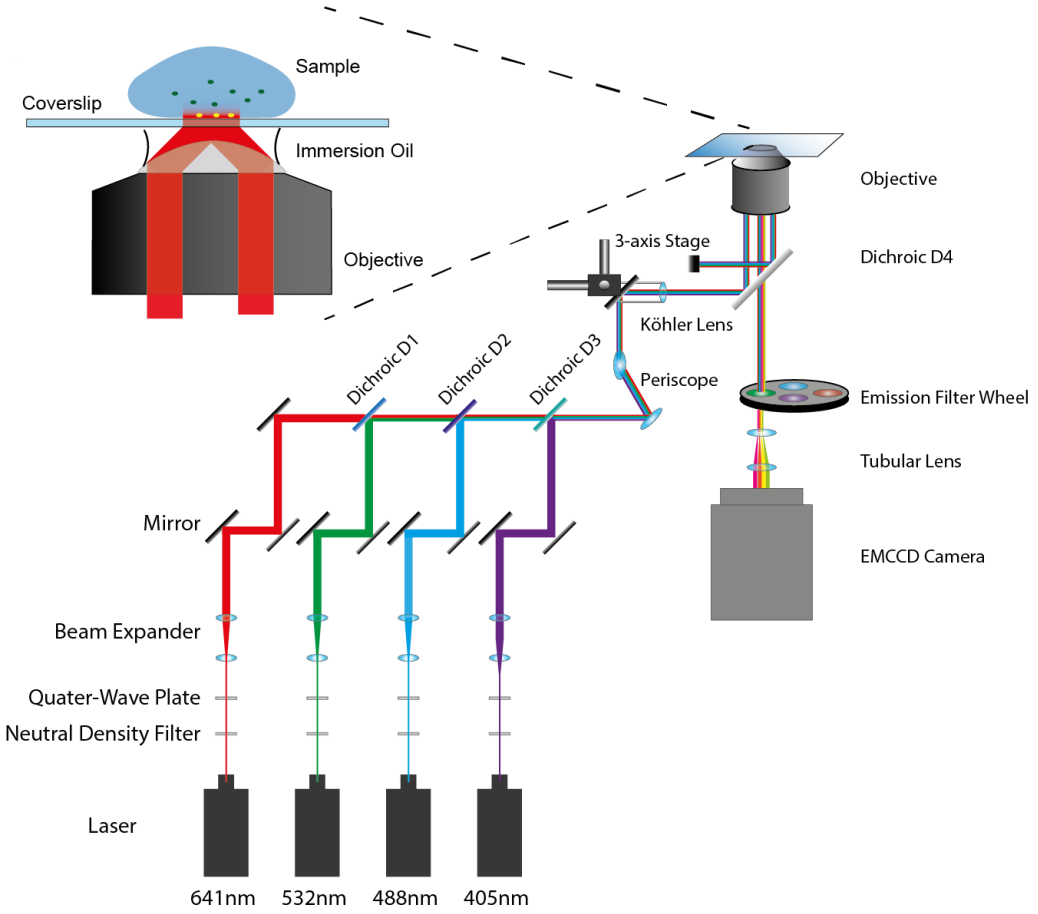

Figure 4 TIRF setup for smFRET and SAVE measurements. The TIRF microscope uses the principle of the total internal reflection by angling the incident laser beam to excite a very thin layer in the sample. The excitation light gets filtered and focused on an emCCD camera for detection. The details of all the filters and dichroic mirrors are given in chapter 3.2

In TIRF microscopy the incident laser beam is angled so the majority of the excitation light is reflected and only an evanescent wave excites only a very thin layer (~150-200 nm) in the sample just above the cover slide.

Confocal microscopy was first used to study protein aggregation with two colour coincidence detection (TCCD). In TCCD two wavelength confocal volumes overlap and their appropriate emissions are both measured with independent ADPs. Whenever a dye traverses the confocal volume they generate a burst of fluorescence. Monomeric dye labelled proteins give rise to a single burst in one channel whereas aggregated proteins will give a signal in both channels (Figure 5 C). This allowes us to distinguish monomeric protein from aggregates and the intensity of the fluorescence bursts gives some information about the size of the aggregates. The first protein studied with this technique was a equimolar mixture of differentially dye-labelled SH3 domain of phosphatidylinositiol-3'-kinase (PI3-SH3) [56].

This principle can be extended and modified multiple ways. In the scanning for intensely fluorescent targets (SIFT) [57,58], the two overlapped beams are moved through the sample to detect species. The use of a microfluidic channel improves the sampling rate over measuring only species crossing the confocal excitation volume due to diffusion (Figure 5 A) [59]. Furthermore, instead of the coincident fluorescence signal, the Förster resonance energy transfer (FRET) can be measured with the same principle. This can be achieved by using a fluorescence donor and acceptor pair and excitation in only the donor channel. This can be used to determine the relative mean distance between the fluorophores, giving some insights into the monomer density within an aggregate [40,60,61].

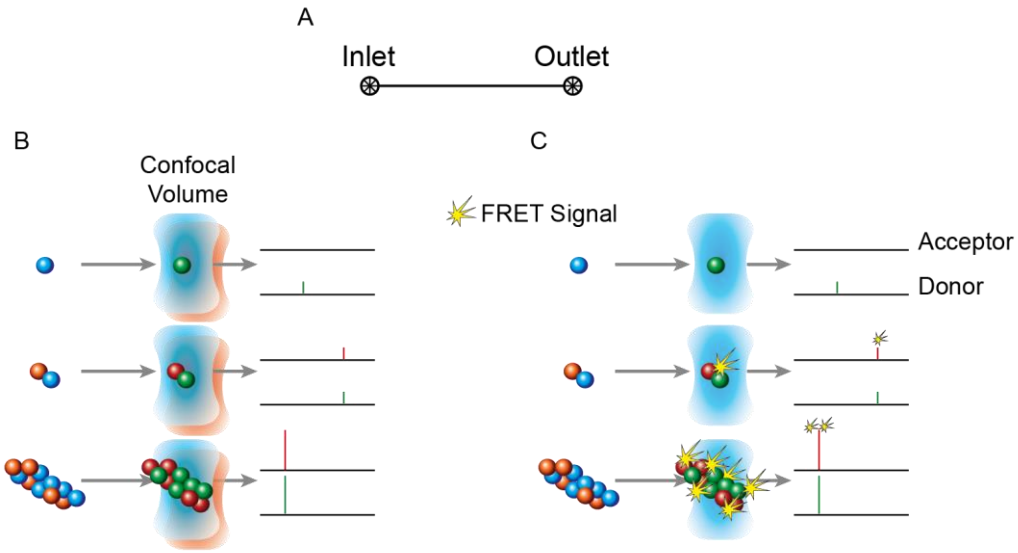

Figure 5. TCCD and smFRET for the ultrasensitive detection of protein aggregates (A) The schematic of the microfluidic channel with 100 µm in width and 25 µm in height is shown.(B) In TCCD, two colour excitation is used to excite molecules transiting the confocal volume. Only those which contain both dyes give rise to coincident bursts. (C) In FRET based measurements, only one wavelength of light is used to excite the molecules. In molecules in which the two dyes are close enough for FRET to occur (yellow star), there is a simultaneous burst in both channels.

Although surface effects are removed in these solution-based techniques the data interpretation has limitations, as the structures are inferred from a burst of fluorescence. Structures exceeding the size of the confocal and aggregates not passing through the excitation volume completely can cause further problems in data analysis. Finally, due to the sub-nanomolar concentrations required to achieve single-molecule sensitivity, some species may dissociate upon dilution. However, development of microfluidic devices that allow rapid mixing before measuring can remedy this problem to some extent [59].

A confocal microscope setup as the one described can also be used for fluorescence correlation spectroscopy (FCS) [62,63]. FCS measures the temporal fluctuations of multiple fluorophores in the confocal volume which allows to infer concentrations and diffusion coefficients of the species. As it relies on multiple fluorophores in the confocal volume it can be difficult to deconvolute mixtures without defined populations.

TIRF microscopy is usually a surface-based method. It uses the phenomenon of total internal reflection that occurs when a plane of light travelling through a transparent medium of a given refractive index is incident upon a dielectric interface with another medium of a lower refractive index at an angle greater than the critical angle. This results in an "evanescent wave" penetrating a small distance into the medium and decaying exponentially. In the case of objective based TIRF [64], collimated laser light from a high numerical aperture objective lens is reflected from the bottom of a glass coverslip containing aqueous solution, and the evanescent wave is used to excite a wide field typically <200 nm into the sample (Figure 4). In contrast to epifluorescence microscopy this partial excitation leads to a greatly increased signal to noise. The resulting fluorescence is, in both cases, collected by the same objective, filtered and focused onto an electron-multiplying charge-coupled device (emCCD) or an equivalent scientific complementary metal-oxide-semiconductor (sCMOS) camera.

As surface based widefield technique TIRF microscopy can overcome some of the limitations posed by the confocal techniques described. It can be used to directly observe fluorescently labelled amyloid aggregates on a glass slide. The physical structure and size can be visualised due to the diffraction limit with a resolution of approximately 250 nm depending on the wavelength. Under very controlled conditions the photobleaching properties of fluorescent dyes can be used to estimate the numbers of subunits which decreases stepwise. With increasing sizes these estimation get less precise as too many dye molecules are present and the individual steps are not visible anymore, which can be avoided by sub-stoichiometric labelling [65].

With the diffraction limit capping the achievable resolution in wide field microscopy to around 250 nm another problem is posed in the study of amyloid aggregates. As transitions between monomers to nuclei to soluble oligomers to protofilaments and to small fibrils can all happen below an aggregate size of 250 nm these processes might not be distinguishable.

Optical super-resolution methods [66-68] have enabled the identification of structures as small as 5 nm [69]. The most commonly used approaches to achieve these results are Photoactivated localisation microscopy (PALM) [66], stimulated emission depletion (STED) [68] and stochastic optical reconstruction microscopy (STORM) [67]. STED is implemented on a scanning confocal microscope which limits the illumination of the sample to a region smaller than the diffraction limit. STORM works by separating the signal of single fluorophores spatially and temporal (stochastic switching and readout). The individual fluorescence localisation can then be fitted to 2D Gaussian functions to determine their centre which allows for improved resolution. This switching can be achieved through various principles. In STORM the fluorescent dyes are stochastically photoswitching between dark and fluorescent states. PALM achieves the stochastic separation of the fluorophores through photoswitchable fluorescent proteins (usually switched to a longer wavelength through irradiation with ultraviolet light) to separate fluorescence from single emitters in time [66]. Methods such as point accumulation for imaging in nanoscale topography (PAINT) [70] and uniform PAINT (uPAINT) [71] use fluorescent probes that temporarily bind to surfaces or binding partners. This has been adapted in DNA-PAINT [72,73]. Transient binding is achieved by interaction of short strands of DNA designed to fit the residence times required at the desired conditions. The PAINT principle has also been used in sPAINT [74] a technique designed to super-resolve the surface hydrophobicity of e.g. amyloid fibrils with the binding of the dye nile red. Nile red does not only transiently bind to the surfaces, allowing super resolution, but simultaneously shifting wavelength depending on the hydrophobicity of the environment, allowing for hydrophobicity maps on the nanoscale.

1.2.3 Lable free techniques

I will discuss approaches that do not require the attachment of an organic fluorophores to the protein of interest, hence label free. The covalent attachment can be difficult to achieve or alter properties of the protein or label. The labelling sites could be limited by the commonly used chemical attachment on primaty amines or sulfhydryl groups on the amino acid sidechains. If neither none of these functional groups are or too many, a 1:1 molar labelling can be difficult to achieve. Mutations or alternative stop-codon usage respectively can circumvent this limitation but in both cases the protein needs to be controlled for functionality. It has been shown that the

attachment of fluorophores can affect the kinetics of protein aggregation, or structures of the fibrils [75].

Label free techniques can use mechanisms to facilitate structural insight via the use of completley non-fluorescent methods, such as AFM, NMR or EM, that use integral properties of the proteins to make them visible. Another approach is to use indirect labelling strategies such as the use of antibodies, nanobodies or aptamers that carry the fluorescent label and specifically bind to the target structures. The fluorophore can also be the probe itself as in the case of extrinsically fluorescent dyes such as ThT, pFTAA and Bis-ANS or nile red in SR applications [74,76]. One method is to use ThT coupled with TIRF microscopy to detect protein aggregates directly. This means this can and has been used to observer aggregates in biofluids such as cerebrospinal fluids. [77] I will discuss this in more detail in chapter 4.

1.2.4 Other techniques

To overcome some of the shortfalls of ensemble techniques, surface-based methods have also been used to characterise the aggregation process. Quartz crystal microbalance (QCM) sensors are able to determine mass variation per unit area by measuring the change in frequency of a resonating quartz crystal. This method is sensitive enough to report on the change in mass of surface-attached fibrils and has enabled very precise measurements of the influence of solution conditions on αS fibril elongation to be obtained [78].

The advances in super resolution light microscopy allow imaging resolutions of greater than 20 nm to be achieved. However, higher resolution structures can be necessary and useful which require more resolving power. Transmission electron microscopy (TEM) is commonly used to determine the structures of aggregates at higher resolution. A highly focused electron beam is used to image specimen to resolutions as high as 0.2 nm. The sample preparation is complex which limits its applications. Some of these sample preparation issues have been solved cryo- elctron microscopy (cryo-EM) in which the samples are not chemically fixed but rapidly cooled, so they are fixed in amorphous ice. The developers of this technique have recently been awarded the Nobel prize in Chemistry [79,80]. To resolve molecular structures, it is necessary to reconstruct many different projections of the identical protein which requires a very high sample purity, which is a challenge for highly heterogeneous mixtures. Nonetheless the structures of purified kinetically trapped

oligomers of αS [81], tau filaments extracted from a human AD brain sample [82], poly-glutamine expanded huntingtin fibrils from cultured neurons [33], and Aβ fibrils [83] were solved.

Atomic force microscopy (AFM) as a non-fluorescent surface-based technique allows the mapping of surface topography and Youngs modulus of molecules. AFM uses a tip on a cantilever to raster scan a surface [84]. The reflection of a laser beam off the tip reports the displacement of the tip, allowing vertical resolutions of the surface of less than 1 nm with lower vertical resolution. Despite the high resolution and the advantage of being label free, AFM is still a surface-based technique, with the problems that come with this. For example findings can be perturbed by differing fibril growth rates on the surface or different binding propensities to the surface [85].

Both AFM and EM have the advantage that the proteins can be detected in the absence of proteins. They are both sensitive to surface effects which may alter findings [85]; this could stem for example from changed fibril growth rates on the surface or different surface attachment propensities.

1.3 Alzheimer's disease and the visualisation of amyloid beta aggregates

The following paragraph is an excerpt from a review I co-authored and was published [37].

The presence of extracellular plaques composed of the Aβ peptide is a pathological hallmark of AD [5]. Aβ is formed and released into the extracellular space through the cleavage of the amyloid precursor protein (APP) [86]. This cleavage can be performed by several proteases such as ADAM 10, BACE 1, α- and γ-secretase, leading to the formation of various N- and C-terminal isoforms of Aβ [87,88]. When the expression and degradation of Aβ is controlled there is evidence suggesting that the peptide has several important and possibly neuroprotective functions, such as regulating synapse activity [89]. However, when the homeostatic balance of Aβ production is disturbed the aggregation of the peptide plays a key role in neurodegeneration [90-92]. As a result, much effort has been dedicated to characterising aggregated Aβ species. It is not clear precisely which factors lead to the loss of the normal balance, however the ratio of the most abundant cleavage products Aβ1-40 and Aβ1-42 has been implicated to be important to AD pathogenesis, adding greater complexity to the oligomer formation process [93].

Due to the high aggregation propensity of Aβ, it can be challenging to obtain a homogeneous monomeric sample, as the molarities required for many ensemble methods are high enough to trigger aggregation. This makes studying the kinetics of aggregation troublesome, since there may already be seeds present which can complicate the reaction. Despite this, a variety of soluble aggregates have been studied, but most have not been characterised beyond the use of SDS-PAGE and antibody reactivity [94]. Beyond this, various structural and functional details have been obtained for water-soluble, non-fibrillar Aβ assemblies [94]. Structures that have been described include protofibrils [95,96], Aβ-derived diffusible ligands [97,98], globulomers [99], spheroids [100,101], disulphide cross-linked Aβ [29], cell-derived SDS-stable low n-oligomers [102,103], Aβ*56 [104] and a brain-derived SDS-stable Aβ-dimer [29,94]. They all have in common distinctly different biological effects compared with mature fibrils, although some of them contain cross β-sheet structures, such as the protofibrils [95,96].

The most commonly used techniques to characterise Aβ aggregates are AFM and TEM. Both techniques are used to examine the morphological differences exhibited

by various aggregates, such as elongated amyloid fibrils and small, globular oligomers [105-108]. These approaches have been used to study all species throughout the aggregation process, as well as comparing the structure of aggregates produced by mutant variants [109,110]. AFM studies showed that not only the morphology of aggregates changed throughout the aggregation process, but the Young's modulus (a measure of stiffness) also increased, suggesting an internal structural rearrangement [111]. Furthermore, Aβ fibrils have been resolved at the atomic level with X-ray crystallography and solid state-NMR including variations in clinical subtypes of AD [112-114]. Structures of the cross β-sheet amyloid state are reviewed in great detail by Eisenberg and Jucker [115]. A complete *de novo* 42 amino acid atomic model of Aβ fibrils has also recently been solved via cryo-EM [116].

Fluorescently labelled Aβ peptide variants are readily available as solid-phase synthesis allows the efficient site-specific conjugation of single fluorescent tags to the Aβ peptides. This has facilitated the use of highly sensitive single-molecule methods to study the properties of individual Aβ aggregates, especially oligomers. The application of single-molecule methods to study early aggregates has provided insights into the size distributions and effects of very early aggregates [117-119]. Narayan and colleagues found that Aβ oligomers initiated neuronal damage on astrocytes [120] and were sequestered by an extracellular chaperone [118]. They described the oligomers as mostly below 10-mers in monomer units, and using TCCD it was possible to study these at levels much closer to their physiological concentrations compared to other techniques [118]. Furthermore, these fluorescent methods have been used to show how oligomers preferentially interact with cell membranes relative to monomers [121]. Subsequently, Flagmeier et al. used an ultrasensitive membrane disruption assay to show that Aβ42 oligomers but not monomers or fibrils are able to disrupt lipid vesicles at picomolar concentrations [92].

Aggregate analysis via TCCD and confocal photobleaching trajectory analysis [117] are limited by acquisition times and instrumental dead times. Whilst the timescale of *in vitro* aggregation of the majority of amyloidogenic proteins is sufficiently slow to take full advantage of these techniques, the temporal resolution can be a limiting factor for the ability to detect early aggregation events of proteins with fast aggregation kinetics, such as Aβ42. To overcome this limitation, microfluidic strategies have been used, whereby the aggregation mixture is rapidly flowed through the confocal volume to

increase the rate of detection, and therefore increase the time-resolution of the methods [60].

TCCD measurements of co-oligomer formation between Aβ40 and Aβ42 helped generate a thermodynamic model of the peptides' aggregation propensities [122]. It should be noted that the ability to size aggregates from TCCD and smFRET measurements is limited due to several factors such as the inhomogeneity of the confocal volume and fluorescence quenching at high label densities. Improvements to the former have been suggested by Murphy *et al.* through the use of Bayesian Inference [123], which led to the data analysis on population sizes and intramolecular distance being more robust than simple threshold-based analysis, especially in more complex datasets.

Super-resolution techniques have been used to probe the seeding capacity of Aβ aggregates in addition to the morphology of aggregates in CSF [124,125]. By seeding fluorescently labelled Aβ40 with brain- and CSF-derived Aβ from AD and control patients it has been shown, using dSTORM, that seeding capacities and elongation rates were dependent on aggregate size [126].

In order to perform label free imaging *in vivo*, there has been a surge in the development of fluorescence imaging probes with similar properties as ThT and Thioflavin S (ThS). Notably the class of oligothiophenes has been used to image Aβ aggregates in their pre-fibrillar and fibrillar state both *in vitro* and *in vivo* (Figure 6) [127-129]. Interestingly, these dyes show different spectral footprints for the different amyloid topologies of Aβ and tau [130]. Similarly, the hydrophobicity reporter dye nile red has been used to spectrally super-resolve local hydrophobicity propensities of amyloid aggregates using sPAINT [74].

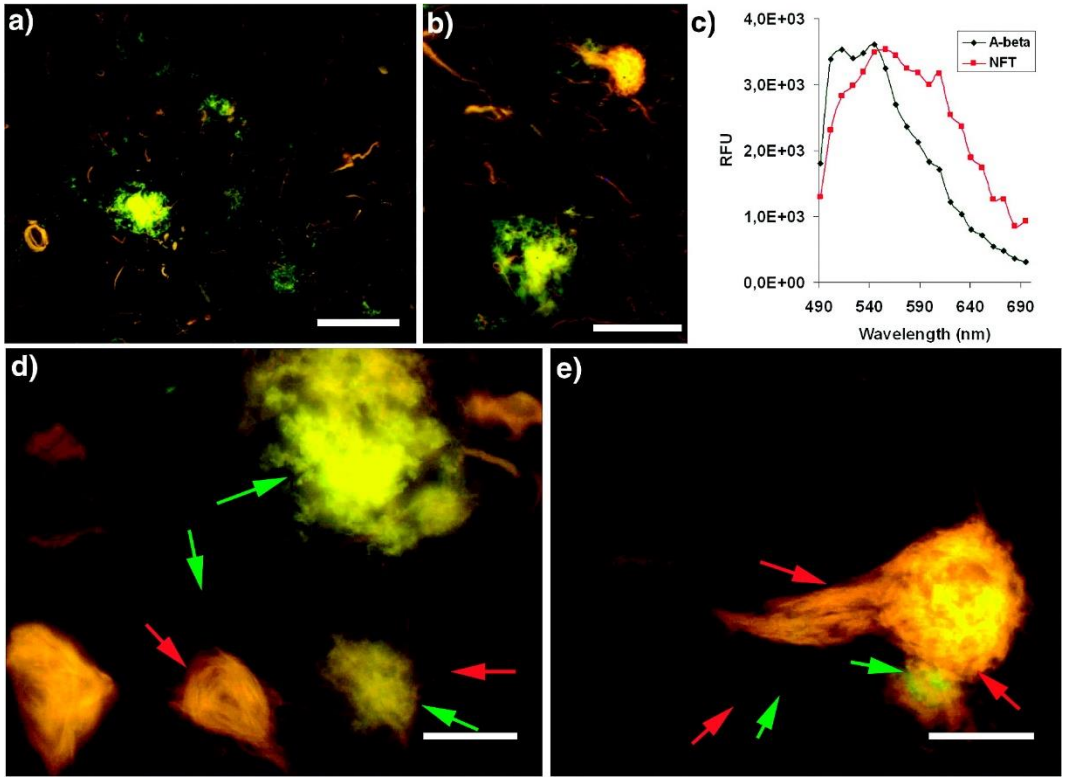

Figure 6 High resolution fluorescence images and emission spectra of pFTAA bound to pathogenic hallmarks in AD. (A,B) Fluorescence images showing an overview of the interaction between Aβ deposits (green), NFTs, and dystrophic neurites (yellow and red). (C) Emission spectra of pFTAA bound to Aβ aggregates (green spectrum) or NFTs (red spectrum). (D,E) High resolution fluorescence images showing the details of the distribution between Aβ deposits (green), NFTs, and dystrophic neurites (yellow and red). Selected Aβ deposits and NFTs are highlighted (green and red arrows, respectively) to indicate striking spatial co-localisation. Scale bar = 50 µm (A), 20 µm (B) and 10 µm (D and E). Figure adapted from Aslund et al. [128] and reproduced from Kundel at al [37] .

A different approach in understanding the molecular mechanisms of aggregation, and hence oligomer formation, is through the combination of high quality kinetic data and kinetic modelling. This work on Aβ has been pioneered by the Knowles and Linse groups. High purity recombinant monomeric Aβ42 has led to robust aggregation kinetics which has enabled the use of global fitting models to get insight into molecular mechanisms of the underlying processes [131-133].

An online modelling platform has been made available to investigate the effect of interactions of Aβ with, for example chaperones [134] or antibodies [135] and to model molecular mechanisms for other amyloid proteins [132]. This has shown that Aβ42 aggregation is strongly dominated by secondary nucleation, and hence the presence of seeds has an autocatalytic effect on the aggregation process [19]. However, care needs to be taken when inferring *in vivo* mechanisms from *in vitro* models, as some of the

effects may be compounded by cellular components, for example fibril seeding on the membrane.

The application of the above mentioned advanced biophysical methods has led to insights into the molecular mechanisms underlying Aβ aggregation and has given us insights into some structural features of the resulting soluble aggregates and amyloid fibrils. One of the main challenges is to link these molecular mechanisms and structural features to the resulting neurological effects and finally to the clinical manifestation of the disease. The prolonged time-course of the disease and the low Aβ concentration in the extracellular space are of particular interest. *In vitro,* Aβ aggregation time-courses are usually studied over hours at concentrations that are orders of magnitudes higher of what is found in the CSF [136]. Furthermore, the interactions and interplay between different Aβ peptide isoforms and with other amyloid forming proteins have not been conclusively explored. The application of the techniques described, could allow the investigation of the aggregates at the atomic and molecular level and help understand the neurobiology of these diseases.

1.4 α-Synuclein oligomers in Parkinsons disease

αS was one of the first described intrinsically disordered proteins [137]. It was identified as the major component of Lewy bodies found in PD and other synucleinopathies and has been associated with amyloid plaques in AD [137,138]. A further link between the disease and αS comes from the autosomal dominant forms of the disease which show duplications and triplications of the *SNCA* gene encoding for αS [139,140]. A third confirmation comes from the single residue missense mutations in αS in the early onset forms of PD [141-146].

Structurally αS consists of three main regions: the positively charged N-terminal region (residues 1-60), the central hydrophobic domain (61-95) also called non-amyloid β-component (NAC) and the acidic C-terminal end (96-140). The N-terminus contains a apolipoprotein-like helical sequence that drives the alpha-helix acquisition upon binding to membranes [147,148]. The NAC region is responsible for the aggregation of αS and the formation of the beta-sheet during fibril formation [149,150]. The proline rich, negatively charged and acidic C-terminus facilitates protein solubility and has no known secondary structure elements [151]. αS is highly dynamic as it is able to transition between different secondary structures depending on its interaction partners [152].

The localisation of mutations in non-sporadic PD cases are all found in the N-terminal region of the protein just flanking the NAC region [153]. It indicates that the mutations modulate the conformational landscape of αS which has been shown both *in vitro* and *in vivo* [31,154-158]. Especially the A30P mutation proved useful as αS, with this mutation, forms a population of trapped oligomers that led to the hypothesis that oligomers are responsible for toxicity in PD [31].

Testing this hypothesis, the generation of a large number of oligomers was required. Methods to achieve this included incubating concentrated αS solutions on ice [159], incubating at 37°C [81,160] and the combination of the incubation with size exclusion [161,162] or diafiltration steps [163] respectively. Even though a recent study managed to purify and characterise kinetically-trapped oligomeric species and characterise them using fluorescence, CD, AFM, DLS and cryo-EM, they did not go on to form fibrils [81]. With the oligomers trapped in an energy well for alternative aggregation/ folding of αS they might not represent the complete picture of heterogeneity of αS oligomers [81,161,164-166]. Depending on the conditions used purified

oligomers differ however and can go on to form fibrils [167-169]. Many additives and conditions have been used to generate various forms of oligomers and have been extensively reviewed recently [170]. While amyloid fibrils *in vivo* are similar to the end point in *in vitro* [33,34], there is no structural information on the oligomers present in the brain as of now. It is conceivable with the same final structure that the formation happens via a common intermediate, but this needs to be confirmed.

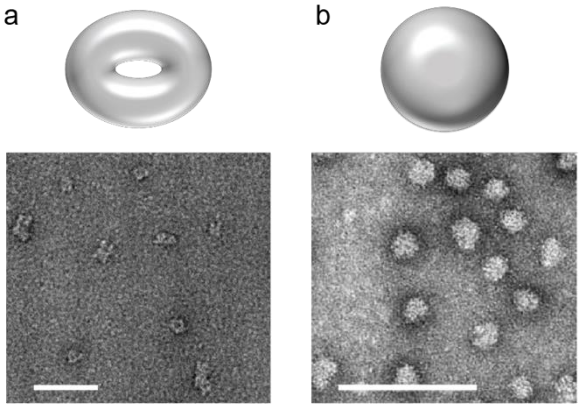

Figure 7 TEM images of oligomers. (A) Annular oligomers described for the first time by Lashuel et al. [159] formed by dissolving lyophilised αS in PBS at a concentration ranging from 300-700 μM and incubating on ice for 30-60 min. Oligomers were then filtered through 0.22 μm filters and separated from monomers by gel filtration. Scale bar is 50 nm. (B) Spherical oligomers as observed by Ehrnhoefer et al. [166]. 100 μM αS was incubated in the presence of N-epigallocatechin gallate (1:10) and incubated in TBS buffer on a rotary shaker (conditions favouring aggregation) at 37°C. Oligomers were separated from monomers and other aggregates by gel filtration. Scale bar is 100 nm. The figure is adopted Kundel et al. [37]

Crosslinking has been used to capture the rare and transient αS oligomers *in vitro* [171,172]. Their size has been characterised but as they are crosslinked and therefore trapped it is not clear if they go on to form fibrils and hence how well they represent the oligomers in the brain. The use of native mass spectrometry has allowed to investigate the size of oligomers and showed different conformational states of monomers and dimers [173,174]. Drift-time analysis showed the presence in sizes from dimers to hexamers, giving insight into their topology [175]. However, these methods require the aggregates to be dissolved in specific buffers which could perturb their structures and are limited in characterising larger oligomers [174-176].

The use of fluorescence methods has been extensively used to monitor intermolecular interactins in αS. Structure-based non-covalent fluorescent probes have been developed and used to specifically detect oligomers, pre-fibrillar species and fibrils [177,178] and will be discussed in more detail in chapter 4. Similarly, nile red is a non-covalent structure-based fluorescent probe. This was used in sPAINT to look at the nanoscopic hydrophobicity landscape of both oligomers and fibrils [74]. We showed

that the oligomers have a higher surface hydrophobicity than the fibrils, which could be a mechanism of toxicity.

Fluorophores can also be conjugated directly to the protein using maleimide chemistry on cysteine residues inserted by site-specific mutagenesis [179-181]. Great care has to be taken to not interfere with the aggregate formation or oligomer structure of the protein through the incorporation of the fluorophores. The covalent attachment of the fluorescent probes to the monomers opens up a variety of methods to study the aggregate formation. FCS, as described above, allows to estimate the size distribution and the concentration of oligomers from their diffusion coefficients giving some insight into early aggregate formation [180].

Single-molecule techniques are of particular power for heterogeneous mixtures as observed with rare αS oligomers. The first technique applied to study αS was SIFT [58,182-184]. SIFT assigns the bursts of higher fluorescence to oligomers, while being able to measure them individually. This is refined in the analysis of photobleaching steps in sub-stochiometric labelled αS. This was done on a TIRF setup as to allow for continuous imaging [65]. Accurate identification of individual photobleaching steps in a single aggregate is usually limited to about ten fluorophores. The study identified a purified oligomer of 31 monomer however. This result has to be seen within the limitations of the technique. The method is biased for the detection of brighter species and the analysis assumed one size of oligomer, which may not have been the case.

In depth single-molecule studies using TCCD and smFRET were made possible through the introduction of a cysteine at position 90, just flanking the fibril-forming region [40,60,61]. The single-molecule measurements revealed two oligomeric populations, masked in ensemble methods. The two populations exhibited different 'compactness' as measured by FRET, different resistance to proteinase-K degradation and different stability in low ionic strength buffers [60]. The same techniques were then used to study the subtle structural differences between the oligomers generated by various mutant forms of αS and the wild type form [61,185]. Furthermore, studying the aggregation kinetics on single-molecule levels at different concentrations allowed to infere a kinetic model of the conversion rates of the two different types of oligomers [186].

Observing oligomers in human biofluids is helping understand structural properties, but it still remains a major challenge to observe native oligomers in cells or

even *in vivo*. Most efforts so far used antibodies *in vivo* as their application is well established and compatible with many imaging techniques [187,188]. Further techniques like complementation assays or proximity ligations assays [189-193] or confocal microscopy methods [194,195] have been used to study αS self-interaction.

2 Aims of this thesis

This dissertation has two main parts. The first part will focus on the possible applications of extrinsically fluorescent dyes to study protein aggregates *in situ*. This will focus on the application of new dyes in the use of the SAVE method focusing on aS and PD. We will answer some technical question to explore the possibility of the described methods as a possible biomarker.

I will then present results how a combination of techniques has allowed us to transfer the said method to AD patient samples and get insight about the structure of the neurotoxic aggregate in human CSF. Furthermore, I will show what implications these findings have on the development of antibodies and why some of them could have failed in clinical trials.

Secondly, I will present a novel, modified approach on how to isolate various oligomeric species of Aβ42 and their distinct structural properties in a cross-sectional manner. More importantly this new approach helped us to understand in more detail some biological implications of the species occurring throughout the aggregation reaction.

3 Material and Methods

3.1 Biochemical Methods

Preparation of αS Aggregates

αS aliquots were kindly provided by Beata Blaszczyk and Ewa Klimont. Either the wild-type or A90C variant (for labelled αS) of monomeric αS was purified from *Escherichia coli* as described previously [196,197]. For A90C, the single cysteine was labelled with maleimide-modified Alexa Fluor 647 (AF647) as previously reported [198]. The excess dye was removed by passing the labelled protein through a P10 desalting column containing Sephadex G25 matrix (GE Healthcare). The protein was concentrated using Amicon Ultra Centricons (Millipore), divided into aliquots, before being flash-frozen in liquid nitrogen and stored at -80°C. Each aliquot was only thawed once prior to use. For the aggregation reactions, a 70 μM solution of wild-type αS in 25 mM Tris buffer (pH 7.4) and 0.1M NaCl (with 0.01% NaN_3 to prevent bacterial growth during the experiments) was incubated in the dark at 37°C, with constant agitation at 200 rpm for 22h prior to the experiment.

Preparation and purification of recombinant Aβ42 for Single Vesicle experiments

The recombinant protein was kindly provided by Dr. Patrick Flagmeier. The recombinant Aβ42 (M1-42) peptide (MDAEFRHDSGYEVHHQKLVFF AEDVGSNKGAIIGLMVGGVVIA), here called Aβ42, was expressed in the *Escherichia coli* BL21 Gold (DE3) strain and purified as described previously with slight modifications [131,199]. Solutions of monomeric recombinant Aβ42 were prepared by dissolving the lyophilised Aβ42 peptide in 6 M Gu HCl then purified by using a Superdex 75 10/300 GL column (GE Healthcare Bio-Sciences AB SE-751 84 Uppsala, Sweden). The center of the elution peak was collected, and the peptide concentration was determined from the absorbance of the integrated peak area using $\varepsilon_{280} = 1490$ L $mol^{-1}cm^{-1}$.

Measurement of aggregation kinetics of Aβ42

For kinetic experiments the Aβ42 monomer was diluted with buffer to the desired concentration and supplemented with 20 μM ThT. All samples were prepared in low-binding Eppendorf tubes (Eppendorf AG, Hamburg, Germany) on ice. Each sample was then pipetted into multiple wells of a 96-well half-area, low-binding polyethylene

glycol coating plate (Corning 3881, Kennebuck ME, USA) with a clear bottom, at 80 µL per well. The 96-well plate was placed in a plate reader (Fluostar Omega, Fluostar Optima, or Fluostar Galaxy; BMG Labtech, Ortenberg, Germany) and incubated at 37°C under quiescent conditions using the bottom reading mode (440-nm excitation filter, 480-nm emission filter). For each new preparation of protein, the aggregation kinetics were checked by performing reactions at different concentrations of Aβ42.

Conditions for Aβ42 aggregation

Aliquots of monomeric Aβ42 were diluted with buffer to a concentration of 2 µM in low-binding Eppendorf tubes on ice. Individual samples were then pipetted into multiple wells of a 96-well half-area plate (Corning 3881, Kennebuck ME, USA) and the plate was placed into an incubator at 37 °C, under quiescent conditions. Aliquots for measurements of Ca^{2+} influx were then taken at the desired times after the plate was placed in the incubator.

HiLyte™ 647 Fluor and HiLyte™ 488 Aβ42 peptide purification and aggregation

Aβ labelled N-terminally with HiLyte™ Fluor 647 and HiLyte™ Fluor 488 were purchased from AnaSpec (#AS-64161 and #AS-60479-01). Solutions of monomeric protein were prepared by dissolving the protein in 10mM NaOH at high concentration and then purified using a Bio-Sep 2000 HPLC column (Phenomenex) in SSPE buffer (Thermo Fischer, #15591043). Peak fractions were collected, and the peptide concentration was determined using the absorbance of the fluorescent label with an extinction coefficient of 250,000 $M^{-1}cm^{-1}$ for HiLyte™ Fluor 647 and 70,000 $M^{-1}cm^{-1}$ for HiLyte™ Fluor 488. Monomeric fractions were frozen immediately after preparation and kept at -80°C until use.

Aliquots of monomeric Aβ were diluted to an equimolar concentration of 2 µM of HiLyte™ Fluor 647 Aβ42 and HiLyte™ Fluor 488 Aβ42 in low-binding Eppendorf tubes and incubated at 37°C, under quiescent conditions.

Sucrose Ultracentrifugation

The aggregated peptide was loaded on a step gradient of 10-50 % sucrose in SSPE buffer at pH 7.4 in increments of 10 % sucrose with a total volume of 2 ml. All samples were centrifuged for 15 h, 41 000 g and 20°C and the fractions were collected immediately and stored on ice until use and stored no longer than one day. The

collection was done by piercing the centrifugation tubes orthogonally in 400 µl fractions and the remaining pellet was resuspended in 100 µl buffer.

Dot Blot

Synthetic Aβ42 was aggregated for 3 h at 37°C under non-shaking conditions at 2 µM monomer concentration. 2 µl of sample at different protein dilutions were spotted onto nitrocellulose membrane slowly. After drying the membrane it was blocked by soaking in 5% BSA in TBS-T (20 mM Tris-HCL pH 7.5, 150 mM NaCl, 0.05% Tween 20) for 0.5-1 h at room temperature. It was then incubated with the primary antibody at 1 µg/ml for 30 min at room temperature. After washing 3 x 5 min with TBS-T the blot was incubated with the secondary antibody conjugated to Alexa-647 for 30 min at room temperature in the dark. Subsequently the blot was washed three times with TBS-T (15 min x 1, 5 min x 2), then once with TBS (5 min) in the dark. The blot was then imaged in a Typhoon gel imager at the according wavelengths.

Dye Solutions

ThT (Sigma-Aldrich), DiThT-PEG2 (Custom Synthesis, Peakdale Molecular) and DCVJ (Anaspec) stock solution was prepared in Dimethylsulfoxide (DMSO) (Sigma-Aldrich) diluted into pre-filtered (0.02 µm filter, Whatman, GE Healthcare) phosphate buffered saline (PBS) (Sigma-Aldrich) to a final concentration of ~100 µM. Its exact concentration was determined spectroscopically using the following extinction coefficients: ThT 36,000 M^{-1} cm^{-1} at 412 nm; DiThT 45,800 M^{-1} cm^{-1} at 410 nm; DCVJ 42,000 M^{-1} cm^{-1} at 460 nm (measured). For BTA-1 (Anaspec) and NR (Anaspec) the stock solutions were prepared weighing out the solid into DMSO. Solutions were all filtered (0.02 µm filter, Whatman, GE Healthcare) prior to use and not used longer than one day. Borosilicate glass coverslips (VWR International) were cleaned in an Argon plasma for 1 hour and prepared for coating with a 20mm x 20 mm Frame-Seal slide chamber (Bio-Rad). The coverslips were coated with 0.01% Poly-(L)-Lysine Solution (PLK) (Sigma-Aldrich) for at least 30 minutes. The PLK solution was aliquoted and stored at 80°C as storage at 4°C lead to an increase in false positives in the negative controls. The PLK-coated surfaces were washed three times with PBS before the sample was applied. Each sample was left on the coverslip for 10 min prior to imaging to ensure absorption of the species on the surface.

3.2 Fluoresence Imaging and Instrumentation

Total Internal Reflection Imaging

The samples were imaged using a home-built total internal reflection fluorescence (TIRF) microscope limiting the detectable fluorescence signal to within 200 nm from the coverslip. For imaging of ThT, DiThT, BTA-1 and DCVJ a 405 nm Laser (LBX-LD, Oxxius Laser Boxx, Laser 2000) was passed through a FF01-417/60-25 (Semrock) excitation filter to remove any stray light, passed through a quarter wave plate to circularly polarise the beam and expanded using a collimated Galilean beam expander. All other lasers and according filters and dichroic mirrors are described in Table 1. The aligned beam was directed parallel to the optical axis at the edge of a TIRF objective (APO N 60X TIRF, Olympus) mounted on an inverted Olympus IX-73 microscope (Olympus). Fluorescence was collected by the same objective, separated from the returning TIR beam by a dichroic Di01-405/488/532/635 dichroic mirror (Semrock), and passed through an appropriate filter for ThT, DiThT-PEG2 and DCVJ: BLP01-488R-25, (Laser 2000) and for BTA-1: FF01-434/17-25 (Semrock). The images were recorded on an EMCCD camera (Evolve 512 Delta, Photometrics) operating in frame transfer mode (EMGain of 4.4 e-/ADU and 250 ADU/photon). Each pixel was 207 nm in length. The distance between the 9 images measured in each grid was set to 350 µm, and was automated (bean-shell script, Mircomanager) to prevent user bias. Images were recorded continuously for 100 frames with 50 ms exposure.

Table 1 Overview over all used filters and dichroic mirrors. If not stated otherwise all filters and dichroic mirrors have been purchased from SEMROCK. *) Has been purchased from THORLABS.

Laser-Line	405 nm	488 nm	532 nm	647 nm
Excitation Filter	FF01-417 60-25	LM01-466-25	FF01-532/3-25	FF01-640/14-25
Dichroic Mirror	Di02-R442 25x36 (Dichroic D3)	DMLP505R *) (Dichroic D2)	Di02 R532 25x36 (Dichroic D1)	N/A
Emission Filter	BLP01-488R-25	FF01-587 BP		LP02-647RU-25
Filter Dichroic	(Dichroic D4)		Di01-R405/488/532/635-25x36 (Dichroic D5)	

Confocal smFRET measurement

The instrumentation and measurement techniques used in this study have been described in great detail previously [56,200]. A schematic of the confocal setup used is

shown in Figure 3. For all measurements using pFTAA the dye was used at 30 nM final concentration and only the events in the blue channel were observed.

DNA-PAINT Imaging

Glass coverslips (0.13 mm thickness, round, 50 mm diameter) were cleaned using an argon plasma (PDC-002, Harrick Plasma) for 1 h. Then, a multiwell chamber coverslip (CultureWell CWCS-50R-1.0, 50 channels) was cut in half and affixed to the glass coverslip. The slide was incubated with aspartic acid (Sigma, 1 mg/mL) for 1 h and washed once with Tris buffer (0.02 μm filtered, Anotop25, Whatman); 5.0 mM tris(hydroxymethyl)aminomethane (Tris), 1 mM EDTA, 10 mM $MgCl_2$, pH 8). Samples were incubated on the slide for 5 min, before the liquid was removed and replaced with Tris buffer containing aptamer, imaging strand and/or ThT/pFTAA. The slides were then transferred to the microscope stage and coupled to the objective using refractive index-matched immersion oil (refractive index n = 1.518, Olympus, UK). If imaging for longer than 2 h, another clean coverslip was then layered on top of the multiwell chamber to prevent evaporation.

Preparation of aptamer and fluorophores

The aptamers and fluorophores were kindly provided by Dr. Horrocks. All DNA strands were diluted in Tris buffer. The docking and imaging strand sequences were the same as those used previously [201]. The docking strand-conjugated aptamer (ATDBio, GCCTGTGGTGTTGGGGCGGGTGCGTTATACATCTA) was used at a final concentration of 100 nM. The DNA imaging strand (ATDBio, CCAGATGTAT-Cy3b) was also dissolved in Tris buffer and used at a final concentration of 1 nM. The ThT solution was prepared as described and further diluted to 5 μM in Tris buffer and mixed with the abovementioned two DNA solutions for imaging.

Super resolution imaging of cells

To prepare cells for imaging they were first washed with phosphate buffered saline (PBS) before being fixed with paraformaldehyde (4% w/v) for 15 min at room temperature. The cells were rinsed three times with PBS before being incubated for 1 h at room temperature in PBS containing 0.5% triton X-100 with 10% goat serum. The aptamer and imaging strand was then diluted to 100 nM and 5 nM respectively in

PBS + 10% goat serum. The cells were incubated with the aptamer solution overnight at 4ºC before imaging. Near-TIRF illumination was used to illuminate the cells.

Instrumentation

A home-built total internal reflection fluorescence (TIRF) microscope was used for imaging. The principal layout is equivalent to what is shown in , hence it is not sketched again. The output from two lasers operating at 405 nm (Oxxius Laser-Boxx, Oxxius) and 561 nm (Cobalt Jive, Cobalt) were aligned to the optical axis of a 1.49 N.A., 60x TIRF objective (UPLSAPO, 60XO TIRF, Olympus) mounted on an inverted Ti-E Eclipse microscope (Nikon, Japan). The microscope was fitted with a perfect focus system (PFS) which auto-corrects the z-stage drift during a prolonged period of imaging. The laser power was attenuated by neutral density filters before the beam was passed through a quarter-wave plate (to circularly polarise the laser beam), a beam expander and their respective excitation filters (FF01-417/60-25 for 405 nm and FF01-561/14-25 for 561 nm, Semrock). The lasers were combined by a dichroic mirror (FF458-Di02-25x36, Semrock) and passed through the back port of the microscope and focussed in the sample by the objective. The laser power at the objective was 1.13 mW and 10.07 mW for the 405 nm and 561 nm lasers respectively. Fluorescence was collected by the objective and separated from the excitation light by a dichroic mirror (Di01-R405/488/561/635, Semrock), and passed through appropriate filters (BLP01-488R-25 for ThT and LP02-568RS-25 for Cy3B, Semrock). The fluorescence was then passed through a 2.5x beam expander and recorded on an EMCCD camera (Evolve 512, Photometrics) operating in frame transfer mode (EMGain of 11.5 e^{-1}/ADU and 250 ADU/photon). Each pixel corresponded to a length of 131.5 nm. Images were taken in a grid by an automated script (Micro-Manager) to prevent user bias. Exposure times were kept constant at 50 ms; at least 4000 frames were acquired for super-resolution images, 100 frames were acquired for diffraction limited images. (The principal layout is equivalent to , hence it is not shown again).

3.3 Data Analysis

3.3.1 TIRF and Super Resolution Image analysis

Data analysis was performed using a custom written ThT analysis plugin for the GDCS SMLM plugin (Alex Herbert, SUSSEX UNIVERSITY) in ImageJ

(http://imagej.nih./goc/ij) kindly developed and provided by Mathieu Palayret. The individual image stacks are intensity averaged over 100 frames and the background level is determined by a quick residuals least trimmed square estimator. The signal gets fitted to a Gaussian 2D point spread function by the GDCM SMLM Peak Fit plugin. The signal-to-background threshold for all signals was kept consistent throughout the dataset after initial judgment. Furthermore, the intensity histograms and signal to background histograms were used to check for consistency. False positive correction of detected spots was done manually after each experiment with only the dye or only the PLK coated surface respectively. Photon emission was calculated with (Equation 1). All graphs have been plotted and fitted with Origin Pro 9 except the lognormal fit of the histograms was performed with custom written code in Matlab.

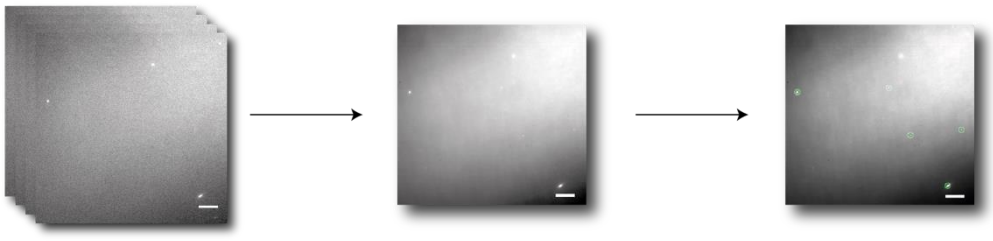

Figure 8 Workflow of the data analysis for the TIRF imaging. The RAW image stack of 50-100 individual exposures is intensity averaged for better signal to noise. The resulting image is the used to identify maxima which are the aggregates we subsequently count and compare with respect to their intensities. The resulting control image is used to check thresholds for each batch of experiments to account for variability in the experiment.

In Figure 8 it is schematically shown how the data is processed. The recorded stacks of multiple exposures of the same field of view are intensity averaged. The resulting image is cropped and then analysed further. The *find maxima* function of ImageJ is used to identify all ThT-positive spots with a noise level set for the entire experiment but varied between conditions to account e.g. for dye background. The signal to noise correction is done locally in the adjacent pixels of the peak which accounts for uneven field illumination. All identified aggregates are then overlaid with a circle to visually control for accurate fitting. The peak intensities are used to generate the histograms and the number of peaks is used to compare the sensitivity of the dyes or the number of aggregates respectively.

$$\gamma_{Signal}\tau = (DU - \gamma_{D^\tau}) \times \left(\frac{1}{QE}\right)\left(\frac{G}{M}\right)$$

Equation 1 Calculation to determine the emitted photons for image analysis

Table 2 Values for calculation of Photons for SAVE experiments. G is the analogue gain (electrons per analogue-to-digital-unit (ADU), τ is the exposure time, QE is the quantum efficiency, M is the EMCCD multiplication and γ_D is the dark count rate per pixel (Hz/pixel)

Pixel Size (nm)	207 *)
G (e^-/ADU)	4.4
τ (s^{-1})	0.5
QE	0.96
M	150
γ_D (Hz/Pixel)	500

*) the pixel size changed to 237 nm after change of the microscope body for later experiments.

For the two-colour coincidence analysis fitting of the signal was done as described above. The procedure runs for both channels and if spots in the two different channels are within 400 nm of each other they are colocalised. Chance coincidence which means having two of the fluorescently labelled species randomly occupying the same region is calculated by rotating one averaged channel 90° and translating it a third of the image size in order that any spots in the centre of the image are not accidentally found to be coincident. Chance coincidence is particular problematic for high densities and concentrations were adjusted accordingly to keep this effect minimal.

Coincidence is calculated with Equation 2 by selecting one channel as base channel and calculate how many of the spots in the base channel are colocalised to the other channel as a fraction of all spots. This is corrected by the chance spots which are the colocalised spots when one of the channels is rotated by 90 degrees.

$$Coincidence = \frac{colocalised\ spots - chance\ spots}{total\ spots - chance\ spots}$$

Equation 2 Calculation to determine the coincidence for the colocalisation analysis

3.3.2 smFRET data analysis

The smFRET data is analysed using a custom written application developed by Mathew H. Horrocks [202].

For the data analysis all intensity data of the APDs was transferred into IgorPro. The thresholds for both channels were adjusted for each set of experiments based on the background signal of the monomer solutions and the buffer solutions. To show the threshold was in the linear range for the monomer concentrations expected I

plotted the monomer brightness and the number of detected events as a function of threshold and monomer concentration (Figure 9).

To control for consistent recording the number of detected events were plotted against time throughout the experiment to control for any possible channel blockages, varying flow rates. The monomer brightness was compared throughout and the alignment was checked frequently through the use of dual-labelled DNA samples.

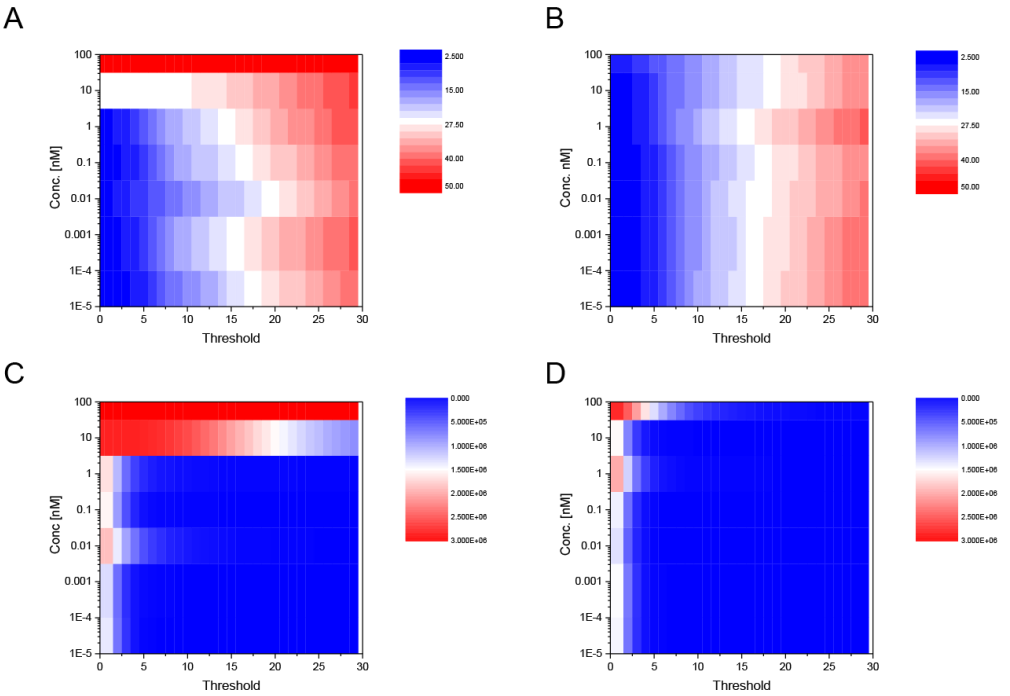

Figure 9 Threshold testing as a function of monomer concentration to determine the correct working dilutions. (A) Detected bursts in the donor channel above threshold of monomeric 488 dye as function of threshold and concentration (B) equivalent experiment with monomeric 647 dye. (C) Detected FRET bursts in the acceptor channel for (C) 488 dye and (D) 647 dye. The plots confirm that the selected thresholds are in the linear regime and the concentrations are suitable to distinguish the aggregates form monomeric bursts.

For the in depth analysis the FRET efficiency was plotted against the apparent oligomer size and depending on the requirements various other parameters were extracted such as e.g. FRET- and Intensity- Histograms of aggregates, fraction of aggregates and aggregate counts. The details of these steps have been described [40,200,203].

3.4 Other techniques

3.4.1 Vesicle Assay

The Vesicle Assay was performed by Dr. Suman De with the help of Dr. Patrick Flagmeier as described in [92].

Vesicles are prepared by mixing 1-palmitoyl-2-oleoyl-sn-glycero-3-phosphocholine 16:0-18:1 PC (Avanti Polar Lipids) and 1-oleoyl-2-[12-biotinyl(aminododecanoyl)]-sn-glycero-3-phosphocholine 18:1-12:0 Biotin PC (Avanti Polar Lipids) at 100:1 ratio. The solvent was then removed under vacuum in a desiccator overnight and the lipids were then rehydrated in HEPES buffer (pH 6.5) with 100 μM Cal-520 (Stratech). Five freeze-and-thaw cycles were performed using dry ice and a water bath, followed by 10 times extrusion (Avanti Polar Lipids) with a membrane of 200 nm cut off to improve the homogeneity of the vesicle size and lamellarity distribution. To separate non-incorporated dye molecules from the vesicles, size-exclusion chromatography was performed. Then the purified vesicles tethered to PLL-PEG coated borosilicate glass coverslides using a biotin-neutravidin-biotin linkage and incubated in Ca^{2+} containing (1.26 Mm) Leibovitz's L-15 solution (Thermo-fischer). The frame-seal incubation chambers affixed (Biorad) coverslides were placed on the instrument described below. Thereafter the sample, diluted to a concentration of twice the targeted value, was added to the coverslide and incubated for ~10 min and same field of views are imaged. Next, ionomycin (Cambridge Bioscience Ltd), an ionophore for Ca^{2+}, was added and incubated for 5 min and subsequently images of Ca^{2+} saturated single vesicles in the same fields of view were acquired once more. Importantly, we made sure that the coverslides were not moved during the experiment so that exact same vesicles can be imaged in different conditions, which can be analysed to calculate sample induced Ca^{2+} influx quantitatively. For each field of view 50 images were taken with an exposure time of 50 ms each. The recorded images were analysed using ImageJ (National institute of Health) to determine the fluorescence intensity of each spot under the three different conditions, namely blank (F_{blank}), in the presence of an aggregation mixture (F_{sample}), and after the addition of ionomycin ($F_{Ionomycin}$). Spot detection was implemented using 'find maxima' and intensity of the spots are calculated by considering 5 pixel diameter by centering brightest pixel of the spot. Then the particular sample induced relative Ca^{2+} influx into a vesicle was calculated using Equation 3.

$$Ca^{2+}\text{influx} = \frac{F_{sample} - F_{blank}}{F_{Ionomycin} - F_{blank}}$$

Equation 3 Calculation of Ca^{2+} influx based on the fluorescence changes detected.

The average degree and standard deviation of Ca^{2+} influx was calculated by averaging the Ca^{2+} influx into individual vesicle from 16 field of views.

3.4.2 Inflammatory Response Measurement and Cell Culture

The TNFα levels were kindly measured by Dr. Craig Hughes. The BV2 cell lines were derived from immortalised murine neonatal microglia. They were grown in Dulbecco's Modified Eagle's (DMEM) supplemented with 10% foetal bovine serum and 1% L-Glutamine (Life Technologies) and incu-bated at 37 °C in a humidified atmosphere of 5% CO2 and 95% air, until approximately 1.6 x 106 cell/ml. For long duration experiments the buffer was exchanged every 24 hours. Elisa assays. To determine cumulative TNF-α production, supernatants were obtained after incubation with the Amyloid aggregate fractions over viable time frames and stored at −80°C until analysed. TNFα levels were analysed using the Duoset® enzyme-linked immunosorbent assay (ELISA) development system (R&DSystems, Abingdon, Oxfordshire, UK).

3.4.3 Atomic Force Microscopy

The AFM was performed by Dr. Simone Ruggeri. The AFM was done on bare mica (TedPella Inc., USA) substrates. The mica surface was cleaved for each sample and an aliquot of 10 μl of the sample solution was deposited on the positively functionalised surface. The droplet was incubated for 5 minutes, then rinsed by 1 ml of Milli-Q water and dried by the gentle stream of nitrogen gas. The preparation was carried out at room temperature. AFM maps were realised at least with a resolution of 1024x1024 pixels by means of a JPK nanowizard2 system (Germany), operating in tapping mode and equipped with a silicon tip (μmasch, 2 Nm^{-1}) with a nominal radius <10 nm. Images flattening and single aggregate statistical analysis was performed by SPIP (Image Metrology, Denmark) software [204].

4 Studying Amyloid Aggregates in human CSF

4.1 Introduction

The development of new drugs is strongly coupled to two factors: firstly, an understanding of the molecular mechanism of the disease to identify a therapeutic target and secondly a biological readout to monitor the beneficial effect preferentially with an easily accessible and measurable biomarker. There has been good progress in the understanding of the molecular players in the case of AD and PD over the last decades. However, monitoring the disease progression and identifying early signs clinically and biochemically has been an ongoing problem. For a long time, the only fully reliable diagnosis about the subtypes of many dementia variants was the post mortem analysis of the brain.

The first identification of amyloid proteins in a human CSF was in 1992 showing the presence of Aβ [205]. CSF is accessible with the standard procedure of a lumbar puncture and proteins will be much more readily measurable than in blood as they do not have to cross the blood-brain barrier. It was also shown that αS was present in cerebrospinal fluid in PD patients with the potential as a biomarker [187,206].

It was found in recent years for AD, that the three amyloid markers of total tau, phospho-tau and amyloid beta fragments (specifically 1-42) robustly correlate with MCI and dementia due to AD with sensitivity and specificity reaching 85–90% [207,208]. The three markers are used in combination and their diagnostic power can be explained in different ways. An increase in total tau correlates to AD pathology and can be linked to the release of tau by degenerating axons into the extracellular space [209]. High concentrations of total-tau are a sign of intense axonal degeneration that indicate fast disease progression [210,211]. The phospho-tau concentrations in CSF reflect the presence of neurofibrillary pathology [212,213].

CSF biomarkers in AD

For Aβ the situation is reversed in the correlation between the CSF levels and disease progression. In 1992 Haass and colleagues first showed that Aβ is secreted to the CSF [205], but subsequent measurements of CSF Aβ could not show a clear change in AD [214,215]. This could be accounted for by the non-specific ELISA used. The

relevant Aβ isoforms 1-40 and 1-42 were not distinguished and hence a change could not be observed [216].

It was then shown in 1995 that AD patients have reduced Aβ42 [217]. This was explained by sequestration of Aβ42 in senile plaques [218] and possible oligomerisation and matrix effects, leading to the reduced levels [207]. This measure was improved by taking into account the Aβ40 to Aβ42 ratio as this allowed to determine the levels of Aβ42 in the background of the individual Aβ production [207,219]. Aβ40 production is about ten times higher than Aβ42 and does not change in AD but the 42:40 ratio reduces even more markedly than 42 alone [216,220]. These findings have been confirmed by ELISA methods [221], luminex [222], electrocheminoluminescence immunoassay [223], and other techniques [224,225]. Not only has the decrease been confirmed but also multiple large clinical studies have confirmed the link. Hansson and colleagues [226] conducted a large multicentre studies showing consistent results throughout and with an in depth meta-review by Olsson and colleagues [227].

Overall around 90% of the MCI patients with pathological CSF biomarkers at baseline eventually progressed to AD dementia in these studies. Aβ42 levels decrease prior to onset of AD dementia by at least 10 years and prior later increase of tau and p-tau [209]. This suggests changes in Aβ precede the tau-related pathology.

For the described CSF biomarkers, especially for Aβ, it was not so clear how the drop in Aβ42 could be explained. This could be due to decreased Aβ production, decreased Aβ clearance, aggregation and deposition of Aβ in brain tissue, with lower amounts diffusing to the extracellular space and CSF, increased proteolytic degradation of Aβ, and possibly more [216]. However, the most likely explanation is the increased rate of aggregation in the brain, as an inverse correlation was shown between CSF Aβ42 and plaque load in cortical regions [218].

Other diagnostic approaches in AD

Another way of predicting and diagnosing AD uses the amyloid binding ThT-derivative Pittsburgh B (PiB) as ^{11}C-modified derivatives in positron emission tomography (PET). PiB interacts with the amyloid deposits in the brain showing increased ligand retention in cortical brain regions in AD compared to controls [228,229]. This concept has been expanded by the use of multiple ^{18}F labelled tracers for amyloids

which can have slightly different binding properties [230]. PET imaging shows good correlation with the CSF biomarkers and AD progression [229]. PiB and other amyloid beta ligands are targeting aggregated, beta-sheet structure containing protein deposits.

This beta-sheet binding property leads to predominantly labelling of compact plaques and vascular deposits as shown in post-mortem tissue [231]. This means in turn that less closely packed aggregates and amorphous plaques are not getting picked up very well but the PET imaging shows good agreement with Aβ pathology regardless of the non-comprehensive labelling of all Aβ aggregates [232,233].

Despite the fairly established biomarkers for AD, we still have not fully understood the molecular mechanisms of aggregation and pathology in the brain. With the secretion of Aβ into the CSF we have direct access to the resulting aggregate species before plaque formation. This can potentially allow us to examine structural properties of the former in the CSF. The biomarker approach described above selects for a sequence specific epitope on the protein. Alternatively, we can, orthogonal to mesoscopic PET imaging, use ThT to image the microscopic aggregates in the CSF [77]. Despite some potential diagnostic value, this could more importantly help us better understand the nature of the aggregates in the brain.

Multiple anti- Aβ antibodies failed in phase III clinical trials recently. Most prominently bapineuzumab. There is a variety of explanations for this which I will discuss in more detail in the following chapter 4.2.3. It is important to understand however, the correct pathologic state of the neurotoxic protein. Otherwise potential non-harmful forms might be wrongly depleted and worsen the condition. There are two things I will examine in the following. Firstly, can we learn more about the number and structure of the aggregates in CSF by directly observing it via SAVE. Is the aggregate number and structure different between AD and HC in the CSF? This can potentially help translate some of these properties in to *in vitro* systems to study the correct aggregation states. Secondly, if we have a method of measuring aggregates in the CSF, can we inhibit their effects? This can help us evaluate e.g. antibodies in preclinical trials on human aggregates.

CSF biomarkers in PD

αS as a biomarker for PD cases is still not fully validated. The central role of αS in the role of pathogenicity and the correlation between the neurotoxicity and its levels make it an attractive biomarker candidate. There have been conflicting results as to whether the levels of total αS are linked to the disease progression and suitable as a biomarker [106,234-237]. The most recent results suggest no link for total CSF αS levels and PD. Some results also suggest a link between low levels of αS and tau in CSF [238]. All this however just shows even more the need to develop a prognostic and diagnostic marker for PD. Horrocks and colleagues were able to distinguish PD and HC CSF samples by the number of ThT active aggregates imaged with high-resolution TIRF microscopy [77]. This made the technique a promising candidate as diagnostic tool (Figure 10). Furthermore, it might help us understand the aggregates present in the brain.

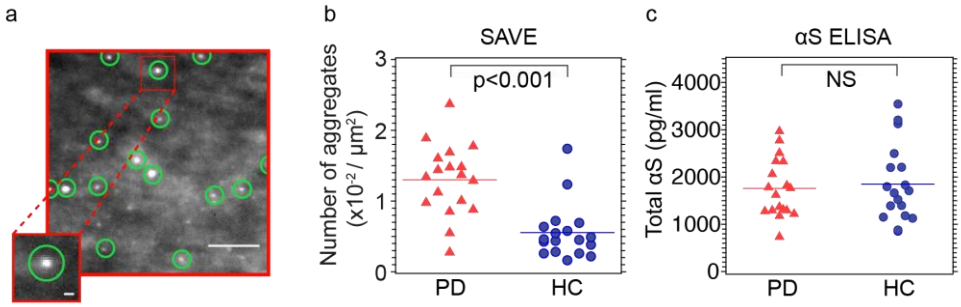

Figure 10 The SAVE method allowed to distinguish PD patients and HC patients by counting the number of ThT-active aggregates in the CSF. (A) shows an example image of a CSF patients CSF imaged with SAVE and the green circles show the counted aggregates. (B) and (C) show the direct comparison between the PD and HC samples as analysed with SAVE and an αS specific ELISA which does not show any difference between the samples in contrast to the SAVE method. Figure reprinted from Kundel at al. [37].

The following section will consist of two main parts. Firstly, the expansion of the SAVE method with various other extrinsically fluorescent dyes and the horizontal method transfer to AD CSF samples. Secondly, I will demonstrate how SAVE and other methods helped to understand why the antibody bapineuzumab might not have been successful in phase III clinical trials and how antibody effects differ between *in vitro* aggregated protein and aggregates in CSF.

4.2 Results

4.2.1 New Extrinsically Fluorescent Dyes to improve SAVE

High resolution microscopy coupled with extrinsically fluorescent dyes can be used to visualise unlabelled single amyloid aggregates. In this chapter I show how parameters for the imaging of individual aggregates of αS can be optimised, using five different dyes. I will show that a dimer of Thioflavin T gives improved performance in this particular application. I will also show effects and how the sample handling can affect the outcome.

The oligomeric states of αS were found to promote elevated levels of reactive oxygen species and Ca^{2+} in cells, membrane permeabilisation and play an important role in seeding and therefore elevated disease progression [239]. It is likely that absolute protein concentrations which are dominated by the monomer, often used in ELISA based diagnostic tests, might not be the best parameter for disease progression. Rather, a test which determines the relative concentrations of protein aggregates may be a better solution. Single amyloid visualisation through enhancement (SAVE) addresses this problem by measuring the individual aggregates (Figure 11) found in human CSF [77]. We explore if the technique can be improved or expanded with different beta-sheet binding dyes to enhance its capabilities.

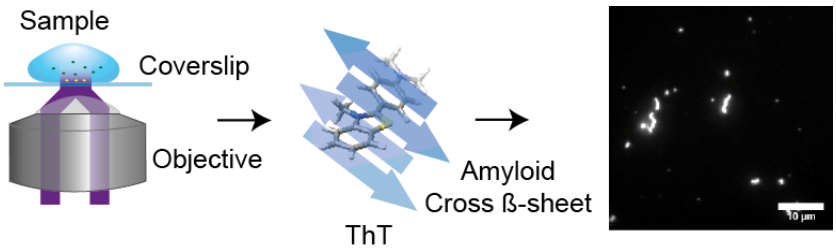

Figure 11 Schematic of the SAVE method showing a simplified view of the single aggregate visualisation through enhancement with the sample deposited on a coated glass coverslip and imaging in TIRF mode after the addition of ThT and subsequent data acquisition and analysis. The scale bar is 10 µm showing αS aggregates.

The SAVE method is particular useful for two reasons. Firstly, because it does not require a covalently attached fluorophore, which is not easily done in a biofluid. Secondly because it enables the size distribution of aggregates to be monitored within a single sample, which is not possible with an ensemble method. Despite the surge of oligomer specific ELISA tests, these still usually select positively for one epitope in the ensemble measurements. That means even with a specific epitope we will only be able to see one ensemble response to the overall presence of the structural binding sites.

This means we would for example not be able to distinguish between many aggregates with little binding sites and little aggregates with many binding sites.

I selected five dyes that have been shown previously to bind to beta-sheet structures present in amyloid aggregates. We compared ThT, a custom made PEG2 linked Thioflavin Dimer (DiThT-PEG2), DCVJ, BTA-1 and Congo Red for testing (Figure 12). To the best of my knowledge, no other studies used extrinsically fluorescent dyes to image aggregates in biofluids. This makes the explorative nature of this work important.

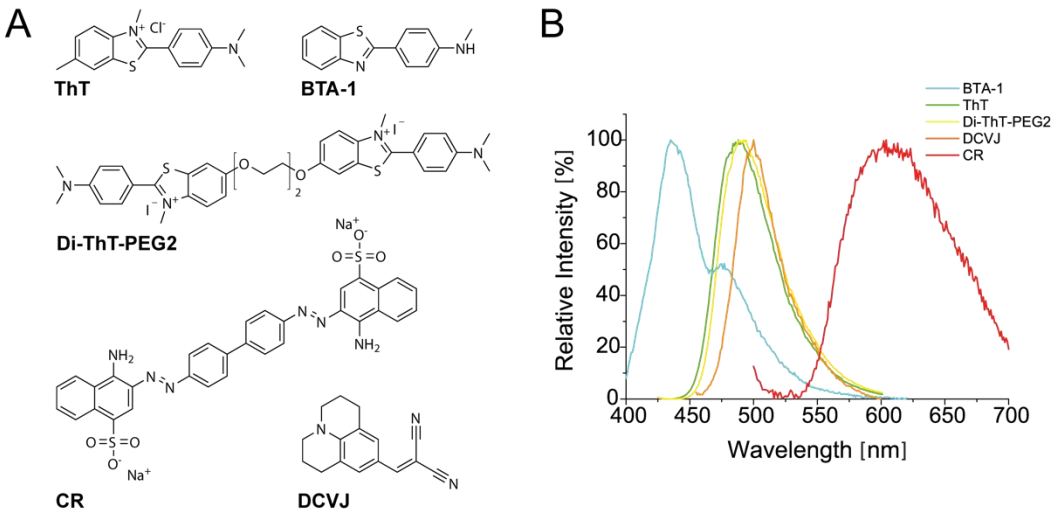

Figure 12 (A) shows the chemical structures of the extrinsically fluorescent dyes used to test for ThT alternatives. The dyes are ThT, Di-ThT-PEG2, BTA, DCVJ and CR. (B) The respective emission spectra of the tested dyes upon binding to αS aggregates is shown. All spectra are normalised for their intensity.

The important properties of the dyes were tested for (1) the usability for SAVE with a sufficient signal to see individual aggregates (2) the optimal dye concentration to balance false positive and signal to noise with a constant protein concentration and (3) the most promising dyes, namely ThT and DiThT, were tested at various aggregate concentrations at their optimal imaging concentration.

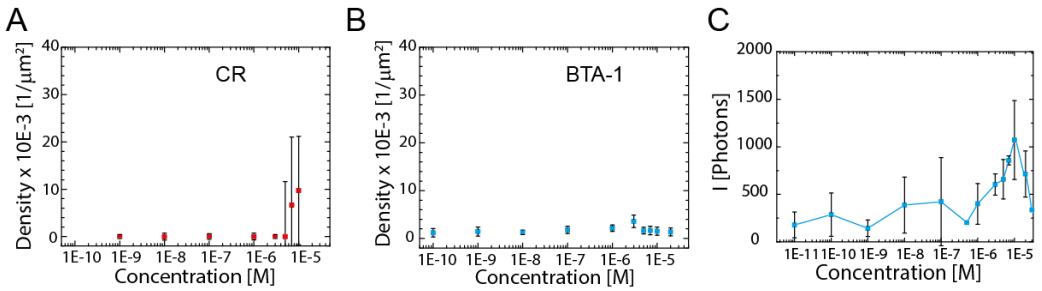

Figure 13 (A) The aggregate density measured with CR in the presence of aS aggregates with the SAVE method. We cannot see an increase in aggregate density until very high dye concentrations which have high error bars due to false positive background effects. (B) BTA-1 doesn't show any aggregates either. (C) An example of the lognormal fitted intensity distribution for BTA-1 has been plotted. As the overall number of detected spots is so low, the fits have big errors and doesn't allow us to get conclusive results with either dye. Hence, they are not suited for the application.

Where ThT, DiThT-PEG2 and DCVJ show good signal at various dye concentrations CR and BTA-1 show no signal (Figure 13). This has all been analysed using the methods described in chapter 3.3. In brief, we focus on all puncta signals above background to see if BTA-1 and CR are suitable. Even though they are known to bind beta-sheet structures, their photochemical properties are not sufficient to image single aggregates with the proposed method.

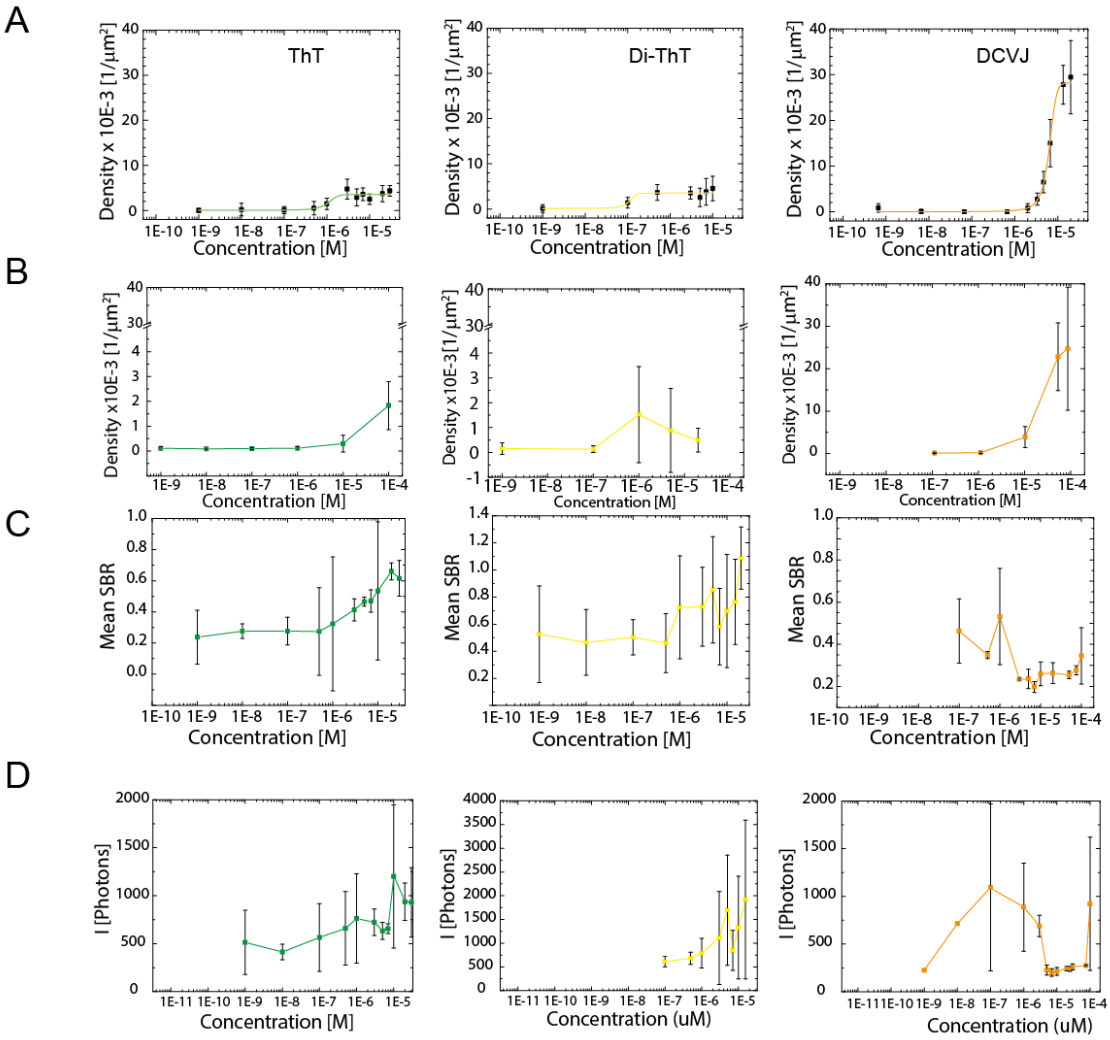

Figure 14 The data of 3 technical repeats for each data point of ThT (green), Di-ThT (yellow) and DCVJ (orange) are shown. All graphs show the readout as a function of dye concentration. (A) shows the aggregate density without false positive correction. (B) shows the density of detected 'aggregate' in the absence of protein, a measure of the false positive rate. (C) The mean SBR is calculated by fitting each cumulative histogram of each reapeat with a lognormal function as it bests represents the distribution. The SBR is calculated for each aggregate individually between the peak intensity and the surrounding pixels (D) The Intensities have also been fitted with a lognormal function as described for the SBR. At very low concentrations the fitting failed and is hence not displayed, as almost no aggregates were detected to start with.

To compare binding affinities the binding curves have been normalised after fitting (Figure 15 A) with midpoint and saturation point. Fitted to a sigmoidal curve the half point is 1.1±0.3 µM, 0.1±86 µM and 6.3±0.4 µM for ThT, DiThT and DCVJ respectively. The higher binding affinity of the ThT-Dimer is probably due to its dimeric structure. DiThT shows the highest affinity to αS with ThT about 10-fold lower and DCVJ even lower. I distinguish two types of 'background': (1) SBR background as a function of signal strength to amorphous background noise which

shows how sensitive the dye is, if an aggregate is present and (2) false positive background for dye molecules giving false positive signals, when no αS aggregates are present. The SBR is calculated locally for each fitted maximum and is hence not susceptible to changes in the overall illumination of the TIRF field. The false positive background for both ThT and DiThT does not increase at higher concentrations and stays consistently low over the whole range (Figure 14 B). However, the false positive background of DCVJ is significant above ~10 μM (Figure 14 B). There is an overall trend of increased SBR as function of aggregate density but there is no clear optimum (Figure 14 C). The optimal dye concentration for imaging is hence largely dominated by two factors. The low limit of the dye concentration is determined by the detection of the aggregates while the upper limit is determined by the increasing amounts of false positives. The mean intensity is fairly constant with an increase at higher dye concentrations with the high deviations make interpretation difficult. The exception here is DCVJ where the increase in false positives is matched by a decreased in intensity. This suggest that the false positives are bright enough to be above threshold but with overall low intensity and start dominating in presence over the aggregates.

For above absolute signal intensity and the SBR ratio the histogram of the intensity for each set of data at a given concentration of dye was fitted to a lognormal distribution and is plotted in Figure 14 C, D. The photon count of the three lognormal fits was calculated using Equation 1 using values as stated in the Table 2 section.

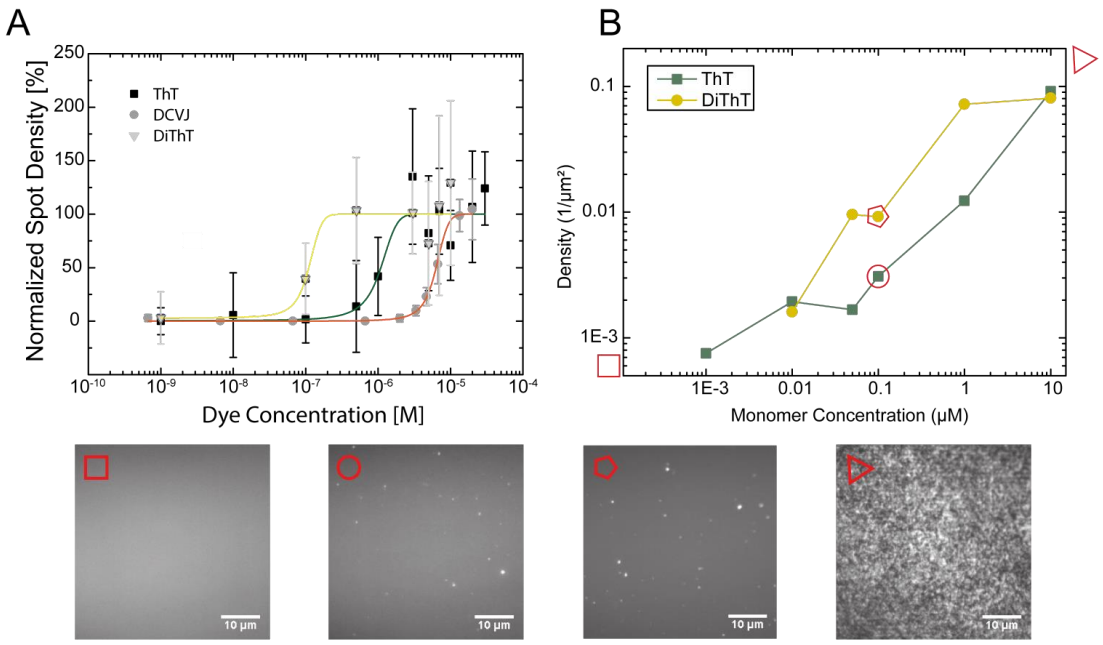

Figure 15 (The binding affinity for Di-ThT-PEG2 (yellow), ThT (green) and DCVJ (orange) fitted to a sigmoidal dose response normalised to its maximum density. Each point is the mean of at least three biological repeats each consisting of 27 recorded field of views (11x10³ µm²) with the standard deviation of each repeat as error. (B) The average density and as a function of protein concentration after 22h aggregation at fixed dye concentration of 10 µM ThT (yelow line) and 1 µM Di-ThT-PEG2 (green line). Each density value is the average of 27 field of views. Representative image data for the various concentration is shown below. The square is a sample for a monomer concentration of 1E-4 µM and the triangle for 100 µM. The density is equal to the background density and therefore not included in the plot.

Comparing the density of detected aggregates at the same protein concentration the saturation for ThT and DiThT is in the same regime indicating that neither detects more aggregates above its Kd. DCVJ though has a higher saturation density. This is due to increasing false positive events as shown in Figure 14 A, B. This could be caused by precipitation or micelle formation of the dye in the aqueous solution or unspecific binding to the PLL- coated surface.

Changing the protein concentration over with fixed dye concentration can give us insight into relative detection limits. As shown in Horrocks et al. [77] with an enriched oligomer concentration the lower detection limit for these is 10 pM. In our case to compare ThT and DiThT I chose to aggregate αS to a mostly oligomeric state without specifying the oligomer concentration. Both dyes show a linear relation between the density and the protein concentration with DiThT appearing to be slightly more sensitive. At very high protein concentration the individual signals cannot be separated anymore. (Figure 15).

Sample handling procedures

I also tested the effect of the standardised spinning of the CSF samples post lumbar puncture and whether the freezing of the samples for storage has an effect on the outcome of our method. The centrifugation is a standard procedure to ensure no cells in the samples from piercing the skin before taking the sample.

Prior to assay development a variety of controls were examined to exclude effects of the CSF sample preparation, processing and storage. CSF samples are obtained via lumbar puncture done by a trained clinician on the patient. In most cases the samples get subsequently centrifuged at 2000- 3000 g for 10-15 mins to remove cell debris and blood contamination. The samples get frozen on dry ice or flash frozen in liquid nitrogen and stored at –80°C. As the SAVE method is able to detect and distinguish different macromolecular structures and not only protein abundancies it was crucial for us to control for preservation of these. There has been evidence that freeze-thaw cycles can generate smaller size amyloid fibers and that storage conditions alter biomarker results [240-242]. To avoid biasing our results by generating smaller fibril fragments through freeze thaw cycles a fresh CSF sample (appr. 30min to 1h post spinal tap) was used to measure the effect. This was compared to the same sample frozen in liquid nitrogen and analysed later. No appreciable difference was observed in the oligomer count but the results show a small reduction of aggregates overall (Figure 16).

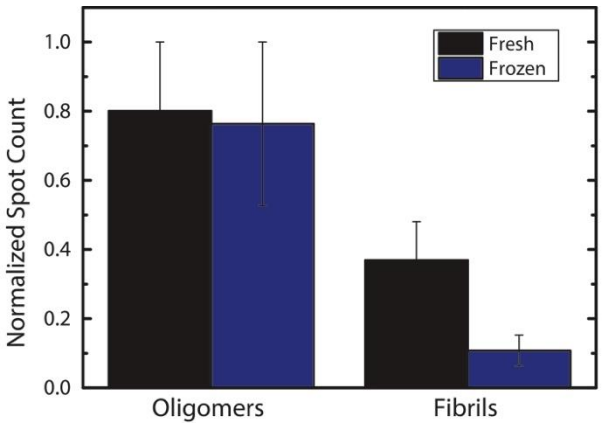

Figure 16 SAVE imaging of a fresh and a frozen CSF sample. The mean of 27 field of views with the standard deviation as error shown. The overall aggregate count is reduced due to the freeze thaw cycle, but the change is overall small. It appears as if the non-diffraction limited fibrils are affected more strongly.

This effect might be smaller than in an AD sample, as the sample was from a patient with no diagnosed AD or PD and is therefore probably not showing the same amount of oligomers and fibrils as it would in the case of a PD or AD patient.

However, to allow for aliquoting samples for multiple repeats we kept one freeze-thaw step in any further sample handling and avoided subsequent freeze-thaw cycles.

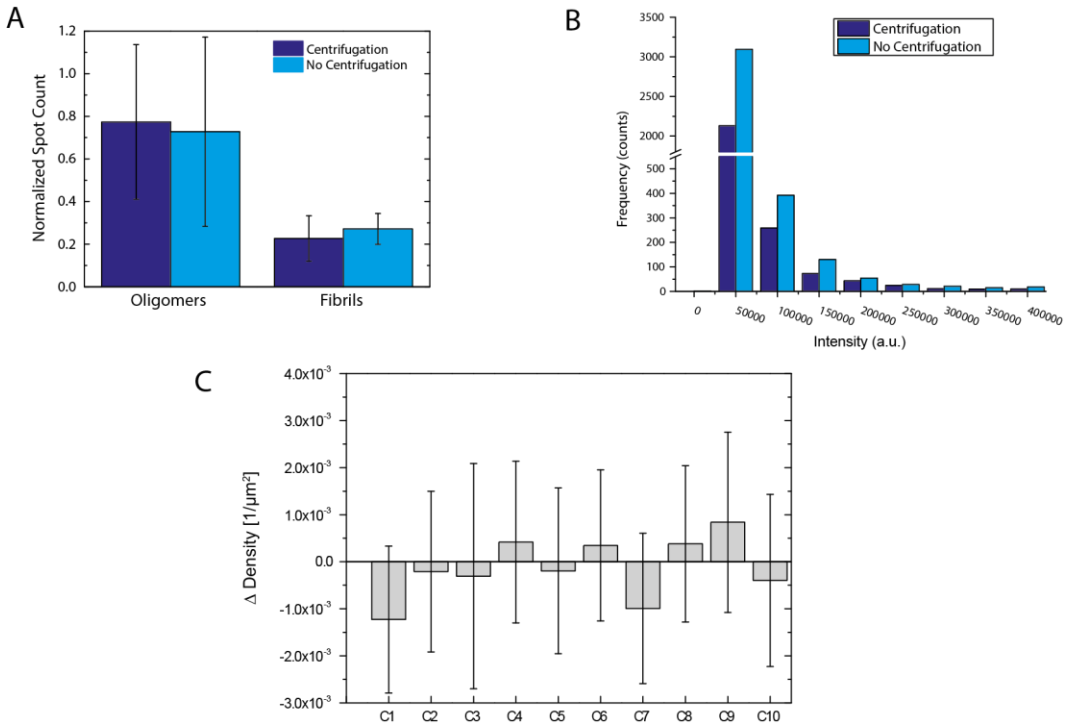

Figure 17 Comparison of different centrifuged and non-centrifuged CSF samples. (A) The normalised spot count is shown with the normalised mean of 3 repeats with 27 fov each with the standard deviation of as error. No depletion of one or the other species can be observed. (B) A histogram of the intensities shows now particular influence on large or small aggregates. The intensities from all three repeats are binned. (C) The aggregate density difference of a different set of deidentified patients. Each bar is the difference of centrifuged vs non-centrifuged of one repeat with 27 field of views with the error bar the higher standard deviation of the two values. Again, no clear influence of the centrifugation can be observed.

To examine the influence of spinning, a frozen unspun sample from a single sample out of a PD cohort and a set of AD patient samples was used. The SAVE technique was applied, and results are shown in (Figure 17). There was no clear trend in the sample set of the AD cohort. All samples have been de-identified for research use and then divided into spun at 2000 g for 10 min at 4°C and unspun. The results are comparable for the PD sample with the speed slightly higher at 3000 g for 10 min at 20°C. A closer look at the intensity distribution to account for depletion of larger species did not give a difference either. The speed of the centrifugation seems to be low enough to not bias the results in our technique. These finding suggest that the sample procedure is not affecting the SAVE technique in its present form. Therefore, it is necessary to develop further parameters to get a better and predictive distinction of both PD and especially AD CSF samples.

In both cases however it was not possible for us to access fresh and non-centrifuged confirmed AD or PD CSF. It is conceivable that the presence of ThT-positive aggregates was overall different in the tested CSF samples. Furthermore, as

the patients required a spinal tap to analyse their CSF they are most probably in treatment for some form of neurological disorder which could potentially influence the outcome of the experiments. Nonetheless within the given circumstances it appears that neither the mild centrifugation nor the storage at -80°C affect the outcome of the SAVE measurements.

4.2.2 SAVE to search for AD biomarkers in CSF

After the SAVE method was used and assessed for αS we tried to establish if this method could be readily applied to CSF samples from AD patients. ThT is known to bind to Aβ protein as it exhibits the same extended beta-sheet structures that required for fluorescent enhancement of the dye. The hypothesis was that if there was a difference in the number of amyloid aggregates in the CSF we should be able to detect that difference. We measured a sample cohort of overall 37 samples with a clinical diagnosis of AD or as HC. All AD positive samples had protein levels of Aβ1-42 < 600 ng/L, T-tau > 350 ng/L and P-tau181 > 80 ng/L according to Toledo et al. [243]. The details (protein levels, gender, age) of the cohort patients are listed in (Table 3). The SAVE analysis showed however no statistically significant difference between the two sample cohorts (Figure 18) in contrast to the results in PD (Figure 10) [77]. Neither the number of the aggregates nor their intensity changed significantly (Figure 18 A, Figure 19). I measured overall 37 samples with 18 in the AD cohort and 19 in the HC cohort. Even when comparing the mean number of aggregates in each sample the difference is not sufficiently significant.

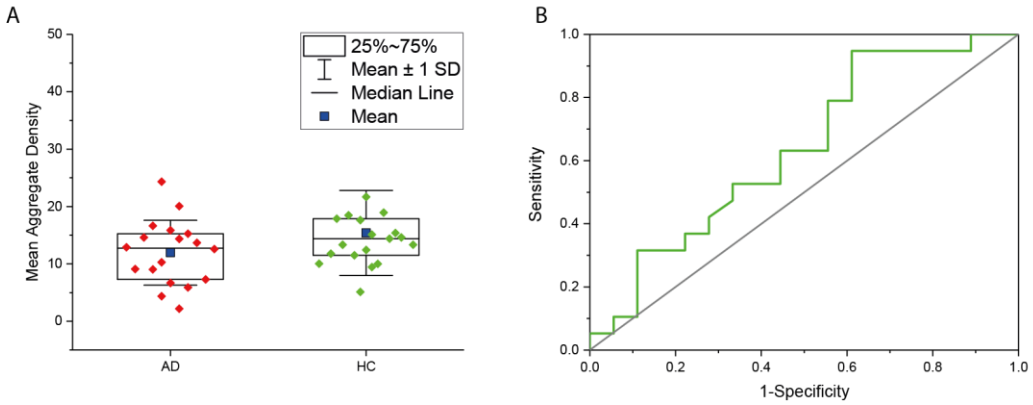

Figure 18 (A) Comparison between AD CSF samples (red) and HC CSF samples measured with the SAVE technique. The mean line is shown with 25 and 75 percentile and the error bar showing the SD of each cohort. ANOVA test shows no significance with p = 0.1237 between the 18 and 19 samples in each cohort. (B) A ROC curve in green with the random chance line in grey is shown comparing the AD and HC cohort. The area under the curve is 0.635 which means the test is overall poor in discriminating AD from HC patients.

ROC curves are frequently used to assess the diagnostic power of clinical test. Figure 18 B shows the ROC curve for the AD and HC dataset. The further the line moves to the upper left the better the specificity and sensitivity of the test to distinguish AD from HC. In my case the curve deviates from the diagonal line which is equivalent to complete randomness only very little. This means the test is not suitable to distinguish samples in the cohorts. Horrocks et al. furthermore observed a shift in the intensities

in the case of the αS aggregates [77]. The cumulative histogram of the intensities of all the detected aggregates shows a small deviation (Figure 19).

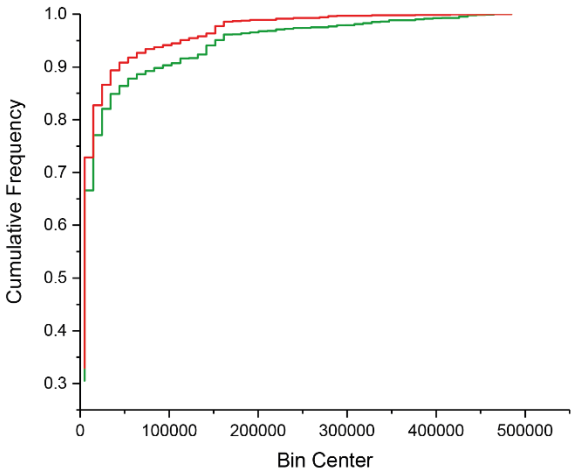

Figure 19 The cumulative frequency histograms of the AD (red) and HC (green) cohort is shown as a function of Intensities. The shape of the curve is mostly very similar with only a small deviation in the mid region.

To test whether this shift was sufficient to improve distinction between AD and HC improves I picked a randomly selected subset of samples with varying thresholds. (Figure 20 A) shows the box plot of all aggregate intensities of the ten-patient subset. The selected thresholds are indicated vertical bars. (Figure 20 B) shows the resulting mean intensities of the subsets selected via the indicated thresholds showing now improvement over the comparison of the number of aggregates. These findings however lead on to further studies in chapter 4.2.3. I go on to study structural properties of aggregates in human CSF under the effect of various antibodies and this is complemented by means of Ca^{2+} influx measurements.

A possible explanation of the same level of detected ThT-active aggregates which I find in the AD and HC CSF could be the fact that AD has a mixture of aggregates present throughout the disease. It has been shown with ELISA that the levels of total Aβ42, Aβ40 and tau develop nonlinearly throughout the disease [207]. In this cohort the threshold for determining disease was defined by the results of the ELISA. These ELISA tests, even though they can predict disease progression, do not take into account clinical diagnosis and some of the HC cohort might still develop AD or other neurodegenerative diseases further down the line. The results could also be influenced by bias in protein levels due to e.g. tauopathies that clinically would not develop into

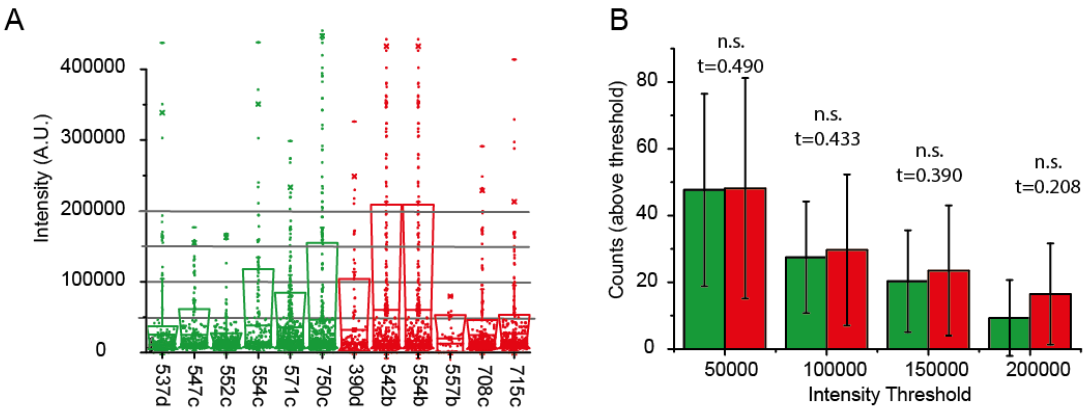

Figure 20 (A) Box plot of individual peak intensities for a set of 5 sample each to specifically test various intensity thresholds to distinguish AD from HC. The box shows the 25 and 75% percentile with the mean line and standard deviation indicated by the bars. (B) Comparison between the indicated thresholds counting aggregates above the respective intensity thresholds. The box represents the mean between all 5 samples with the standard deviation as error and the result of the students t-test indicated above each comparison.

AD but would still show increased tau levels. Together these factors could all contribute to the result that SAVE is not suitable as a tool to predict or diagnose AD.

Table 3 Overview of all measured AD (red) and HC (green) CSF samples with the mean aggregate density and the standard deviation of all 27 field of views and the corresponding ELISA results, age and gender.

ID AD/HC	Mean Density	Std Dev	Tau ng/L >350	Aβ ng/L <600	Ptau ng/L >80	Age	Gender
390d	6.678	3.973	1180	290	117	77	M
542b	14.357	8.578	984	556	88	75	F
548b	10.285	8.995	1360	505	137	64	F
554b	20.071	16.628	982	553	112	80	F
557b	2.178	2.464	835	491	90	82	F
708c	13.678	6.279	703	562	85	71	F
715c	15.857	11.407	778	330	80	72	M
720c	9.035	4.039	750	392	90	75	F
722c	5.892	4.279	518	334	91	77	M
731c	9.107	5.122	780	546	94	20	F
734c	24.321	21.840	974	515	87	75	M
757c	16.642	13.583	873	234	88	63	F
788c	14.607	11.802	984	556	88	75	F
800c	12.571	5.659	1310	532	143	82	M
830c	7.285	5.450	826	591	167	52	F
865c	12.892	11.902	720	508	104	72	F
872c	15.250	8.420	768	522	102	85	F
884c	4.357	4.638	1200	315	165	59	F
883c	12.428	6.613	193	758	33	70	M
537d	11.500	5.261	297	716	35	65	M
547c	10.000	6.546	329	1250	53	78	M
552c	15.107	11.505	264	617	50	68	F
554c	9.428	6.945	324	809	43	69	M
571c	17.642	17.489	332	678	46	62	M
750c	18.928	8.119	283	1050	39	69	M
768c	18.464	8.865	115	691	38	77	M
777c	13.321	7.474	214	877	36	78	M
809c	14.392	7.422	130	729	28	69	F
812a	15.392	8.234	106	789	21	62	F
815a	11.785	5.459	266	698	31	73	F
820a	5.107	4.065	134	675	27	60	M
821c	14.607	8.269	250	847	42	70	F
823c	41.214	52.212	120	923	25	68	F
842c	10.035	5.984	253	860	46	73	M
847c	21.678	15.264	303	977	49	73	M
870c	13.321	8.477	263	706	40	64	F
879c	17.892	17.475	188	604	31	82	F

Expansion of SAVE via a clusterin competition assay

The extracellular chaperone clusterin binds to oligomeric Aβ42 aggregates with high affinity. Recent findings suggest that the molecular chaperon clusterin can help preventing cell toxic effects of Aβ aggregates [120]. Clusterin or Apolipoprotein J is a multifunctional disulfide linked heterodimeric glycoprotein composed of two 40 kDa subunits [244]. The CLU gene locus was associated to AD in genome wide studies [245,246]. It has been shown that the extracellular Clusterin sequesters oligomeric forms of the Aβ40 peptide in long lived stable complexes suppressing Aβ40 aggregation with a similar binding occurring for Aβ42 [247]. Furthermore clinical studies confirmed a potentially important role for clusterin in the earliest stages of the AD neurodegenerative process and suggest independent effects of clusterin and p-tau on Aβ-associated atrophy rate of the entorhinal cortex and hippocampus [248].

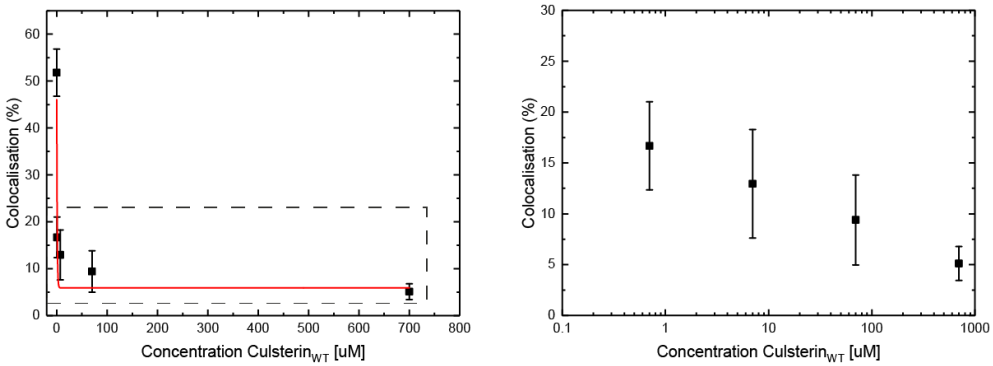

Figure 1 Co-localisation competition with fluorescently labelled Clusterin and unlabelled Clusterin binding to αS Oligomers. The left graph shows the percentage co-localisation based on ThT with the concentration of the pre-incubated Clusterin given on the x-axis. Each point is the mean of three experiments each with 27 field of views and the error is the standard deviation of the mean. The data is fitted to a sigmoidal dose response function with an EC50 of 3.21 x 10^{-6} ± 0.40 x 10^{-6} µM with an r^2 of 0.91 for the fit. The right hand shows the dashed area with same data on a logarithmic scale.

The underlying rationale for the competition assay is the observation, that clusterin binds to oligomeric amyloid proteins such as αS oligomers [249]. It bound to αS aggregate already at sub-stochiometric ratios. At low clusterin: substrate ratios the amyloid formation was increased while high clusterin: substrate inhibited amyloid formation [249].The following *in vitro* data suggest a possibility of the use of fluorescently labelled clusterin in a competition assay as a probe to explore αS - clusterin interactions in CSF. To test this hypothesis, I used αS oligomers and pre-incubated them with varying concentrations of clusterin. I then added a fixed concentration of 1.5 nM

AF647 labelled clusterin and analysed the colocalisation with the ThT active aggregates.

The difference in co-localisation could be used in addition to the density of the ThT active oligomers to improve diagnostics. Figure 21 shows the differences of co-localisation dependent on the added amount of unlabelled wild-type clusterin with unchanged amount of labelled clusterin. The translation of this principle into CSF could potentially distinguish differences yet undetected by the current method by adding an additional parameter. CSF clusterin has been associated with PD, but the results are unclear to how they are linked [250-254]. With the proposed method I could detect if in the PD case more clusterin was associated with the oligomers and vice versa even if the overall aggregate yield was equal depending on the co-localisation rate. The combination of SAVE and clusterin colocalisation can help understand aggregates in our PD and HC CSF samples and possibly improve diagnostics. This system has not been further explored however as I have focused my efforts on detailing more of the structure of the Ca^{2+} inducing aggregates in human CSF of AD patients as described in the following chapter.

4.2.3 Structural Effects of Antibodies on Aβ42 aggregates

The development of new therapeutic antibodies led to the prominent and promising candidate Bapineuzumab developed by MedImmune which failed in Phase III clinical trials [255,256]. One of key questions was, why an antibody against Aβ aggregates which are linked to the disease was not successful. A therapeutic strategy in AD is to target the small soluble protein aggregates, in particular in the case of Aβ42, to reduce their toxic effect. A lack of understanding of the precise composition and structure of the aggregates *in vivo* makes this however a challenging task. We suggest that the combination of a single vesicle and single cell based ultrasensitive measurement of calcium influx and single aggregate imaging can help preclinical tests with aggregates that resemble more closely the *in vivo* situation. I will describe the assays we use briefly. Importantly all assays use very little sample volume (<10 ul) which makes it possible to measure, compare and screen with the precious resource of the human CSF. This all makes it as suitable approach to characterise potential therapeutic agents in CSF.

A discussed earlier the small soluble aggregates are a potential target for treatment. Especially aggregates for human sources are of interest. Isolated aggregates from human sources such as the soluble fraction of brain homogenates have been used [29,257]. The preparative steps involved however could alter the properties of the notoriously transient aggregates. The suggested methods do not involve preparative steps but use the CSF directly in the assay. There have been few other experiments involving CSF without further preparative steps, namely by Klyubin and Walsh showing that aggregates in CSF can induce long-term potentiation deficits in brain slices which can be suppressed by antibody addition [257,258]. CSF is suitable as a representation of the extracellular processes in the brain as it freely exchanges in with interstitial fluid surrounding the brain. It has also been shown that AD CSF can cause cell death, which was reduced by the addition of extracellular chaperones [259].

We have shown that picomolar levels of Aβ oligomers can induce Ca^{2+} influx into neuronal cells by local dosing via a nanopipette and via a quantitatively measuring the Ca^{2+} influx into vesicles [260]. As I showed previously we can image single aggregates of amyloid beta with the SAVE method. With these methods I will characterise the protein aggregates present in the CSF of AD patients and control individuals. I

furthermore test the effectiveness of a single chain nanobody raised against amyloid beta Nb3, clusterin and the antibody bapineuzumab and their effects on the aggregates.

The structural characterisation was done in parallel with a high-throughput Ca^{2+} influx assay and a single cell Ca^{2+} influx assay. I will include the results of the two assays as part of the integrated research to complete the story but will focus on my own work. regarding the structural changes.

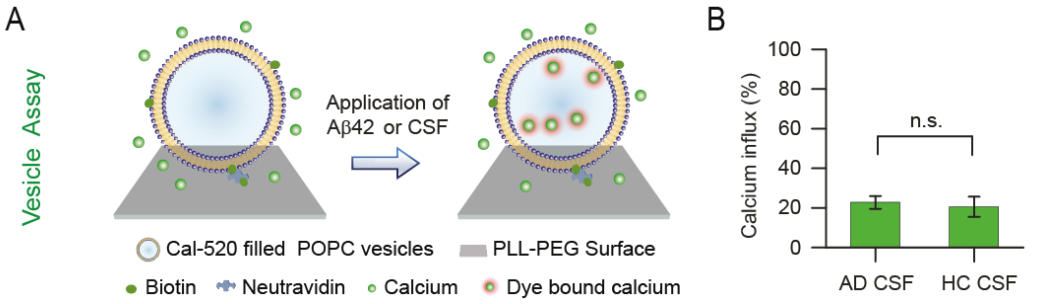

Figure 22 (A) Schematic of the vesice assay to measure Ca^{2+} influx due to AD and HC CSF. POPC vesicle filled with the calcium sensitive dye Cal-520 are tethered to the surface of a glass coverslide. Upon addition of addition of the sample (Aβ or CSF) the increase in fluorescence can be observed due to the Ca^{2+} in the surrounding buffer solution entering the vesicle. The addition of an ionophore allows the normalisation of each individual vesicle signal and hence a quantitative measurement. (B) No significant difference in the Ca^{2+} influx due to AD and HC CSF is observed. Full statistical details can be found in Table 4.

The starting point was the measurement of Ca^{2+} influx with the high throughput vesicle assay induced by AD CSF and HC CSF. There was no significant difference between the samples (Figure 22). The ultrasensitive measurement of calcium into vesicles is achieved by tethering POPC vesicles filled with the Ca^{2+} sensitive dye Cal-520 via a biotin-neutravidin interaction to a glass surface. These are spaced in a way that each vesicle can be detected individually on a high resolution TIRF microscope. The surrounding medium contains Ca^{2+} which can be detected when membrane disruption or perturbation due to amyloid aggregates leads to Ca^{2+} influx. After addition of an ionophore the maximum intensity of each fluorescence signal in each vesicle is determined to allow for a quantitative measure of the Ca^{2+} influx. This method allows detection of aggregates at very low concentration with the use of minimal amount of sample per measurement (<10 ul) [92].

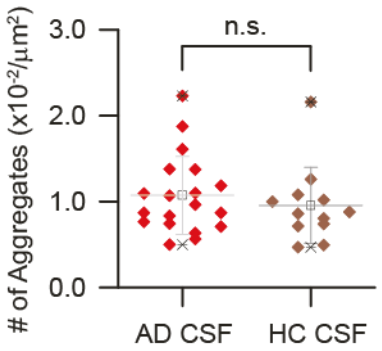

Figure 23 Comparison of the number of aggregates found in the AD CSF patients and HC CSF patients used in the vesicle and Ca^{2+} assay. The difference in the number of aggregates is not significant. The mean line with the standard deviation as error is shown. 5 of the AD CSF samples of this cohort were measured by Dr. D. Whiten.

Secondly, the SAVE imaging with ThT showed no difference in the number of ThT-active aggregates (Figure 23). This is consistent with the findings described in chapter 4.2.2. These findings suggest that a similar number of aggregates in AD and HC CSF cause the Ca^{2+} influx. The results are also consistent with previous findings with aggregate specific ELISA-based detection. These neither detected a clear difference between AD CSF and control CSF [136,261].

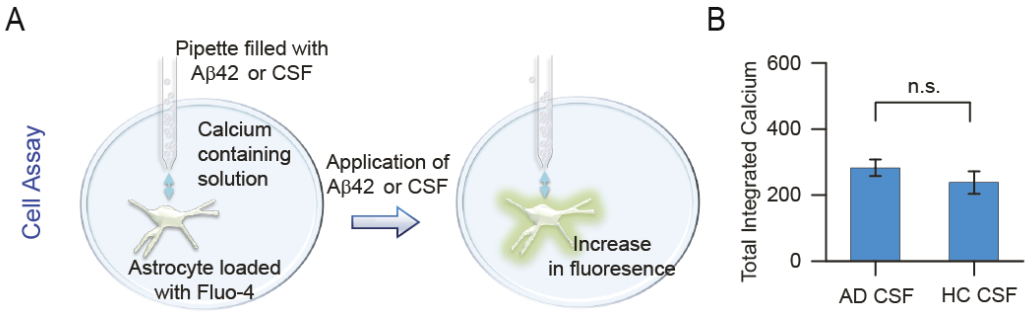

Figure 24 (A) Schematic of the SICM experiment to measure Ca^{2+} influx into astrocytes with the Ca^{2+} sensitive dye Fluo-4 and the use of a nanopipette to deliver the aggregates locally (Aβ or CSF). The astrocytes are filled with the Ca^{2+} sensitive dye Fluo-4 and surrounded by a Ca^{2+} containing bath solution. Upon delivery of the sample the increase in fluorescence is measured with a highly sensitive TIRF microscope. (B) The total integrated Ca^{2+} signal after addition of both AD and HC CSF does not show a significant difference in the cell assay. Full statistical details can be found in Table 5

A SICM setup with a nanopipette dispensing the CSF onto single cells was used to measure the calcium influx into astrocytes as described previously [260] (Figure 24 A). In this technique local dosing reduces the diffusion time to the cell surface, leading to detectable Ca^{2+} influx at low picomolar concentration. For the directed delivery of the CSF onto cells we use a nanopipette setup as described before [260]. A SICM setup is used to control the distance of a nanopipette over the surface of a cell (Figure 24 A).

The delivery of the reagents has previously been measured and modelled [262]. The sample is delivered to a surface area of about 1 μm^2 with a distance of the pipette of about 300 nm above the cell. The cells are filled with the Ca^{2+} reporter dye fluo-4 and the bath solution is filled with Ca^{2+}, to report any Ca^{2+} influx. This method allows the aggregates and CSF respectively to be delivered on small surface area, but the small cell to tip distance also reduces the diffusion distance for the aggregates before they reach the cells. This increases the local flux of the aggregates. This setup allows us to very sensitively measure the Ca^{2+} influx, in this case in to astrocytes, which reflect a realistic cell membrane in comparison to the POPC vesicles. Again, we did not see a significant difference in AD and HC but in both cases Ca^{2+} influx was observed (Figure 24 B).

After establishing the baseline for the Ca^{2+} influx the techniques helped to characterise the nature of the aggregates present in CSF. We tested the effectiveness of a single chain nanobody against Aβ, the extracellular chaperon clusterin and bapineuzumab.

I tested bapineuzumab biochemically for binding to Aβ aggregates with a dot-blot and a labelled anti-human secondary antibody (Figure 25). This confirms that the antibody used are all native and binding to the aggregates. The Nb3 testing is not shown as this was done by Erwin DeGenst and clusterin binding was confirmed in previous studies of the same batch.

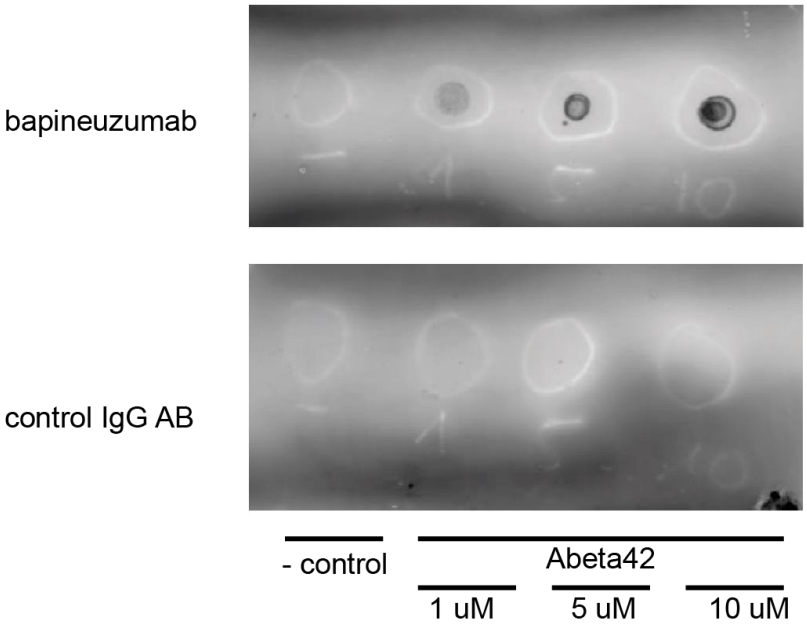

Figure 25 Dot-blot of bapineuzumab and the control IgG antibody compared at increasing concentrations of Aβ42 aggregates with the monomer concentration shown. There is a clear concertation dependent increase in the known binder bapineuzumab, whereas the control antibody is not binding to the Aβ42 aggregates. The control is an empty buffer only control.

As described earlier, there was no difference in the Ca^{2+} influx between the different CSF samples and no difference in the number of ThT-active species (Figure 23). This is in agreement with aggregate specific ELISA-based detections [136,261]. This suggests that the number of aggregates causing the Ca^{2+} influx is comparable.

To identify if there is a qualitative difference in the aggregates we added the extracellular chaperon clusterin to the CSF prior to our measurements. The extracellular chaperones that can reduce the toxicity of CSF and has been shown to bind to misfolded and aggregated proteins. As described earlier clusterin has been shown to bind Aβ42 oligomers at sub-stochiometric concentrations [249,259]. Clusterin can bind to oligomers in multiples and it can decrease the Ca^{2+} influx into single vesicles [92,118,247]. The affinity of clusterin for the oligomers of Aβ is very high as only 100 pM of clusterin halved the Ca^{2+} influx in the vesicle assay [92].

Clusterin suppressed the Ca^{2+} influx in both the vesicle assay and the cell assay. This suggests that the influx is indeed caused by protein aggregates. Clusterin is already present in the CSF with concentrations of about 90 nM both in HC and AD [263]. This implies that the concentration of clusterin is not high enough in the CSF which agrees with reports of toxicity reducing effects of high clusterin concentration [259].

The next step was to use a Aβ42 specific single-chain nanobody Nb3 to see if we could reduce the effect Aβ specific. This nanobody was raised against the Aβ peptide binding to the epitope 17-28 with a measured dissociation constant to the monomer of 13 nM. The CSF samples were pre-incubated with 150 nM Nb3 for 15 min prior to the experiment. For recombinant Aβ42 oligomers approximately 18 nM was needed to half Ca^{2+} influx [92]. The same Ca^{2+} reducing effect with synthetic Aβ42 aggregates was found in the cell assay [260].

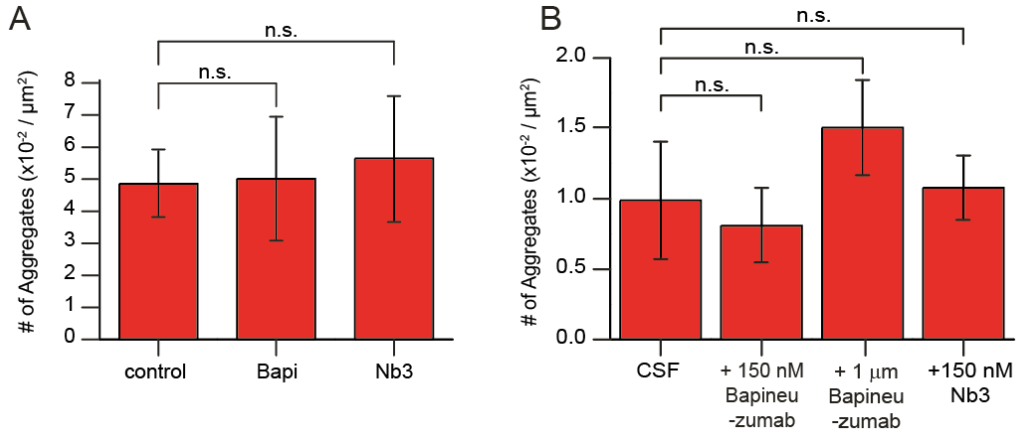

Figure 26 Assessing the structural changes of the ThT-active aggregates with SAVE upon addition of bapineuzumab and Nb3 on synthetic Aβ42 and AD CSF. An aggregated solution of 1 µM total Aβ42 monomer concentration was incubated with 150 nM of each antibody for 15 min and aggregates were counted as described previously. Each bar represents the mean of 3 slides with 27 field of views overall imaging a 3 x 106 µm2 area. Error bars represent the standard error of the mean of all 27 field of views (B) The effect of the antibodies on the number of ThT positive aggregates in human CSF. The mean of 4 samples with 27 field of views each with the error bars representing the standard error of the mean of all samples. Full statistical details are in Table 6.

After testing the effects of clusterin and Nb3 I went on to test the efficacy of bapineuzumab. The bivalent humanised antibody that was tested to bind soluble Aβ monomer and oligomers at the N-terminus [264]. However, the phase 3 trials did not show any clinical outcome in AD patients [255,256,265]. There are many possible explanations why the trials might have failed. One of the most agreed ones are, that the passive immunisation might have occurred to late in the disease, that the effective doses were to low and that the disease relevant species might not have been targeted adequately. Especially the two last points are the ones that we will investigate further with our proposed methods.

150 nM bapineuzumab caused a relative decrease of 70% in Ca^{2+} influx and 1 μM reduced it completely with recombinant Aβ oligomers. It was also effective in preventing the Ca^{2+} influx in the cell assay. The concentration of bapineuzumab did not detectably alter the number of ThT-active species with recombinant Aβ oligomers (Figure 26 A) or with AD CSF (Figure 26 B). This indicates no significant change in the number of β-sheet containing species within the timescale of our experiments.

When AD CSF samples instead of recombinant Aβ oligomers were used with an antibody concentration of 150 nM the Ca^{2+} influx was decreased insignificantly by ~12% for both AD and HC (Table 4). An increase of the bapineuzumab concentration to 1 μM caused a relative decrease of ~75% in the vesicle assay (Table 4), but no significant reduction in the cell assay at either antibody concentration. Bapineuzumabs lack of reduction, even at high concentrations, could be explained by different affinities or interactions between the cell membrane and the oligomers in contrast to the POPC vesicle. The results show that higher bapineuzumab concentrations are needed to reduce the extent of Ca^{2+} influx caused by human CSF compared to synthetic Aβ42 oligomers in buffer solution.

In addition to the SAVE technique, I also tested bapineuzumab and Nb3 in a smFRET experiment to see if the antibodies potentially change features of the aggregates that are undetected with SAVE. According to the previous tests I aggregated dual-labelled co-aggregates and incubated them for 24 h and 48 h with a humanised IgG, bapineuzumab, Nb3 and no antibody and measured before addition and at both timepoints. The first aspect tested with this method was, whether the fraction of the aggregates goes down over time as a function of the presence of the antibodies. The smFRET technique is more sensitive towards small aggregates and

hence might show differences in the non ThT active populations. Despite the increased sensitivity no significant difference was in the number of aggregates due to the presence of the antibodies (Figure 27 B). The consistent number of donors shows that no effect is masked by depletion of aggregates out of the mixture (Figure 27 A). This was further confirmed with the fraction of oligomers not changing either, meaning the equilibrium is not shifted (Figure 27 C). Again, if we normalise the aggregates and look at the fold reduction between the time intervals there is no significant reduction (Figure 27 D). Finally, there is no difference in the aggregate reduction comparing Nb3 and bapineuzumab to IgG.

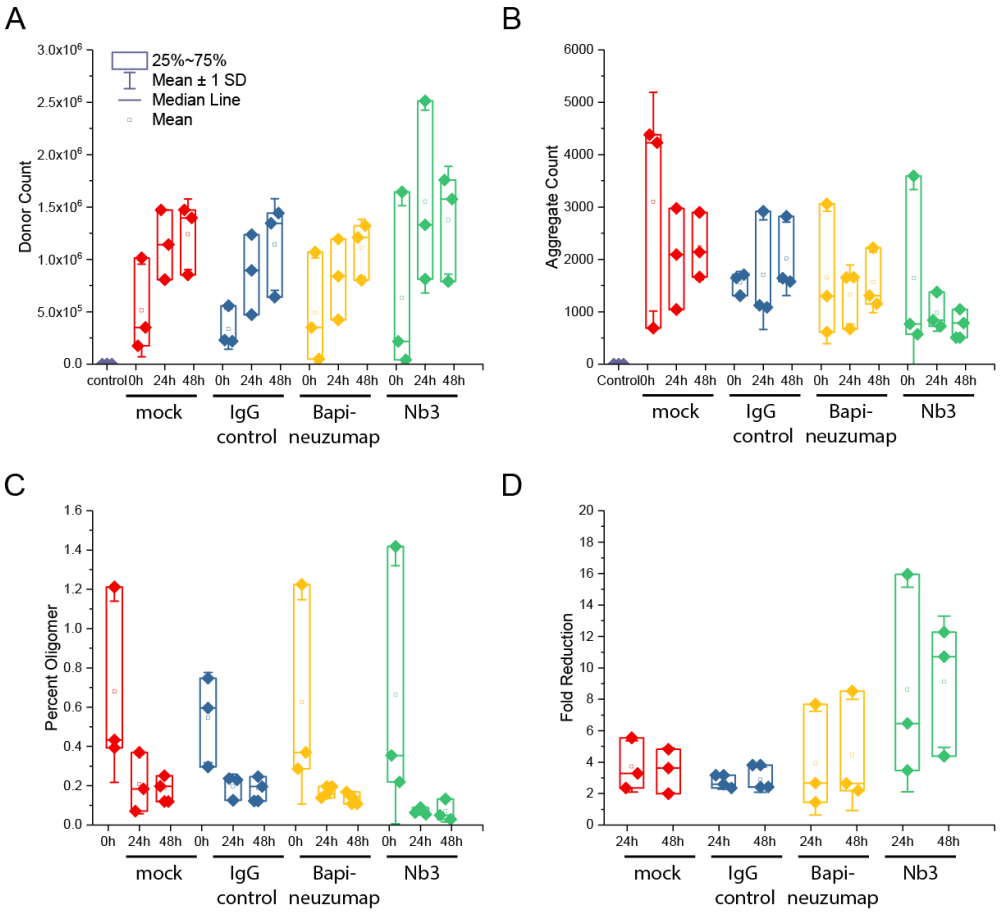

Figure 27 The effect of various antibodies on dual-labelled co-aggregates tested with smFRET at 24 h and 48 h after addition is shown. As indicated in (A) all three independent repeats are shown with the 25 and 75 percentiles as box, the median line and mean as small squares and the standard deviation of the mean as error. (A) The effect of the antibodies on the donor count is shown and to show that no donor depletion is causing any effects. In red (mock) only buffer is added to the aggregates; in blue the addition of a humanised anti IgG control antibody is plotted; in yellow bapineuzumab and in green Nb3. (B) The aggregate count of all FRET positive oligomers is plotted. (C) The percentage of oligomers as a function of FRET positive aggregates over the number of donor events is shown. (D) The fold reduction of FRET active aggregates over the first and second 24 h interval is shown. The reduction in aggregates is not significant, neither within the individual samples, nor compared to the IgG control.

Even though I am not detecting changes in the number of aggregates with the smFRET method I can still get insight into the FRET efficiencies within the aggregates and hence look for structural changes. To analyse the structural changes upon addition of the antibodies I used the FRET efficiencies measured and compared them between the various incubation periods and antibodies.

The FRET histograms of one repeat is plotted as an example for the underlying data for the subsequent fitting (Figure 28). All histograms were fitted, with all r^2 below 0.9 and are plotted (Figure 29). There is no significant change in the FRET efficiency and hence the structure of the aggregates under these conditions.

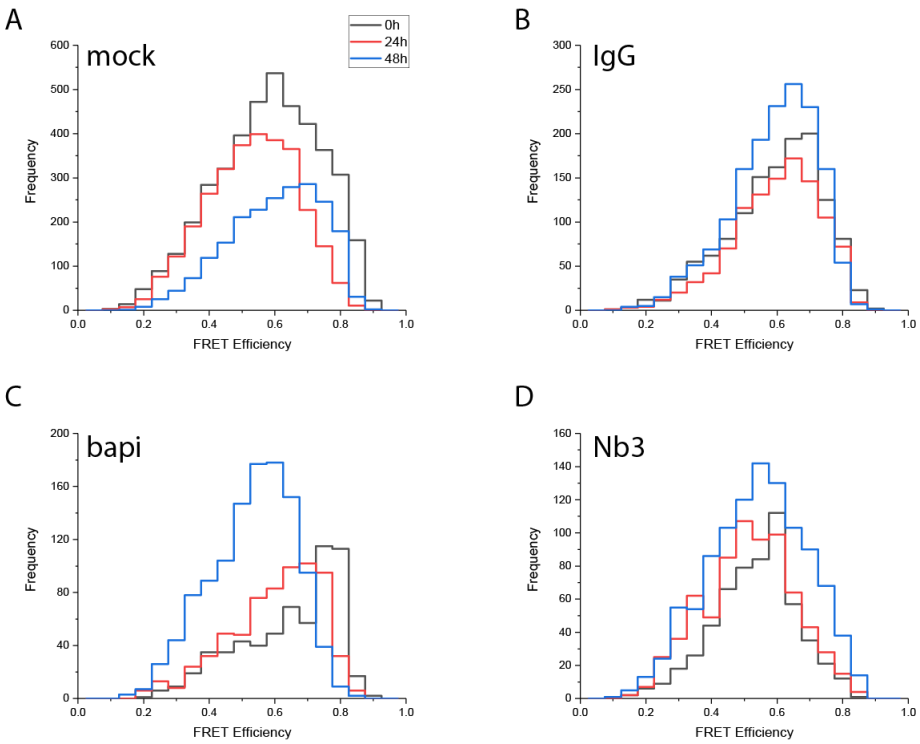

Figure 28 Example histograms of the FRET efficiency change over time for the various antibodies. The FRET efficiencies are shown as a function of time: before incubation with antibody (grey), after 24h (red) and after 48h (blue) with (A) the mock buffer only, (B) 1 µM of an unspecific human backbone anti-IgG antibody, (C) 1 µM bapineuzumab and (D) 1 µM Nb3.

I can therefore conclude, that any beneficial effects are due to binding to the aggregates and subsequently masking any potential harmful surfaces of the aggregates.

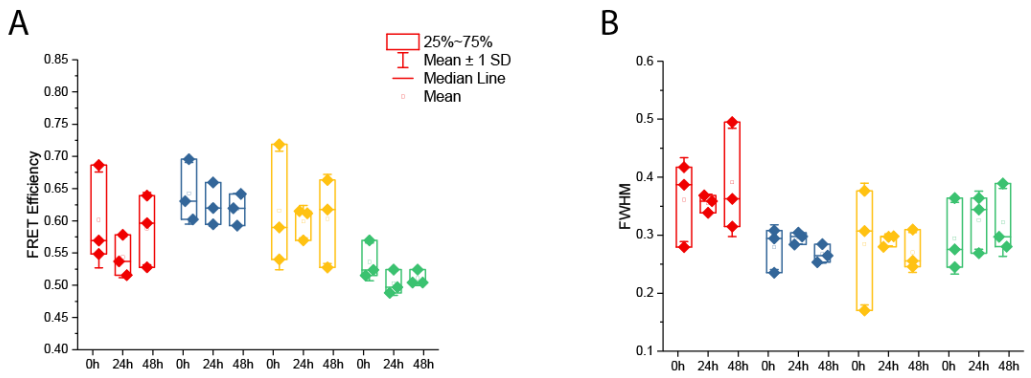

Figure 29 The mean FRET efficiencies as fitted to the histograms. (A) The result of the gaussian fitting of the histograms with all three repeats shown as data-points (B) FWHM to show the homogeneity of the population.

Possible explanations for the reduced effectiveness of the inhibition of the Ca^{2+} influx caused by human CSF include (1) reduction in the effectiveness of binding of the antibody to the oligomer due to molecular crowding and non-specific binding; (2) morphological changes between Aβ oligomer in CSF to the synthetic ones used in the *in vitro* case; (3) post-translational modification could be present in Aβ oligomers in the CSF, rendering them inaccessible or not recognisable to the antibody while still causing Ca^{2+} influx. Any combination of these effects could cause the observed effects and hence bapineuzumab is less effective in human CSF.

Finally, I used an IP setup with Nb3 and BSA as control attached to magnetic beads to probe for the specificity of the Ca^{2+} influx effect. The depletion of Aβ42 due to the interaction with Nb3 should lead to a decrease in the number of ThT-active species and to a drop in the Ca^{2+} influx in our vesicle assay. This assumes the epitope is readily accessible and the Nb3 binding surface is available after binding to the oligomers. The magnetic beads with the streptavidin-biotin linker should allow for sufficient accessibility of the Nb3 epitope. After an incubation time equivalent to the previous experiments I removed the beads out of the CSF solution. The resulting SAVE and vesicle assay measurements are shown (Figure 30)

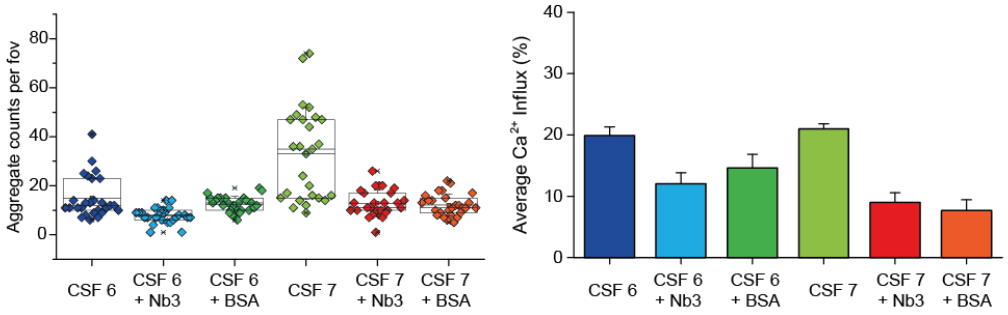

Figure 30 IP pull-down test to test the specific depletion of aggregates with the Aβ42 specific Nb3 and BSA as control immobilised on Dynabeads. (A) SAVE imaging of two CSF samples (CSF 6, CSF 7) before the IP procedure after incubation with Nb3 and BSA coated beads respectively. The datapoints show the aggregate counts per field of view for 27 imaged. The box shows the 25 and 75% percentile, the mean line and the error bar is the standard deviation. (B) The Ca^{2+} influx of the same samples was measured with the vesicle assay showing the mean Ca^{2+} influx with standard error as error bars.

With the SAVE imaging I observe a slight drop in the number of aggregates in the CSF after the IP step. This is consistent with a drop of toxicity in the vesicle assay. However, the difference between the Nb3 coated and BSA coated beads is not significant highlighting a common problem with these experiments. I believe that the observation might be a result of the unspecific binding of the aggregates to the bead, due to the hydrophobic nature of the aggregates. That means the aggregates are depleted out of solution by either the bead surface or hydrophobic interaction with BSA. I can confirm a decrease in toxicity due to the incubation suggesting it is indeed the Aβ42 aggregates. The reduction by adding antibodies in solution shows that they are Aβ42 containing.

Table 4 Full statistical details of the single vesicle assay presented in the indicated figures above.

Single Vesicle Assay				
Figure	**Sample**	**Number of vesicles**	**Number of CSF samples**	**p Value**
Figure 22 B	AD	4906	5	0.44
	HC	4602	5	

Table 5 Full statistical details of the cell assay presented in the indicated figures above

Cell Assay				
Figure	**Sample**	**Areas per sample**	**Number of CSF samples**	**p Value**
B	AD	33	6	0.30
	HC	65	9	

Table 6 Full statistical details of the single aggregate imaging presented in the indicated figures above

Single Aggregate Imaging				
Figure	**Sample**	**Areas per sample**	**Number of CSF samples**	**p Value**
Figure 23 B	AD	27	19	0.49
	HC	27	12	
Figure 26 A	Aβ42	27	N/A	0.70
	Aβ42 + BAPI	27	N/A	
Figure 26 A	Aβ42	27	N/A	0.07
	Aβ42 + Nb3	27	N/A	
Figure 26 B	CSF	27	4	0.62
	CSF + 150 nM BAPI	27	4	
Figure 26 B	CSF	27	4	0.28
	CSF + 1000 nM BAPI	27	4	
Figure 26 B	CSF	27	4	0.73
	CSF + 150 nM Nb3	27	4	

4.3 Outlook and Discussion on methods using CSF

I demonstrated that above assays, both the SAVE and the vesicle assay, can be useful to understand the molecular mechanisms of PD and AD. The SAVE technique has some obvious limitations, most importantly it only binds to beta-sheet structures. This is obviously specific for amyloid aggregates, but it is not specific to subtypes of aggregates made from different monomers such as Aβ42 or αS. This also means we cannot measure non-ß-sheet containing aggregates which might be more neurotoxic. SAVE can however still complement other techniques. Especially in the case of PD there seems to be a better relation between the number of aggregates in the CSF and with disease progression. It is imaginable that multiplexing with e.g. various extrinsically fluorescent dyes with specific binding sites or a combination of ThT or ThT-like dyes and antibodies could help expand the information content we could gain from imaging aggregates in CSF.

Similarly, techniques that use other targeting molecules such as clusterin and explore competition or other interactions of amyloid aggregates on single molecule level could help in deciphering the molecular mechanisms of the neurotoxicity. This has been briefly explored and has potential to be developed into a high-throughput method. This would ideally be paired with a second parameter as clusterin, as a chaperone, is not sequence specific for e.g. Aβ42 or αS.

The presented research lets me conclude that SAVE can be a useful tool in studying PD and AD alike. I have optimised the conditions for SAVE imaging showing that can be extended to other dyes such as DCVJ and DiThT which has a higher affinity for the aS aggregates. All this provides useful knowledge to select adequate dyes and concentrations in SAVE imaging. However, SAVE was not readily transferable to AD in the sense that the difference seen in PD patients was not observed in AD. Despite this limitation the technique is still useful in understanding aggregates in CSF. It allows us to specifically and compare effects of other proteins towards the aggregates in CSF. Crucially the exact composition and interaction of these amyloid aggregates, be it in PD or AD, might be different from the *in vitro* aggregates. This is where ongoing efforts towards IP procedures coupled with mass spectrometry come into play. The use of immobilised bait structures using the same binding properties as ThT and DiThT should allow to decipher these structures. The specificity to the ß-sheet structure motif and not a sequence specific motif could help understand

the composition of the ThT active aggregates detected in SAVE and potentially improve the method.

Optical methods have been developed too, to further improve the SAVE based toolbox. Namely the optical structural analysis of individual α-Synuclein oligomers developed by Varela and colleagues [266]. This method utilises the polarisation direction of the light to decipher the structural properties if the binding entity. Beta-sheet structures are highly ordered a in consequence their binding sites for ThT too. Oligomers in contrast are amorphous and hence have not the same properties. This allows for an optical distinction of the emission light via the polarisation of the emitted fluorescence. This can then be applied to both *in vitro* and *in situ* samples such as PD CSF.

With the right assays we might not be able to check for distinct biomarkers immediately, but we might be able to show the effectiveness of antibodies to various targets. This in turn helps us understand antibody binding better leading to a positive feedback loop. The above presented techniques are, as suggested, very useful in testing potential antibodies directly in human CSF too. Especially the vesicle assay can be used as a high-throughput method to readily assess capabilities of antibodies. It can also be used for the direct comparison of such as it is possible to generate binding affinity values for oligomers.

With the mechanisms by which amyloid aggregates cause toxic effects and neuronal cell death still under investigation, above methods are even more powerful. Especially in the light of the proposed route of the permeabilisation of membranes, leading to altered calcium homeostasis and ultimately cell death. Our experiments explore this particular branch of proposed mechanisms and shows that that human CSF can induce Ca^{2+} influx in our assays using both single vesicles and astrocytes. This can be counteracted by the addition of clusterin, Nb3 and bapineuzumab. It is important to stress that this effect was much less in AD CSF than in the synthetic counterpart with Aβ42 oligomers in buffer. This suggests the Ca^{2+} influx causing oligomers differ in their structure and composition making and that Nb3, bapineuzumab and clusterin interact with other components in the CSF making them less available. This might explain why bapineuzumab is only effective in reducing the Ca^{2+} influx in CSF at 100-fold higher concentrations than used in the clinical trial [267] If the effects that we observe in CSF reflect those within the brain, this suggests that

high concentrations of the antibody (or perhaps higher affinity and more selective antibodies) are required to sequester fully the potentially toxic aggregates.

5 Size dependent Structure and Effects of Aβ42

5.1 Introduction

One of the most challenging aspects of studying Aβ42 *in vitro* is the heterogeneity of the species throughout the aggregation. The aggregates are also very low in concentration in comparison to the monomer concentration. These issues arise from the kinetics of aggregate formation in solution.

The aggregation of Aβ42 happens at comparable fast reaction speeds when the critical aggregation concentration is reached. Most aggregation reactions are done at concentrations between 0.5- 10 μM monomer concentration in order to observe a lag phase. At these concentrations the lag phase is in the regime of tens of minutes to hours. However, this lag phase decreases as the monomer concentration increases. This short time window makes the study of very early aggregates very challenging.

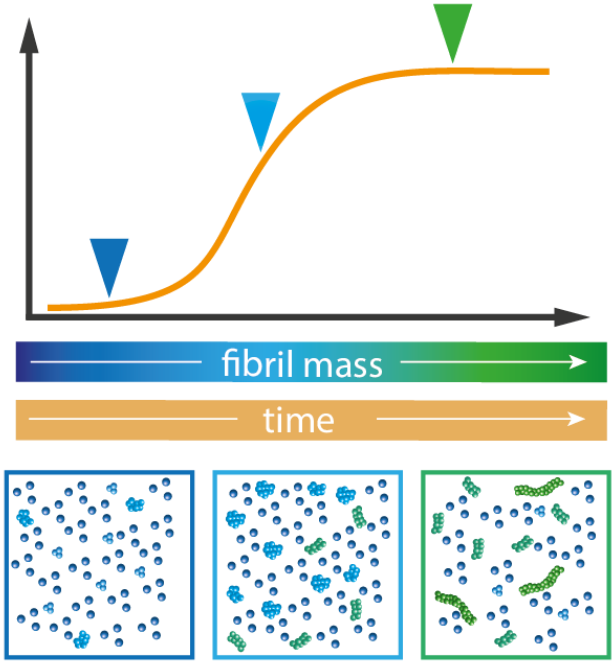

Figure 31 Kinetic scheme of a classic aggregation reaction. The fibril mass increases as a function of time. The arrows indicate possible situations at the different time points. Even though the fibril mass increases on average, smaller protofilaments or oligomers can be present at later times.

Furthermore, the kinetics of the aggregation of Aβ42 are difficult to keep consistent and reproducible. This results from problems in the purification of pure monomer solutions and from impurities in preparations of solid-phase synthesised Aβ42. In addition, most preparative steps require time frames that are as long as or

longer than the lag-phase. This results in aggregation during these steps, to varying degrees, and also often generates irregular lag-phases. However, by generating MAβ42 (Methionine- Aβ42) and Aβ42 recombinantly in *E. coli* the issues with the reproducibility of the kinetics can be overcome [199,268,269]. This enables the kinetics to be modelled to the mathematical models described earlier [132]. It was also shown that recombinant Aβ42 aggregates faster and is more neurotoxic than synthetic Aβ42 [270].

Another challenge in the analysis of protein aggregation with certain fluorescent techniques is the inherent need for a fluorescent dye. Especially the use of covalently attached fluorescent dyes. Due to the high dilutions needed in single molecule experiments, the use of antibodies is not always feasible. Very high K_d values for the binding are required to guarantee the binding at nM to pM concentrations. Covalently attached fluorescent dyes however can potentially alter the aggregation kinetics and can interfere with commonly used techniques, such as ThT curves, to measure the aggregation. This is often caused by fluorescence quenching effects. Thus, if we want to benefit from the detection advantages of the fluorescently labelled proteins, but still compare labelled and unlabelled protein, we need to find a way to bypass kinetic preparations of the aggregates. This would be possible by using a purification technique that separates species based on structural properties.

In this chapter I will show how I used gradient ultracentrifugation to sample a wide range of amyloid aggregates allowing me to directly compare labelled and unlabelled protein. Furthermore, by using this technique I prepared aggregates of multiple sizes within a single experiment under the same preparation conditions. I then directly compared aggregates in respect to their structural properties and their effects on biological models

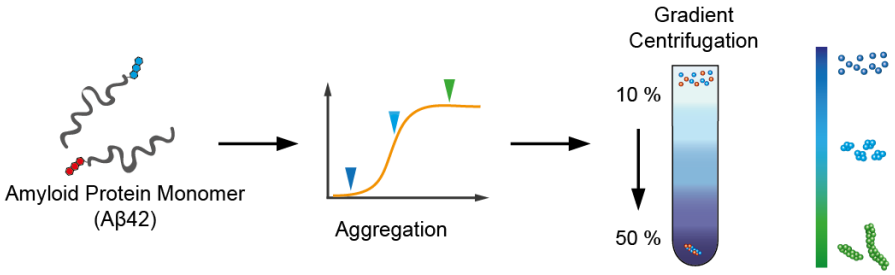

Figure 32 Schematic representation of the ultracentrifugation workflow. Aβ42 monomers, either synthetic labelled co-aggregates or recombinant MAβ42, are aggregated. Usually a combination of time points is combined to sample all species (shown as coloured triangles on the graph) and then loaded onto a sucrose step-gradient. The gradient is divided into five fractions and subsequently measured.

Gradient ultracentrifugation is a commonly used preparative technique for large molecular and macromolecular proteins such as organelles, molecular machines and others. The underlying principle uses the varying hydrodynamic radius (which I will refer to as size of the aggregates from here on) coupled with a gradient increasing in density to differentiate molecules of different sizes. As the centrifugal force is applied the different lengths/sizes migrate with different velocities according to their sedimentation coefficient. The sedimentation coefficient is determined by both the density of the aggregates and their physical shape. That means the relation between mass and sedimentation coefficient is only linear for equally shaped objects. In the case where amorphous oligomers and small fibrils are present simultaneously different shapes and different masses could provide similar sedimentation coefficients. However, we will be able to distinguish these situations with the single molecule methods if they arise.

Analytical ultracentrifugation has been used before to study properties of amyloid aggregates of Aβ42 before [271]. These methods were the starting point for the purification of the Aβ42 aggregates. Gradient centrifugation has also been used to study Aβ40 aggregates and AD brain extracts [272,273]. However, gradient density centrifugation has not been used as a tool to compare amyloid aggregates on a single aggregate level structurally and biologically. As discussed, current research suggests that the small soluble oligomeric forms of aggregates are the most neurotoxic [86,274]. Hence oligomers would be an attractive target for treatment and/or prevention. However, as discussed previously, these forms are challenging to study *in vitro*. Gradient ultracentrifugation is one method that allows to access wide range of aggregate sizes in a single experiment [273,275,276]. Thus, the isolated sizes will be unchanged and consistent, independent of the kinetics of the aggregation.

In addition, the wider array of isolated species will allow us to observe trends rather than differences between two extremes. We can also avoid the pitfalls that occur in other size separation methods, such as size-exclusion chromatography (SEC), which are problematic for fast aggregating proteins. For example, in SEC a high local concentration of protein may occur on the column which could facilitate aggregation resulting in the loss of the small oligomers.

However, it is important to note that this experiment cannot take into account possible polymorphs within the same aggregate size. These have been implicated in amyloid fibrils but it is unclear what role they play for oligomers *in vivo* [115,277].

The role of microglia and neuroinflammation in AD

Neuroinflammation has also been suggested to play a role in the development of AD [278]. In particular, small soluble oligomers have been linked to neurotoxicity. This has led to studies of their structure, molecular interactions and biological mechanisms. As described in chapter 1.3 multiple variants of small soluble oligomers have been purified, structurally characterised and tested for their biological mechanism. However, to this day no atomic or molecular structure of non-β sheet containing Aβ42 oligomer exists. Furthermore, the molecular mechanism that leads from a presence of monomers to oligomers to neurotoxicity, and ultimately the specific clinical effects of AD, is also unknown. That does not mean, however, that the neurotoxic link has not been confirmed [16].

The role of neuroinflammation in AD is a concept that increasingly gained traction more recently. The findings that microglia respond to injury paired with the observation of increased microglial activation in AD patients have lead to the hypothesis that the microglia cells are involved in the disease mechanism [279]. Microglia cells themselves are abundant in the brain and are linked to maintenance and plasticity of neuronal circuits and contribute to the protection and remodelling of synapses [278,280]. In the case of AD, microglia have been found to bind Aβ via cell surface receptors (SCARA1, CD36, CD14, α6β1 integrin, CD47) and Toll-like receptors (e.g. TLR2, TLR4, TLR6, and TLR9) [281-284]. This is thought to be an important part of the inflammatory reaction in AD. CD36, TLR4 and TLR6 result in the pro-inflammatory activation of microglia, while genetic deletion of these receptors reduces Aβ-induced cytokine production [283,285,286]

The link between microglial activity and AD was backed up by the findings that pro-inflammatory cytokine levels in the AD brain such as interleukin (IL)-1β, TNFα and IL-6 were increased and *in vitro* studies showed that these pro-inflammatory cytokines led to neuronal toxicity and death [287]. TNFα in particular was shown to be elevated in AD serum, CSF, cortex and glial cell cultures after exposure to Aβ [278]. TNF-α stimulates NF-κB, a transcription factor for pro-inflammatory factors such as complement and cyclooxygenase (COX) [288,289], as well as survival factors such as

calbindin, manganese-superoxide dismutase, and Bcl-2 [287]. The pathophysiological role for TNFα in AD however is not entirely clear. It has been both reported to kill human cortical neurons [290] but also to be trophic to rat hippocampal neurons [291]. It was also found to protect against glutamate, free radicals and Aβ toxicity in primary neuron cultures [292]. More specifically in AD, the risk for conversion from mild cognitive impairment to dementia is increased in patients with elevated concentrations of TNFα and lower concentrations of the anti-inflammatory TGF-β in the CSF [293]. Protofilament of Aβ42 in particular have been shown to stimulate microglia more robustly than mature fibrils or oligomers while leading to increased TNFα levels [294]. Other contributing factors to neuroinflammation such as complement, chemokines, caspases and others are reviewed extensively by Heneka and colleagues [278].

One system I used is a simplified cell membrane model and a technique to ultrasensitively measure oligomers through calcium influx into POPC vesicles. The other model is the measurement of TNFα production in mouse microglia cells in response to the aggregates

To sum up, in the following chapter I will show how I addressed the problem of studying aggregation independent of kinetic effects. I will furthermore show how I examined if intermediate states of aggregation induce calcium influx and an inflammatory response and how this could potentially be applied to more complex biological questions. I will show that Aβ42 oligomers induced the highest Ca^{2+} influx in the single vesicle assay while protofilaments led to the biggest inflammatory response in mouse microglia cells. The single molecule measurements gave me a measurement of the relative aggregate concentration, I hence can be confident that the effects are proportional to the amount of aggregates present.

5.2 Results

5.2.1 Structural Characterisation

It is essential to have structural information on protein aggregates to make insightful conclusions on molecular mechanisms and biological effects. In the following I will show how the size of the aggregates affects the toxicity of Aβ42 aggregates. This will be a two-step process: (1) I used gradient ultracentrifugation to prepare sized aggregates which I characterised with single molecule methods to, (2) test the influence of size on the permeability of artificial membranes and on the inflammatory response.

I will firstly describe how I developed a protocol for the sucrose ultracentrifugation method with the Aβ42 aggregates. This focuses particularly on the aspects of the structural characterisation via fluorescence and other methods. I characterised the kinetics of the aggregation itself with TIRF microscopy. This is important to help with the selection of aggregation timepoints to later on use as input for the gradient centrifugation, as I wanted to assure that the majority of possible aggregation states is present as a starting point for the preparation. Furthermore, this gives an indication and reference on where the sized aggregates would occur within the aggregation reaction.

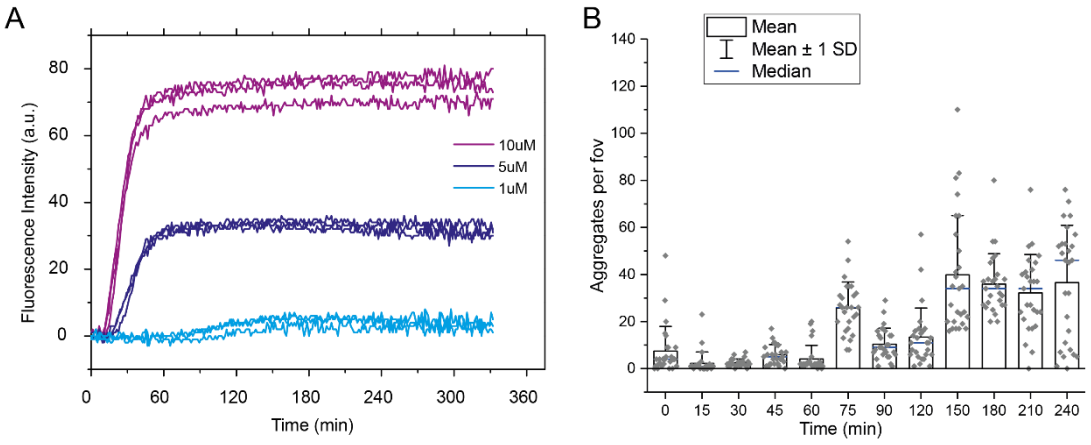

Figure 33 (A) Plate reader aggregation with ThT fluorescence as measure of the fibril mass of unlabelled Aβ42. The fluorescence traces of three parallel technical repeats are shown (B) Dual labelled co-aggregation of Aβ42 in TIRF mode. The number of detected aggregates is shown as a function of time with the bars representing the mean with the standard deviation as error and the blue line the median. Each dot represents one field of view. There is a clear increase in the number of detected spots after about 60 minutes. This measurement was done at constant dilution of the sample. The increase in aggregates corresponds well with ThT measurements for recombinant proteins but the lag phase appears to be longer. We also have to take into consideration, that this was optimised for the later time points in respect to dilution, with the dilution kept consistent throughout. I will discuss this in more detail in the text.

I measured an aggregation of a 2 μM dual-labelled co-aggregation on the TIRF microscope to establish a starting point for the subsequent preparation. As shown in (Figure 33) the number of aggregates clearly increases after about 60 minutes. However, the TIRF method in this case was optimised for higher aggregate levels which means the threshold in terms of detection is skewed towards the bigger, brighter aggregates. Also, the number of the aggregates is not the ideal metric for an increase in size and/or aggregate mass, as in later stages the number of aggregates decreases with more and more monomers bound in large fibrils. Rather representative images (Figure 34 A) and histograms of the intensities (Figure 34 B) are a much better indication for an increase in size and/or aggregate mass.

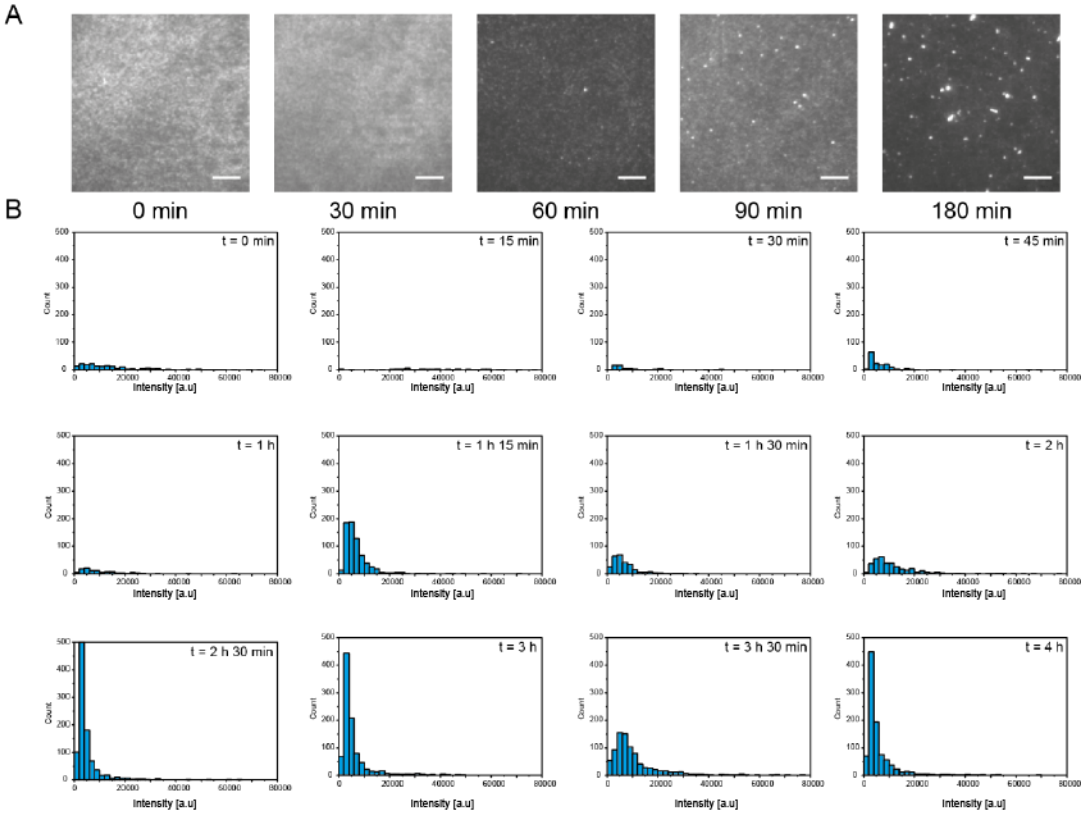

Figure 34 (A) Representative TIRF FRET images of various time-points of the aggregation are shown. The scale bar is 10 μm. (B) Intensity histograms of the dual-labelled co-aggregation of Aβ42. The histograms for all time points are shown as marked. Each histogram is the sum of 27 field of views measured in three technical repeats of a single aggregation.

The aggregation was also monitored with ThT in a plate reader for the unlabelled aggregation which I used later in the vesicle assay and for AFM experiments. I show a ThT aggregation of synthetic Aβ42 as used for the AFM and similar to the one used for the vesicle assay experiments (Figure 33 A). In the vesicle assay experiments these ThT reference measurements were done with recombinantly expressed MAβ42 (not shown). The purification and preparation for above Aβ42 was different to the one

used in the vesicle assay, this leads to a slightly shorter lag-phase. This is not a problem as we have the centrifugation step to correct for any variability.

The fluorescence labels for the co-aggregates interfere with ThT measurements, hence I could not measure the equivalent ThT curve for the dual-labelled aggregates. This does not pose a problem, as the smTIRF data is sufficient to select timepoints with the required distribution of sizes. I started testing the gradient with a mid to late aggregation timepoint at about 1 h 30 min, to include fibrillar species in the mix. For experiments with the vesicle assay, I started 3 aggregations in intervals starting 40 min 1 h 20 min and 3 h before mixing and centrifugation. Both a single timepoint and mixed timepoint are viable as the analysis with single molecule methods shows the exact distribution of species and number of aggregates needed for further analysis. Furthermore, both the single timepoint and the mixed timepoint showed an abundance of species of all sizes with somewhat different distributions, which is accounted for by the SM measurements.

Aggregate Structures as measured with dual-labelled co-aggregates

I first used TIRF microscopy to observe the aggregates in FRET-mode using the dual-labelled co-aggregates. This gives very fast and accurate insight into the sizes and morphologies occurring as results of the preparation.

The high-resolution TIRF microscopy allows me to measure on a length scale from the diffraction limit (~200nm) up to a few hundreds of μm in length in a single field of view. This has a few advantages: (1) we are not limited by large sizes in fractions that contain large fibrils in contrast to a confocal volume; (2) we can immediately see morphological differences through the images we record, mainly fibril shapes and structures; (3) the measurement is high throughput due to the comparably short measuring intervals (~10-15 mins per sample in triplicates). However, one notable limitation is the highest resolution we can achieve, as we need to measure structures at sub 200nm length-scales for small aggregates. TIRF microscopy is also a surface-based technique which might lead to preferential binding of some species to the coated surface or alter properties of the aggregates upon binding. The latter seems unlikely but cannot be fully excluded. I then complemented the TIRF data by measuring unlabelled protein with extrinsically fluorescent dyes such as ThT and pFTAA [77,295].

The steps described below were directly used to assess the quality of the gradient centrifugation in its ability to cross-sectionally separate aggregates. I used sucrose as the gradient reagent as it did not have any measurable impact on the aggregates. Although sucrose has been found to impact the aggregation reaction in some cases of amyloid aggregation [296], this was not a concern for my experiment as the aggregation occurred in absence of sucrose. Aggregation that occurs during the centrifugation does not impact the results as the centrifugal force is constantly present throughout. To avoid any further aggregation during the time of measurements, the reactions were kept on ice immediately after the centrifugation and not used longer than a day, which was sufficient for all tests and assays. The sucrose used as gradient reagent was prepared matching the aggregation buffers for labelled and unlabelled protein respectively which should not affect the aggregates adversely. I also explored the possibility to cross-link the aggregates using GraFix [297]. The results were inconsistent and for the selected structural methods not strictly necessary. This could be a pathway to molecular structure determination though, taking into account the limitations of crosslinking proteins.

The TIRF-monitored aggregation reaction guided the selection of suitable timepoints for subsequent experiments with the gradient ultracentrifugation. Using the TIRF microscopy with labelled co-aggregates I find that the mean size, as approximated by the intensity, increases. We can justify this approximation by the fact that all monomers contain a fluorescent dye and hence, the increase in intensity correlates with the increase in aggregate size. This is especially useful for sub-diffraction sized aggregates as, even though they appear to have the same diameter, their intensity will still differ. I can see morphological different aggregates in the large fractions changing from diffraction limited puncta to elongated fibrils (Figure 35 A). The histograms for fractions are shown in (Figure 35 B).

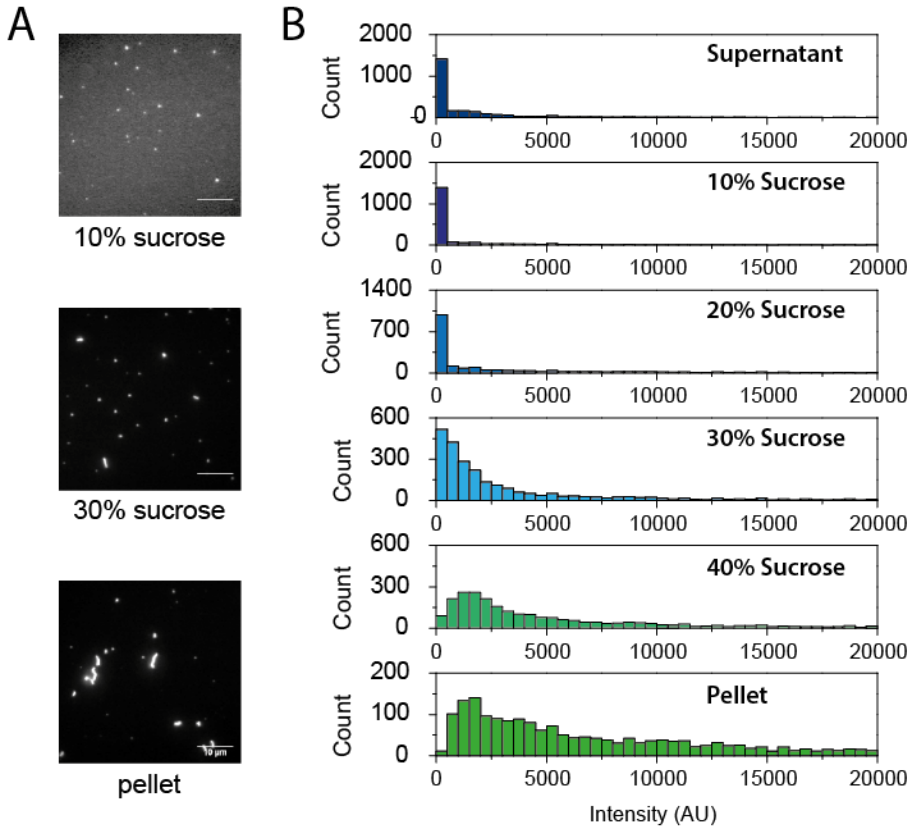

Figure 35 TIRF FRET images and analysis of the gradient centrifugation. (A) Images of three fractions are shown to represent the sizes detected with TIRF microscopy and are representative of the indicated fractions. The scale bar is 10 μm. (B) The FRET histograms of the fractions show a clear shift from a very narrow, dim distribution in the smaller fractions to a marked increase in the higher fractions and in the pellet. Each Histogram is the sum of aggregates of 27 field of views measured in three technical repeats of a single gradient ultracentrifugation preparation.

In the smFRET method I used co-aggregates of 1:1 molar ratios of FRET-donor and FRET-acceptor labelled Aβ42 monomers. These monomers have been HPLC purified previously to avoid possible contamination products. There have been studies that suggest low percentage racemisation in some amino acids during solid phase synthesis which cannot be separated [269]. However, with no N-terminally, fully labelled

recombinantly expressed Aβ42 available, this is for now the best approach to generate fluorescently labelled Aβ42 aggregates. Futhermore, these aggregates have been shown to be morphologically similar to unlabelled aggregates [298].

The smFRET system allowed me to measure the relative aggregate size and their FRET efficiencies as described previously [56,121,122]. I could furthermore calculate a relative percentage of aggregates as function of monomer population in each individual sample, a number which I used to correct the biological effects we observe.

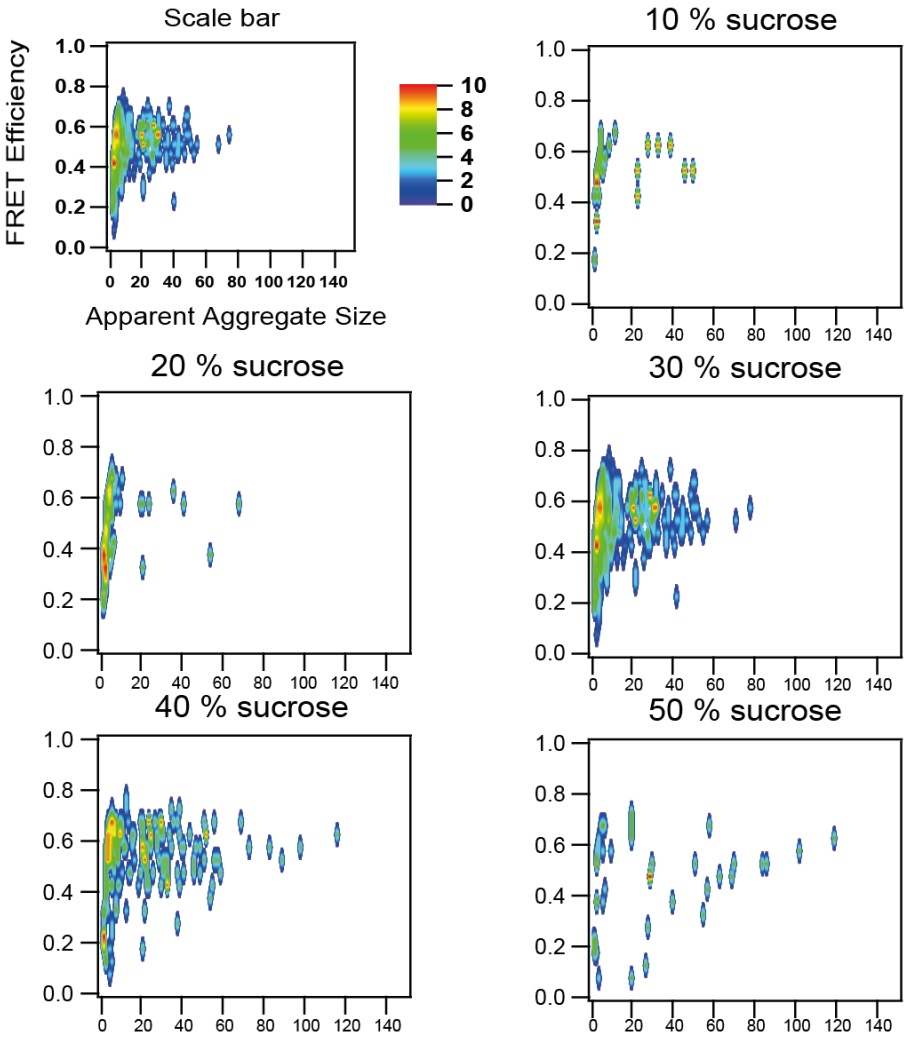

Figure 36 FRET analysis of the dual-labelled co-aggregates as measured with the smFRET. The FRET efficiency is plotted against the apparent oligomer size inferred from the intensity. The aggregates increase in size and the FRET efficiency shifts to higher values. The FRET histograms are representative of the gradient centrifugation fractions and show all aggregates plotted of a single measurement. A single measurement of each fraction contains usually more than 10 000 aggregates, if not the concentrations were adjusted to do so.

The apparent aggregate size plotted against the FRET efficiency (Figure 36) of all measured aggregates shows the shift from bottom left to upper right. This means a

size increase and compaction. As with the TIRF microscopy measurements, the intensity is used as an approximation of the aggregate size. The apparent sizes in lower sized fractions stay consistently low while the increase can be clearly seen moving through the fractions to ultimately the pellet which shows large, high intensity, high FRET aggregate fibrils (Figure 36).

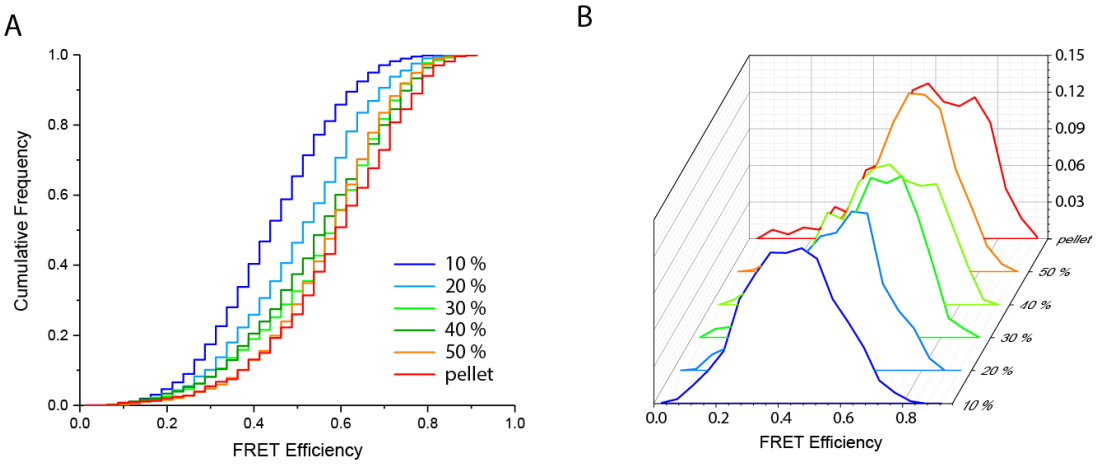

Figure 37 Comparison of the FRET efficiencies as measured in the fractions used for the TNFα measurements. (A) The cumulative frequency histograms show the increase in higher FRET efficiency species with the curve shifting to the right. The Histograms contain all aggregates of the measured fractions (B) shows the normalised FRET efficiency histograms for all fractions. In the 10 % fraction the peak is clearly shifted to the left and then increases over time. These histograms were the basis for fitting two populations (low and high FRET). The fit was done with the 10 % and pellet peak values as fixed values (low: 0.45 and high: 0.62) for the two populations. The resulting fits are shown in Figure 38. This is the result of one representative measurement of one preparation.

The shift to higher FRET efficiency could suggest some form of compaction, but we do not observe distinct structural populations so we cannot definitely determine if there is a structural conversion as seen e.g. for αS oligomers [186,196].

Lastly, the single aggregate measurement allowed me to determine a relative number of aggregates (Table 8). I used this number to normalise the biological assays to a relative aggregate concentration rather than absolute protein concentration.

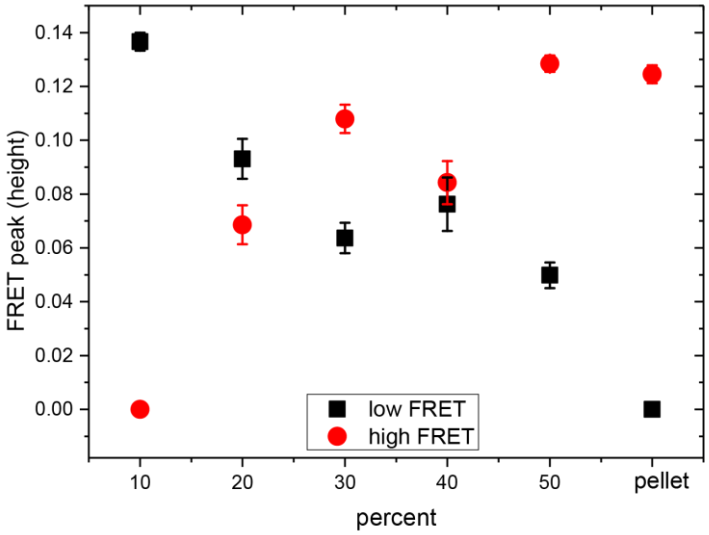

Figure 38 Fitted peak heights of the low (10%) and high (pellet) FRET populations to show the change in the structure more clearly. The fit error is shown as error. As it is apparent from above histograms, the transition is continuous. It needs to be noted that for the fitting the peak of the lowest and highest FRET distributions were used as forced peak positions (0.45 and 0.62 respectively). This can explain the inversion in the 30 percent as the flanks of the peaks are not particularly well suited to fitting.

Sizing aggregates without fluorescent labels

For the single vesicle calcium influx assay it is not possible to use the FRET co-aggregates as spectral overlap would interfere with the measurement of the vesicles. To overcome this problem I used the extrinsically fluorescent dye pFTAA which has similar properties to ThT (in that it binds amyloid structures) [128]. I used pFTAA to determine the relative aggregate concentration difference between the sucrose gradient fractions. This is somewhat limiting in comparison to the FRET methods, as I can only extract the absolute number of pFTAA active aggregates but not the fraction in respect to the total protein. I found that the trend for the intensities of the pFTAA active aggregates is similar to the smFRET. However, the lower fractions (10 % and 20 %) have substantially less aggregates detected overall, which means that the histograms are only sparsely populated (Figure 41 C).

The corresponding TIRF experiments were also carried out with unlabelled protein aggregates using the amyloid reporter dye pFTAA [128](Figure 39). This was to (1) get insights into the binding properties of ThT and pFTAA to oligomeric aggregates and, (2) as preparation for the TIRF and smFRET experiments done in conjunction with the vesicle assay as the used fluorescence excitation and emission wavelengths permitted the use of co-labelled aggregates.

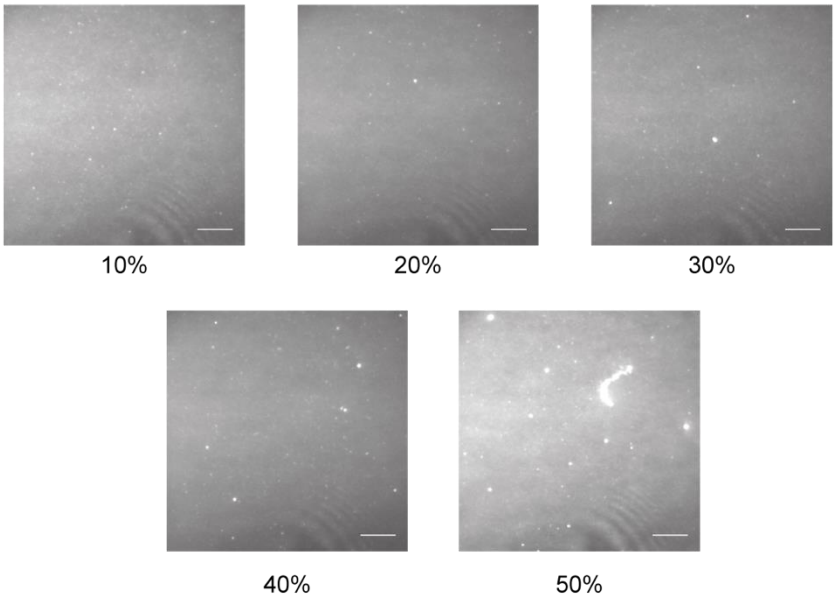

Figure 39 Representative TIRF images recorded with pFTAA of the increasingly larger fractions from 10 % through to 50 %. All images are adjusted for contrast. Especially in the 50% the fibrils are very apparent. The scale bar is 10 μm.

Measuring pFTAA and ThT positive aggregates throughout the isolated sizes show that, below a certain size, no aggregates are detected with the extrinsically fluorescent dyes (Figure 40). I was not able to detect any aggregates in the 10% fraction and only a small number in the 20%. The 20% fraction contains the most oligomers as I will show later. I can readily detect aggregates in the bigger fractions. The decrease of aggregate number in the 50% and pellet can be explained by the presence of large fibrils containing most of the aggregate mass.

In direct comparison pFTAA appears slightly more sensitive and is hence used for the following single molecule confocal experiments. The morphological changes cannot be seen as clearly as with the labelled protein, and the exact relation between fluorescence intensity and aggregate structure is not known. That means the estimate of size is not as accurate. There is still a correlation between fluorescence intensity and increase in size however (Figure 41 C). This correlation is better matched with pFTAA Figure 41B) than with ThT (Figure 41 A). Furthermore, it is entirely possible that the binding properties to the surface for small soluble oligomers is different to the binding properties of mature fibrils and protofibrils. This could lead to a lower representation as aggregate numbers in the lower fractions. The use of confocal measurements in solution using a method similar to the smFRET but with the pFTAA dye instead would avoid this problem.

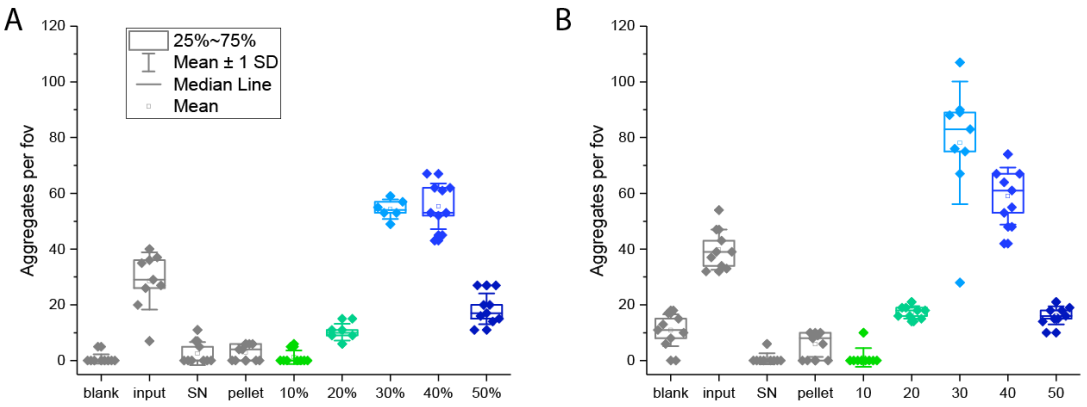

Figure 40 The aggregate count detected with the SAVE technique using (A) ThT and (B) pFTAA. (A) The aggregates per fov of 27 different areas as detected with ThT are shown as a function of the fractions (10-50 %) and the blank, input (before centrifugation), supernatant (SN) and pellet. (B) The same samples as imaged with pFTAA are shown. The overall aggregate count in the input is shown but cannot be compared quantitatively as the dilution due to the subsequent centrifugation has to be taken into account. The results show us however, the extent to which we can detect oligomers with ThT and pFTAA especially in the 20% fraction. We can however readily detect protofilaments and fibrils with both methods. The decrease in numbers in the pellet and the 50% fraction is probably due to less abundant but larger aggregates.

After assessing pFTAA on a TIRF setup I went on to use it in conjunction with the smFRET setup. In this case I can only observe the fluorescence directly from the dye and no FRET as in the following experiments. I could show that the increase in size correlates with an increase in mean intensity (Figure 41) when measured in the smFRET setup. This is consistent with the other measurements and allows us to use it together with the calcium influx assay.

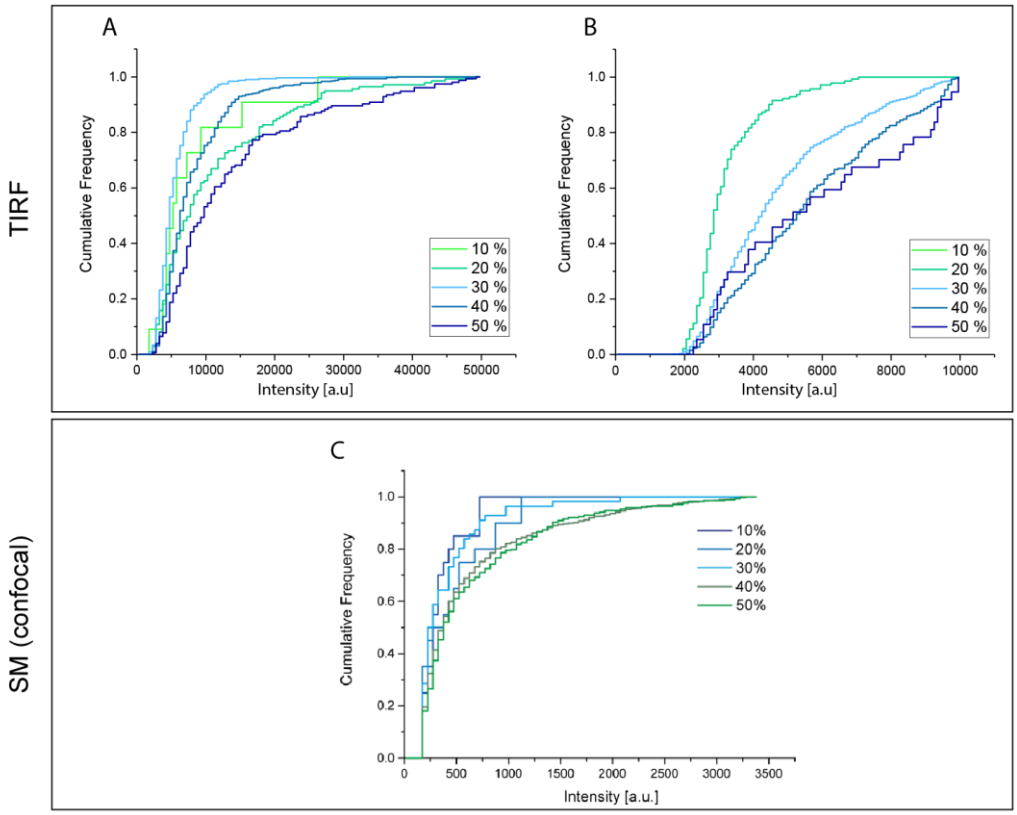

Figure 41 Cumulative Frequency histograms of the sucrose fractions as measured in TIRF with (A) ThT and (B) pFTAA. (A) The increase in intensity towards higher fractions is not as clearly defined especially for the 30% fraction which seems to be fairly low intensity in comparison to the 20% fraction. (B) The increase in intensity towards higher fractions is very apparent. 10% is not displayed as not enough aggregates were detected to display a meaningful histogram. All histograms are the cumulative relative intensities of the aggregates of 3 technical repeats with 9 fov each of one preparation. (C) Cumulative frequency histograms of the pFTAA intensities observed with the fractions used for the single vesicle assay as measured with the confocal SM technque. The lower shape of the curves of the 40 % and 50 % fractions clearly confirms the shift to bigger aggregates while the 10 % fraction shows the smallest ones.

DNA-PAINT and AFM for nanoscopic sizes and structures

The TIRF microscopy methods do not allow us to see any morphology differences below the diffraction limit. In principle it is possible to observe peptide monomers with both TIRF microscopy and the confocal smFRET if they have an attached fluorescence label, but neither of the techniques gives us a clear picture of the sub-diffraction morphology. Thus, I used AFM as a complementary technique to examine the morphology of the sub-diffraction aggregates (Figure 42).

The AFM measurements showed a statistically significant increase in the height of the aggregates. The height can be measured very precisely with the AFM cantilever tip even down to the smallest sized aggregates and can distinguish monomers from aggregates. The height and width characteristics of the lower fraction matched with the properties of soluble oligomers. The 30% fraction which gave the highest increase in TNFα have a diameter and morphology that matches protofibrils with a mean length of ~ 80 nm and a single fibril chain width. The higher percentage fractions are all of fibrillar nature with heights and widths of mature fibrils. That means the AFM measurements confirmed the fluorescence data by showing oligomeric, round shaped aggregates up to the 20% fraction with a transition to more protofilaments, which is hidden in the TIRF below the diffraction limit, and fibrils in increasing size from there onwards. AFM however has its own limitations. This includes attachment to the mica-substrate and the fact that the samples have to be dried which both can introduce artefacts.

Therefore, I attempted to use DNA-PAINT, a technique that allows SR imaging of aggregates, with the sized aggregates. This fluorescence method would have some advantages over AFM, (1) it is a solution-based technique, as mentioned, (2) it could be more easily transferred into fixed and potentially live cells which I will demonstrate in chapter 5.2, (3) in principle it is possible to multiplex with various probes are available. One current limitation for DNA-PAINT technique I use in based on the use of an amyloid specific aptamer. This aptamer was developed for αS and not specifically for Aβ42. We validated that the aptamer binds Aβ42 via Aβ42-657 labelled aggregates co-localising with the super resolved reconstructed DNA-PAINT image. This was done in fixed cells however, as this was a primary interest. This is discussed in more detail in chapter 5.2. The application of DNA-PAINT has some limitations, mainly due to the fact that the surface coating usually used for AB42 imaging, namely PLL,

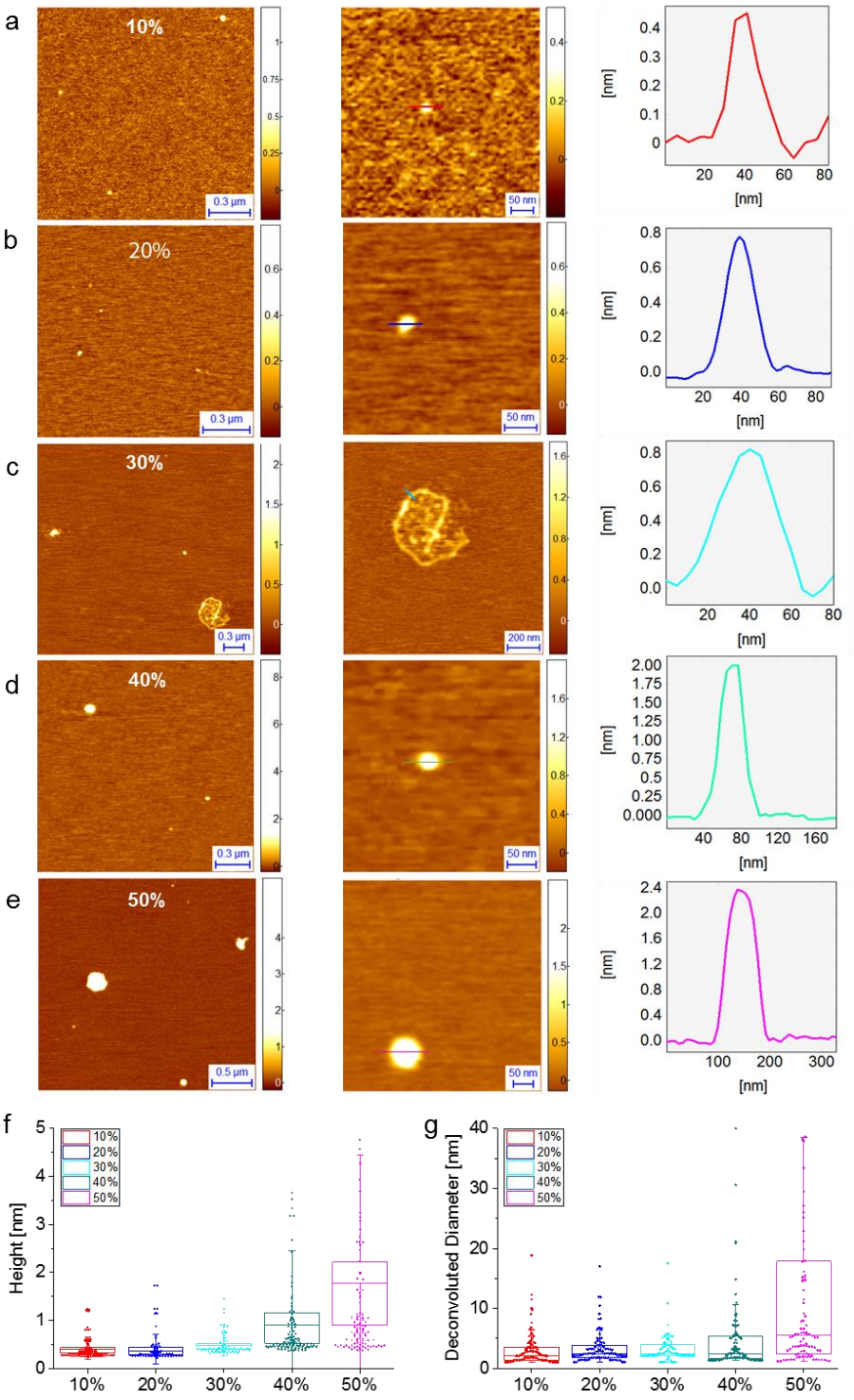

Figure 42 Representative AFM images of the fractionated Aβ42 aggregates. (a)- (e) show a representative overview of the AFM image, a magnified view and a representative cross-section of a single aggregate. The height (f) and the deconvoluted diameter (g) Aβ42 aggregates is shown. The 30% fraction (c) is the only one that shows characteristic cross-sectional width of the protofilaments while 10% (a) and 20% (b) have the cross-sectional width of oligomers and 40% (d) and 50% (e) are fibrils. The images and analysis have been kindly provided by Dr. Simone Ruggeri.

is not compatible with DNA-PAINT. This means I had to use aspartic acid which was used previously with αS. I was not able to detect the fractionated AB42 aggregates with DNA-PAINT. This could have two explanations. The Aptamer recognises fibrillar structures much better, hence that it was not suited to resolve the smallest aggregates, but even larger ones were not clearly visible which was surprising, as I was able to detect aggregates with said aptamer in cells. It could be a surface effect, as I was not able to validate, that the unlabelled protein readily binds to aspartic acid. Altogether this does not mean it is not possible to do DNA-PAINT with Aβ42 aggregates, but it needs refinement with both surfaces and maybe aptamer alternatives.

5.2.2 Biological effects

The structural study of the Aβ42 aggregates is important but I was afurthermore interested in the biological implications of the structural changes. As stated before, it is thought that both the Ca^{2+} homeostasis is adversely affected in AD and also that neuroinflammation could play a role. Thus, these are the two biological consequences that I analysed.

To examine the effects of aggregate size on Ca^{2+} influx through membranes I used the ultrasensitive measurement of Ca^{2+} influx into vesicles as described by Flagmeier and De et al. [92]. This allowed me to quantitatively and sensitively detect the presence of Aβ42 oligomers. But more importantly, in comparison to kinetic experiments, I could quantitate the relative amount of aggregates in the samples and used this information to normalise the response from the assay. I saw the biggest increase in Ca^{2+} influx, which is the measure of Aβ42 oligomers, in the smallest fractions (Figure 43 B). The absolute numbers of pFTAA active aggregates to calculate the response per aggregate are shown in Table 7. The results are consistent with the increase measured during a time-course of an Aβ42 aggregation.

Table 7 Confocal pFTAA aggregate count used to correct the Ca^{2+} assay as shown below.

Sample	Aggregate Count
10 %	457100
20 %	89200
30 %	15420
40 %	15300
50 %	39760

This increase becomes exaggerated if we normalise for the relative abundance of amyloid aggregates (as measured with pFTAA in solution). This means that the oligomer fractions induced the greatest calcium influx into single vesicles. The molecular mechanism of this Ca^{2+} influx however is unclear but may be some form of membrane perturbation or facilitated permeability. Arguably the vesicle membrane is far less complex and devoid of receptors in comparison to the cell membrane of e.g. the microglia cells. The increased calcium influx into vesicles through membrane perturbation seems not to be the same mechanism as the inflammatory response

through the microglia cells as the peaks appear at different sizes of aggregates. This lends itself to speculate that oligomers of Aβ42 aggregates are distinct from the aggregates causing neuroinflammation which I will discuss in the following section.

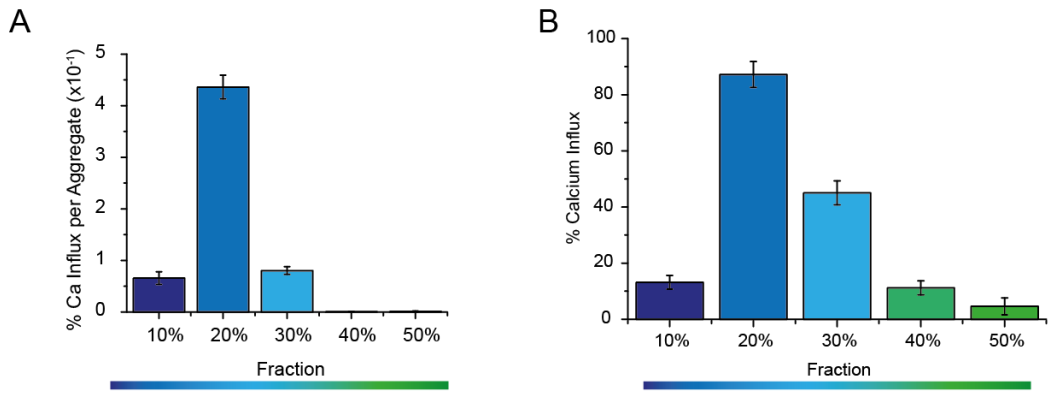

Figure 43 Ultrasensitive measurement of calcium influx of Aβ42 oligomers. (A) The calcium influx per detected pFTAA active aggregate percentage for the various sizes is shown. The mean is shown with error bars as standard deviation. (B) The uncorrected calcium influx data directly from the assay. The mean of three repeats each of all measured vesicles with standard deviation as error bars is shown.

I have not used the equivalent smFRET measurements to normalise the response of the Ca^{2+} influx as the experimental protocol for the aggregation differed. In the case of the smFRET experiments I used a single timepoint as basis for the gradient centrifugation whereas in the unlabelled experiments I used multiple aggregation timepoints and pre-mixed them. The rationale behind this is, that the methods used to measure the unlabelled aggregates are not as sensitive as the smFRET, so more aggregates overall in each fraction are needed to get a good sampling. As the timepoints and hence the underlying relative proportions of aggregates can be different between labelled and unlabelled a different approach is needed. The selection of compatible dyes between the smFRET and the Ca^{2+} influx measurement could help resolve that problem.

Aβ42 induced Pro-Inflammatory Response of Microglia Cells

To evaluate the neuroinflammatory potential I used mouse microglia cells and measured their TNFα release upon addition of the Aβ42 aggregates (which are found mostly in the extracellular space) [86]. We did not only examine the effects of the size of the aggregates on membrane perturbation, but I also measured the TNFα production of mouse microglia cells per aggregate. The dual-labelled co-aggregates are diluted into the medium at nanomolar concentrations and the TNFα release is measured 24 h and 48 h post addition. Neither the remaining sucrose nor the labelled Aβ42 monomer gives any appreciable response (Figure 44). The aggregates were measured with the smFRET technique on the day of application onto the cells.

The ELISA showed a maximum TNFα response with the aggregates of the 30% fraction after being corrected for the per aggregate response as measured with confocal FRET. This suggests that different size aggregates have different effects. TNFα levels reduce again after 48h of incubation of the cells in the 30% and 40% fractions, close to levels of the very large aggregates. The 10% and 20% fraction aggregates lead to an increase and unchanged release of TNFα after 48h. This could be explained by a continuation of the aggregation and hence conversion to larger aggregates. This is particular apparent in the consistent increase in TNFα over the 24 h in the 10 % and the opposite effect very strongly in the 30 % and then still present in the 40 % and 50 % fractions.

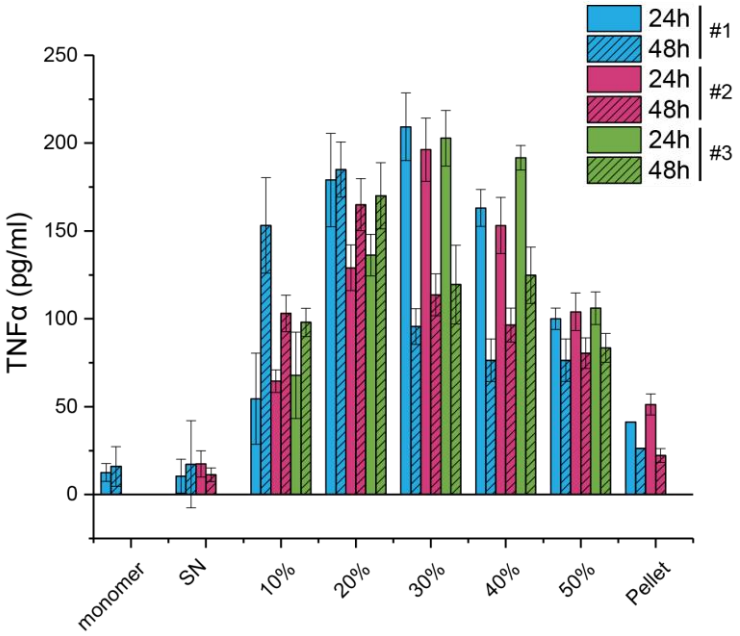

Figure 44 Three full biological repeats of the TNFα ELISA tested after 24 h and 48 h after addition of the aggregates. Each bar represents the mean of 3 measurements with the standard deviation as error. I prepared and provided the aggregates and Dr. Craig Hughes measured the TNFα in the mouse microglia

In the lowest fraction I found a much higher number of donor events compared to the other fractions. This is a result of a highly concentrated monomer and hence small-mer solution in the supernatant which is partially found in the 10 % fraction. Hence the small-mers contribute to the much-increased number of FRET events from the input solution. I could not find any TNFα increase with pure monomer. Hence, I assumed that I could use the aggregate number directly. The fraction of aggregates is comparable to the other samples too (Table 8). The aggregate number was then used directly to give a semi-quantitative method to interpret the increase in TNFα. The detailed numbers of the FRET numbers that were used to correct the below ELISA are given in Table 8.

Table 8 No. of FRET events, donor events and the fraction of aggregates used correct the TNFα assay. The values are the mean and standard deviation of three full technical repeats including aggregation and centrifugation step. The individual measurements of the according preparation was used to correct the respective TNFα assay.

Sample	No. of FRET aggregates (x 10^3)	No. of donor events (x 10^5)	Percentage of aggregates
10 %	168± 20	63.2± 850.1	0.007± 0.006
20 %	33± 39	63.7± 84.2	0.013± 0.008
30 %	10± 5	6.2± 8.0	0.099± 0.090
40 %	9± 4	7.2± 9.4	0.091± 0.095
50 %	14± 18	3.3± 4.5	0.109± 0.094

The TNFα ELISA showed a maximum at the 30 % fraction, which was identified as containing protofilaments. This is apparent in the ELISA results (Figure 45 A) and gets exaggerated by the correction applied by the smFRET measurements (Figure 45 B).

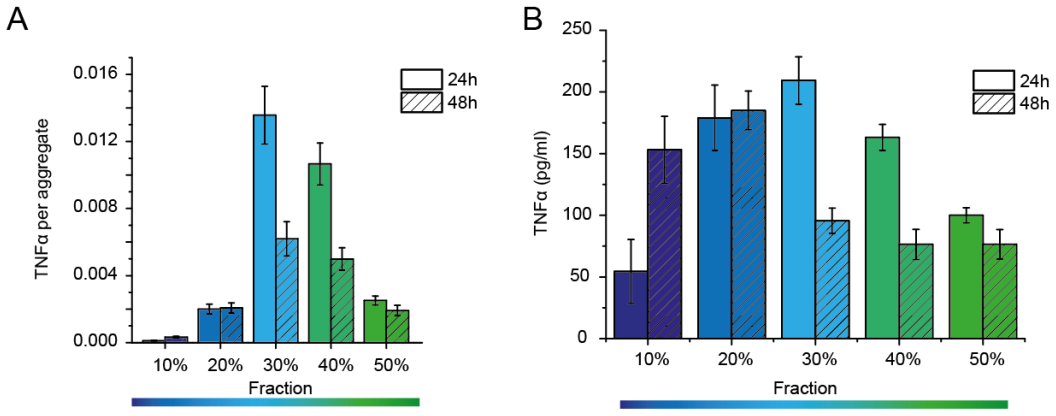

Figure 45 The TNFα increase per aggregate after correction with the relative abundance of protein aggregate shows an increase towards medium sized aggregates and very little response to smaller aggregates. (N=3; one shown) (B) The absolute measured response of TNFα as determined with ELISA. All bars are the mean of three replicates with the error bare the standard deviation.

5.3 Outlook on size dependent effects

I have shown in this chapter that it is possible to study a cross-section of aggregate sizes in parallel. This has two advantages over kinetic studies. Firstly, it decouples the preparation from kinetic variability, which is still a major "headache" in many aggregation experiments. Secondly, it allows us to directly compare numerous stages at the same time with adequate aggregate numbers.

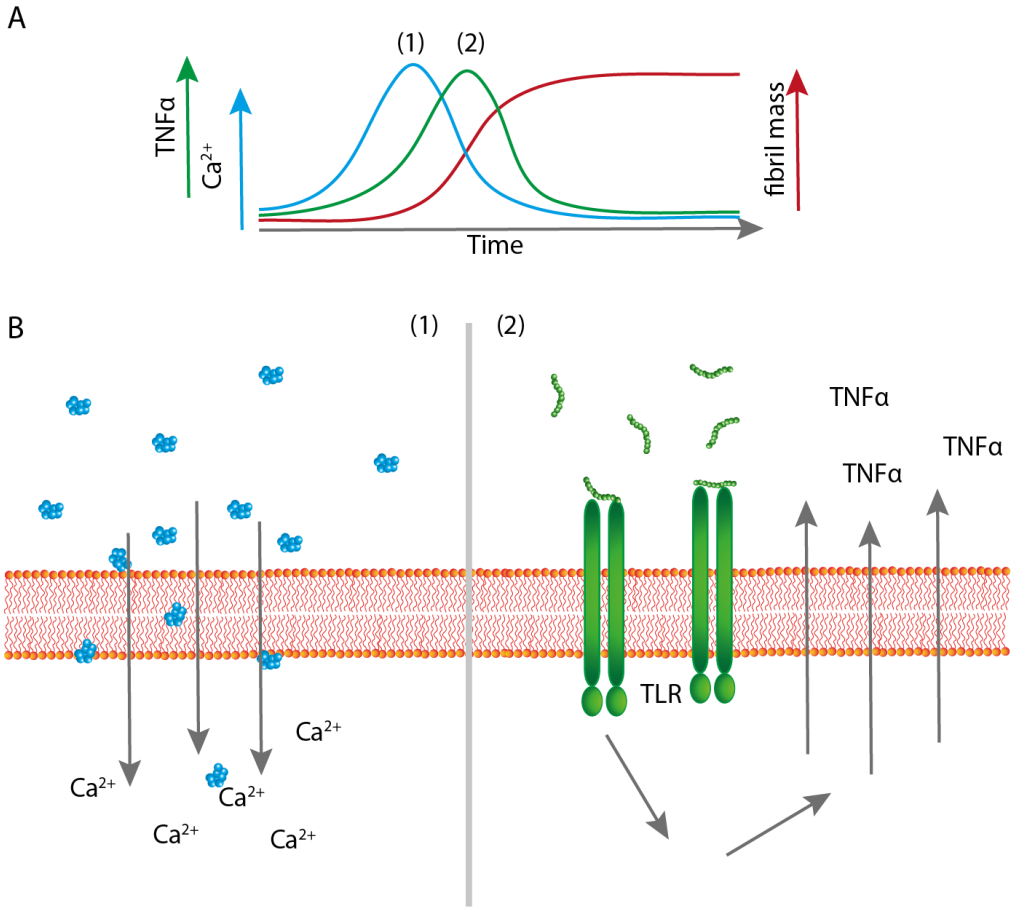

Figure 46 Model for the different effects on cell membranes and microglia cells through Aβ42 oligomers and protofilaments. (A) The graph shows a simplified view on the aggregation and their respective predominant species with the two important points marked with (1) where predominantly oligomers are present and (2) where protofilaments are present. These two points correlate with the maximum response in (1) Ca^{2+} influx and (2) a maximum pro-inflammatory response. (B) The schematic shows the possible underlying mechanisms of these two effects with Ca^{2+} influx

Furthermore, I found that protofilaments, not oligomers or fibrils, induce a pro-inflammatory response. To confirm that the observed effects were not artefacts of varying concentrations of aggregate types, it was corrected to the response per aggregate using smFRET. I also normalised the measurement of the calcium influx into vesicles (with the limitation of normalising to pFTAA positive aggregates). The

maximum calcium influx was observed with the small oligomeric species which matches the findings of kinetic studies [92].

Continuing from the first part, it would be intriguing to see what effect the various species have on Ca^{2+} influx and pro-inflammatory response in a combined cell model. This could for example be a combination of a single cell assay and a parallel inflammatory response measurement. We could then use targeted/ designed antibodies to bind to subsets of these aggregates, now that we have methods to purify, measure and test them biologically. This all could ultimately help to understand the underlying molecular mechanisms of aggregates in the brain better.

Interestingly, the fact that the protofilaments are most potent at inducing the inflammatory response suggests a molecular mechanism. The TLR3 receptor has a cavity that can bind elongated structures of about 1 nm in diameter as shown with bound RNA (Figure 47). Protofilaments also have the same elongated shape as the bound RNA with a similar diameter.

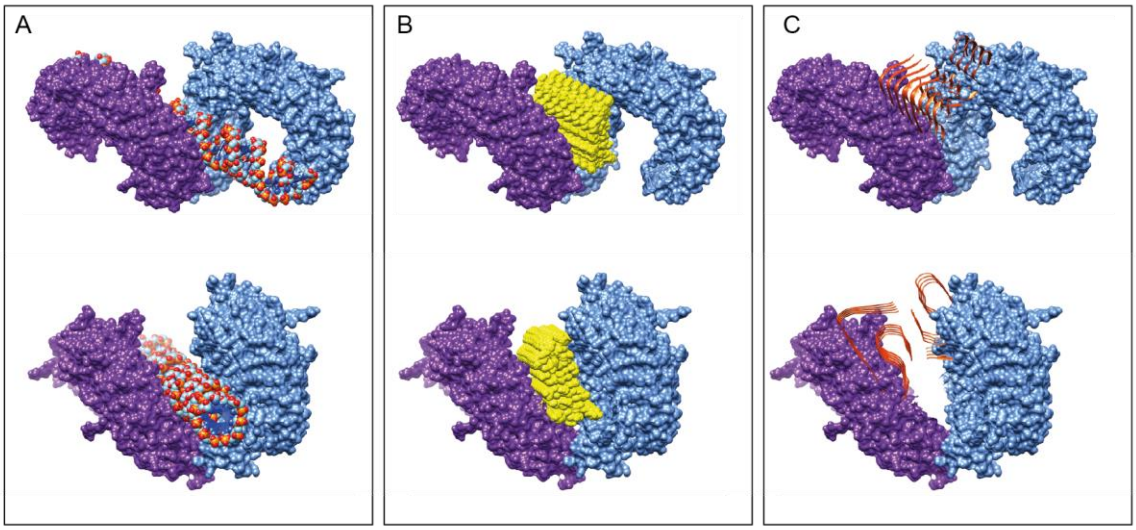

Figure 47 (A) The crystallography structure of the ectodomain of the TLR3 receptor bound to RNA (accession number 3CIY) according to [299] is shown in a top (top) and side view along the RNA, filament and fibril axis respectively (bottom). (B) The structure of a cross-beta filament is superimposed (accession number 2M5N [300]) where the RNA would usually bind. The cleft would have the correct diameter to accommodate this structure in contrast to (C) where the structure of an Aβ42 fibril is superimposed (accession number 5OQV [116]). The cleft is clearly too narrow to accommodate a structure this size. This could explain the findings with the TNFα measurements.

6 Future Work

The combination of single molecule techniques in studying human aggregates in CSF bears a variety of advantages but is still at the very beginning. Before further extending on the use of various dyes as diagnostic tool in PD or AD, I think the results of the AD SAVE application demand for more groundwork. Most crucially we need to identify what the exact composition the aggregates we detect. This includes (A) the aggregates itself, whether they consist of Aβ42 only, various different cleavage products, co-aggregates and/ or other aggregates and (B) any possible interaction partners, most notably chaperones such as clusterin or various heat-shock proteins.

One possible way to better understand the aggregates is the extension of the competition assay with clusterin into the CSF. This would give insights into possible clearance mechanisms and interactions. There is also an option of the use of antibodies and eventually multiplexing while imaging single aggregates. This has already been explored by Zhang et al. [125]. But rather than focusing solely the diagnostic side, I think it these tools help understand the molecular nature of the human aggregates and their interactions in the extracellular space.

A different approach to investigate the molecular nature of the aggregates is by IP. I described an IP experiment we used to demonstrate, that the Ca^{2+} influx in the vesicle assay is can be decreased by IP with Aβ42 specific antibodies. However, ultimately it would be intriguing to identify amyloid aggregates more general, e.g. with immobilised ß-sheet binding entities such as ThT and derivatives. These could then be analysed by e.g. mass spectrometry to explore their molecular composition. This would be an antibody unbiased view that could also give us insight into the strengths and weaknesses of the SAVE method.

The conclusions about the oligomers and protofilaments in chapter 5 are interesting in the light of the aggregates in human CSF. The implications of protofilaments present in the CSF and the brain would have implications for treatment and could help understand some of the molecular and cellular consequences in the brain. I will discuss two ways of connecting the work I have presented.

We could use the gradient centrifugation to purify aggregates from human CSF to study their effects in isolation. This would be made possible by the very sensitive

detection methods we have at hand. A handful of improvements would be beneficial. As CSF samples are very low in volume and the number of aggregates is very low, a downscaling of the gradient would be ideal. We could use more sophisticated gradient mixes e.g. linear gradients and better sample collecting techniques to either focus on one particular species or get a finer sampling.

The other way to connect the findings from this thesis would be to specifically look for species in the CSF we already identified. Especially protofilaments could be of interest, to see how abundant they are in the CSF. We could use AFM to detect the protofilaments. This comes with the problem of a very diverse mix of proteins in the CSF that would potentially be detected. However, pre-treatment with Proteinase K could help to digest most non-fibrillar and non-filamentous proteins and probe for the presence of protofilaments in the CSF.

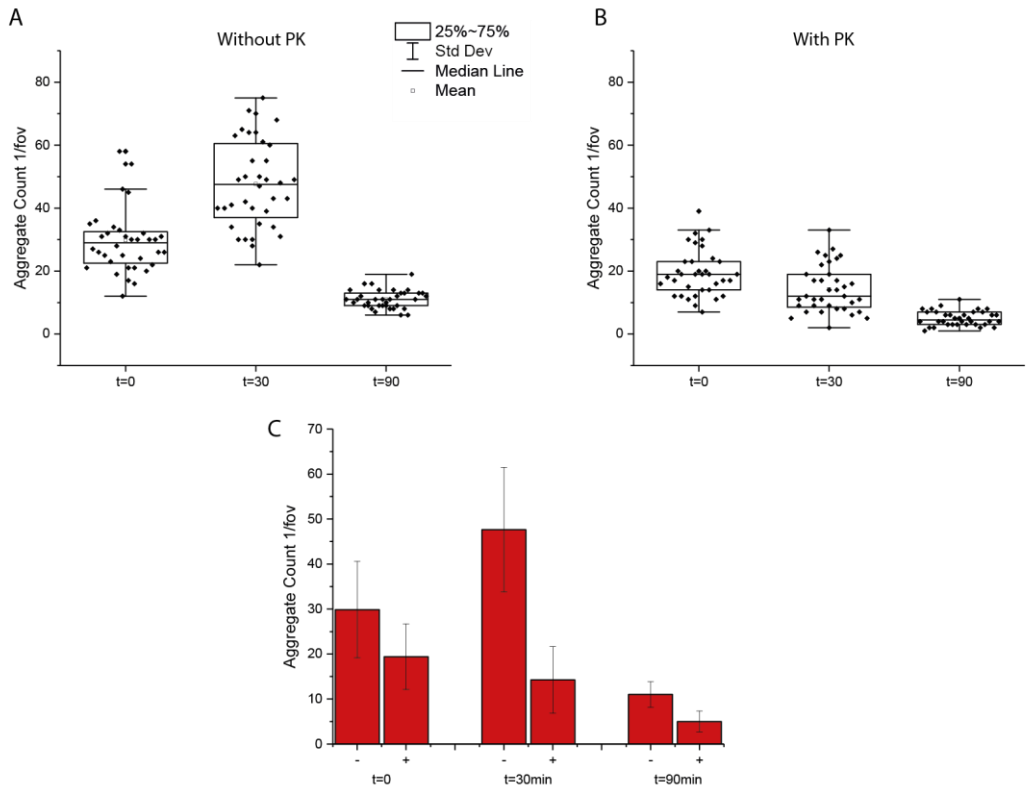

Figure 48 SAVE imaging of a CSF sample to test the decrease in ThT active aggregates after incubation with PK in preparation for AFM imaging experiments. Time course of the aggregate count (A) without PK and (B) with PK of three technical repeats. The aggregates of all three times the 12 fov are shown with box and error bars as indicated. (C) shows the direct comparison of the aggregate count per fov and the decrease after 30 min and 90 min.

To explore this option, I performed some preliminary experiments. These showed that there is only a small reduction of the ThT-active aggregates in the CSF with a pre-

incubation with 0.1 µM Proteinase K (Figure 48). This could be a suitable pre-treatment to AFM to probe for the presence of protofilaments.

Super- resolution imaging of Aβ with a "brain in a dish"

In addition to above cell-biological and biophysical characterisation I explored options of imaging the pre-separated aggregates *in vivo*. Importantly for this experiment we need a resolution beyond the diffraction limit, as the differences between the oligomers are mostly below 200nm. I was interested if we could see a distinct difference in uptake, spreading and effect on human cortical neurons in a microfluidic device (Figure 49). This device is constructed to separate the compartments of the cell bodies with only the neurons in the central channel. The different fluid levels assure a pressure difference, so any agents added to one side of the chamber can only go across via active transport and not diffusion.

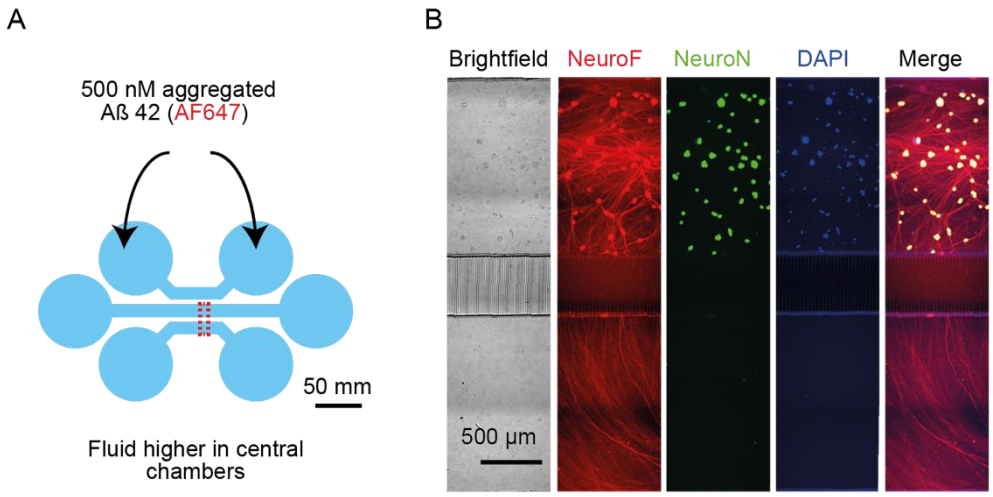

Figure 49 Schematic of the microfluidic device to study spreading of Aβ aggregates. (A) The microfluidic chamber consists of two compartments divided with a central channel connected via fine channels. The cell bodies are added on one side the neuronal axons will grow through the central channel. The higher fluid in the central compartment avoids any diffusion through the channels. All aggregates crossing from one side to the other can only do so by active transport/ spreading by the cells along the axons. (B) Wide-field images of the microfluidic device stained with various neuronal and axonal markers to demonstrate the presence of axons in absence of cell bodies in the central chamber. This schematic was kindly provided by Dr. M. Horrocks.

Firstly, we confirmed the suitability of DNA-PAINT for imaging of Aβ aggregates [201]. I used fluorescently labelled Aβ aggregates to confirm coincidence between the aggregates in the cell and the localisations detected via DNA-PAINT. DNA-PAINT uses a DNA Aptamer specific for amyloid aggregates as binding entity with a short complementary DNA-strand extension. This extension transiently binds its complement which has a fluorophore attached. This allows for PAINT imaging for

prolonged time without any of the disadvantages of photochemical blinking of the dye itself.

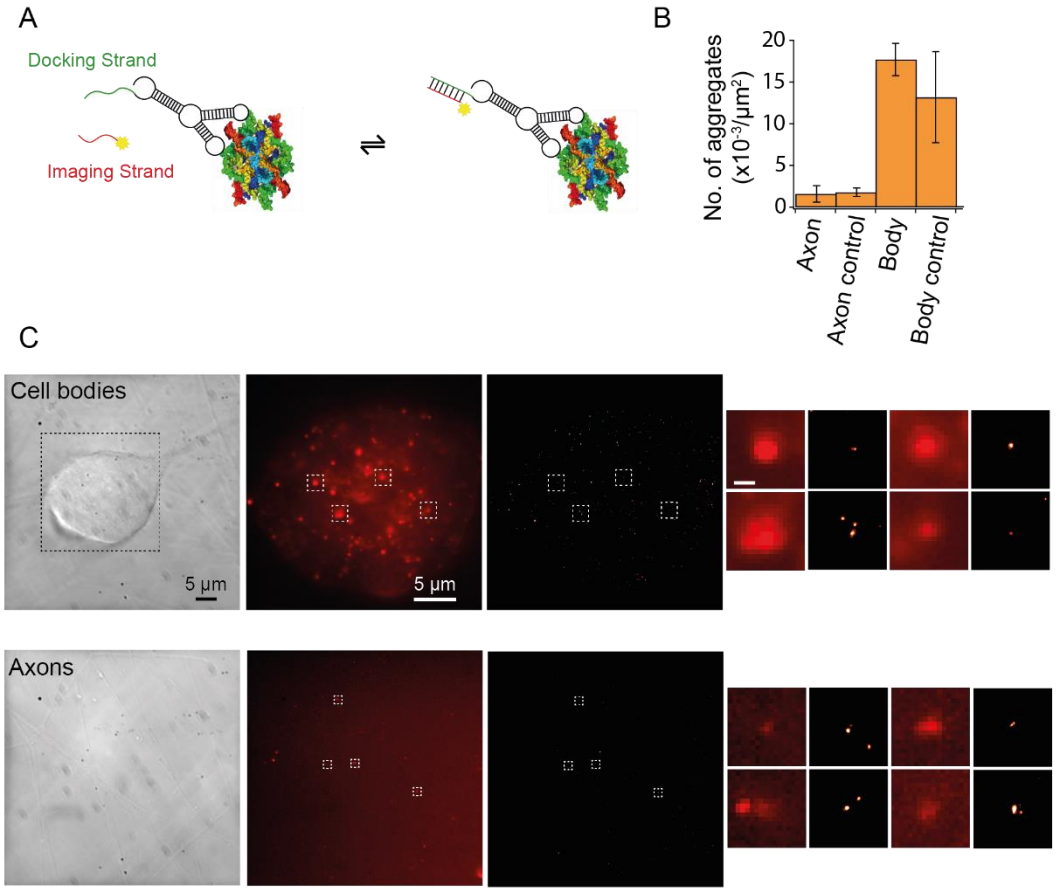

Figure 50 DNA-PAINT experiment to show imaging capabilities of DNA-PAINT to image Aβ42 aggregates in fixed neuronal cells. (A) The principle of DNA-PAINT is based on the PAINT technique as described with a docking strand attached to a DNA-aptamer which binds amyloid structures. A complementary imaging strand with a fluorophore attached is then usesd for PAINT in the cells. (B) The number of aggregates as detected with the fluorophore is displayed compared to an empty control (C) Representative widefield, TIRF and DNA-PAINT images are shown. The inset on the right shows the increase in resolution in the reconstructed image. This schematic was kindly provided by Dr. M. Horrocks.

I first confirmed that the Aptamer co-localises with covalently labelled Aβ42-647 in our cell model. I can clearly see an increase in resolution (Figure 50 C)

We tried to show the spreading of Aβ42-647 along the axons from one cell body into another by adding high nanomolar concentrations of predominantly oligomeric aggregates. This was done without any size separation steps to maintain high protein concentrations and as a proof of principle experiment.

Ultimately the goal is not only to study spreading in these devices but also the effect on white matter and myelination of neuronal cells. For this purpose, the cell

culture inserts would have added oligodendrocytes in the central chamber. Myelination and white matter lesions have been implicated in AD but not much is known about the process so far [301]. The described technique could help to get a controlled model that we could image on SR level and with the DNA-PAINT technique further down the line even multiplex. This would help to get insights into the interactions of the amyloid aggregates with oligodendrocytes and neurons and their effect on white matter and myelination.

7 Concluding Remarks

In the presented body of work, I have demonstrated that the study of amyloid aggregates in CSF can give us valuable insights into the nature of human aggregates. This question is particularly suited to the strengths of the biophysical methods. I have shown how the SAVE technique can be used with other dyes than ThT and that a dimeric variant of the ThT molecule is the most viable of the tested dyes.

I have shown that SAVE is limited in its application as diagnostic tool in AD cases. It can however help to understand the effects of external factors on aggregates such as antibodies and nanobodies. I showed that, despite having an effect on Ca^{2+} Influx the antibody and nanobody did not change the structure of the aggregates.

Finally, I showed the structure-function relationship for Ca^{2+} influx into vesicles and the inflammatory response of microglial cells. With the help of gradient ultracentrifugation and in-depth structural characterisation I showed that oligomers are the main inducers of Ca^{2+} influx whereas protofilaments are most potent in inducing TNFα. Mature fibrils seem to have little to no effect on both parameters.

8 Publications

{ Size-dependent Structure and Effect of Aβ42 aggregates. De S**†**, **Wirthensohn DC†**, Flagmeier P**†**, Hughes C**†**, Aprile FA, Ruggeri FS, Whiten DR, Emin D, Sormani P, Knowles TPJ, Dobson CM, Bryant C, Vendruscolo M, Klenerman D **Nature Structural and Molecular Biology** (*preparing submission*) **†contributed equally** }

Nanoscopic characterization of individual protein aggregates in human neuronal cells. Whiten DR†, Zuo Y†, Calo L, Choi M-L, De S, Flagmeier P, **Wirthensohn DC**, Kundel F, Lee SF, Dobson CM, Gandhi S, Spillantini M-G, Klenerman D, Horrocks MH, **Chemical Sciences** (*under review*) †contributed equally

Shedding light on aberrant interactions: A review of modern tools for studying protein aggregates. Kundel F**†**, Tosatto L**†**, Whiten DR**†**, **Wirthensohn DC†,** Horrocks MH, Klenerman D **FEBS Journal** 2018 Mar 4, doi:10.1111/febs.14409. **†contributed equally**

Inhibiting Ca^{2+} influx induced by aggregates in human CSF, Drews A**†**, De S**†**, Flagmeier P**†**, **Wirthensohn DC†**, Chen WH, Whiten DR, Vincke C, Mulydermans S, Paterson RW, Slattery CF, Fox NC, Schott JM, Zetterberg H, Dobson CM, Gandhi S, Klenerman D., **Cell Reports** 2017 Dec 12, 21 (11), p3310–3316. **†contributed equally**

Ultrasensitive Measurement of Ca^{2+} Influx into Lipid Vesicles Induced by Protein Aggregates. Flagmeier P, De S, **Wirthensohn DC**, Lee SF, Vincke C, Muyldermans S, Knowles TPJ, Gandhi S, Dobson CM, Klenerman D. **Angewandte Chemie Int Ed Engl**. 2017 Jun 26;56(27):7750-7754.

Multi-dimensional super-resolution imaging enables surface hydrophobicity mapping. Bongiovanni MN, Godet J, Horrocks MH, Tosatto L, Carr AR, **Wirthensohn DC**, Ranasinghe RT, Lee JE, Ponjavic A, Fritz JV, Dobson CM, Klenerman D, Lee SF. **Nature Communications**. 2016 Dec 8;7:13544.

Individual aggregates of amyloid beta induce temporary calcium influx through the cell membrane of neuronal cells, Drews A, Flint J, Shivji N, Jönsson P, **Wirthensohn D**, De Genst E, Vincke C, Muyldermans S, Dobson C, Klenerman D. **Scientific Reports**. 2016 Aug 24;6:31910.

9 References

[1] 2016 WHO, **2018**, 1–6.

[2] A. Alzheimer, *Allg. Z. Psychiatr. Psych. Med.* **1907**, *64*, 146–148.

[3] J. Parkinson, *J. Neuropsychiatry Clin. Neurosci.* **2002**, *14*, 223–236; discussion 222.

[4] M. Goedert, M. G. Spillantini, K. Del Tredici, H. Braak, *Nat. Rev. Neurol.* **2013**, *9*, 13–24.

[5] C. L. Masters, G. Simms, N. A. Weinman, G. Multhaup, B. L. McDonald, K. Beyreuther, *Proc. Natl. Acad. Sci.* **1985**, *82*, 4245–4249.

[6] J. P. Brion, A. M. Couck, E. Passareiro, J. Flament-Durand, *J. Submicrosc. Cytol.* **1985**, *17*, 89–96.

[7] I. Grundke-Iqbal, K. Iqbal, M. Quinlan, Y. C. Tung, M. S. Zaidi, H. M. Wisniewski, *J. Biol. Chem.* **1986**, *261*, 6084–9.

[8] N. J. Pollock, S. S. Mirra, L. I. Binder, L. A. Hansen, J. G. Wood, *Lancet (London, England)* **1986**, *2*, 1211.

[9] M. Goedert, C. M. Wischik, R. A. Crowther, J. E. Walker, A. Klug, *Proc. Natl. Acad. Sci. U. S. A.* **1988**, *85*, 4051–4055.

[10] M. G. Spillantini, M. L. Schmidt, V. M.-Y. Lee, J. Q. Trojanowski, R. Jakes, M. Goedert, **1997**, *388*, 839–840.

[11] M. Goedert, *Science* **2015**, *349*, 1255555.

[12] T. Crowther, M. Goedert, C. M. Wischik, *Ann. Med.* **1989**, *21*, 127–32.

[13] C. Duyckaerts, *Rev. Neurol. (Paris).* **2013**, *169*, 825–833.

[14] M. Goedert, B. Ghetti, M. G. Spillantini, *Cold Spring Harb. Perspect. Med.* **2012**, *2*, a006254.

[15] F. Chiti, C. M. Dobson, *Annu. Rev. Biochem.* **2006**, *75*, 333–366.

[16] F. Chiti, C. M. Dobson, *Annu. Rev. Biochem.* **2017**, *86*, 27–68.

[17] F. Chiti, M. Stefani, N. Taddei, G. Ramponi, C. M. Dobson, *Nature* **2003**, *424*, 805–808.

[18] C. M. Dobson, *Nature* **2003**, *426*, 884–890.

[19] S. I. A. Cohen, S. Linse, L. M. Luheshi, E. Hellstrand, D. A. White, L. Rajah, D. E. Otzen, M. Vendruscolo, C. M. Dobson, T. P. J. Knowles, *Proc. Natl. Acad. Sci. U. S. A.* **2013**, *110*, 9758–63.

[20] A. K. Buell, C. Galvagnion, R. Gaspar, E. Sparr, M. Vendruscolo, T. P. J. Knowles, S. Linse, C. M. Dobson, *Proc. Natl. Acad. Sci. U. S. A.* **2014**, *111*, 7671–7676.

[21] S. Linse, *Biophys. Rev.* **2017**, DOI 10.1007/s12551-017-0289-z.

[22] J. L. Tomic, A. Pensalfini, E. Head, C. G. Glabe, *Neurobiol. Dis.* **2009**, *35*, 352–358.

[23] C. A. Lasagna-Reeves, D. L. Castillo-Carranza, M. J. Guerrero-Muoz, G. R. Jackson, R. Kayed, *Biochemistry* **2010**, *49*, 10039–10041.

[24] C. A. Lasagna-Reeves, D. L. Castillo-Carranza, U. Sengupta, A. L. Clos, G. R. Jackson, R. Kayed, *Mol. Neurodegener.* **2011**, *6*, 39.

[25] K. Flach, I. Hilbrich, A. Schiffmann, U. Gärtner, M. Krüger, M. Leonhardt, H. Waschipky, L. Wick, T. Arendt, M. Holzer, *J. Biol. Chem.* **2012**, *287*, 43223–43233.

[26] R. M. Koffie, M. Meyer-Luehmann, T. Hashimoto, K. W. Adams, M. L. Mielke, M. Garcia-Alloza, K. D. Micheva, S. J. Smith, M. L. Kim, V. M. Lee, et al., *Proc. Natl. Acad. Sci.* **2009**, *106*, 4012–4017.

[27] M. P. Lambert, A. K. Barlow, B. A. Chromy, C. Edwards, R. Freed, M. Liosatos, T. E. Morgan, I. Rozovsky, B. Trommer, K. L. Viola, et al., *Proc. Natl. Acad. Sci.* **1998**, *95*, 6448–6453.

[28] S. Li, S. Hong, N. E. Shepardson, D. M. Walsh, G. M. Shankar, D. Selkoe, *Neuron* **2009**, *62*, 788–801.

[29] G. M. Shankar, S. Li, T. H. Mehta, A. Garcia-Munoz, N. E. Shepardson, I. Smith, F. M. Brett, M. A. Farrell, M. J. Rowan, C. A. Lemere, et al., *Nat. Med.* **2008**, *14*, 837–842.

[30] M. Ahn, C. L. Hagan, A. Bernardo-Gancedo, E. De Genst, F. N. Newby, J. Christodoulou, A. Dhulesia, M. Dumoulin, C. V. Robinson, C. M. Dobson, et al., *Biophys. J.* **n.d.**, *111*, 2358–2367.

[31] K. A. Conway, S. J. Lee, J. C. Rochet, T. T. Ding, R. E. Williamson, P. T. Lansbury, *Proc. Natl. Acad. Sci. U. S. A.* **2000**, *97*, 571–576.

[32] V. N. Uversky, J. Li, A. L. Fink, *J. Biol. Chem.* **2001**, *276*, 10737–10744.

[33] F. J. B. Bäuerlein, I. Saha, A. Mishra, M. Kalemanov, A. Martínez-Sánchez, R. Klein, I. Dudanova, M. S. Hipp, F. U. Hartl, W. Baumeister, et al., *Cell* **2017**, *171*, 179–187.e10.

[34] K. A. Conway, J. D. Harper, P. T. Lansbury, *Biochemistry* **2000**, *39*, 2552–2563.

[35] P. Arosio, T. P. J. Knowles, S. Linse, *Phys. Chem. Chem. Phys. PCCP* **2015**, *17*, 7606–7618.

[36] T. Shirahama, A. S. Cohen, *Nature* **1965**, *206*, 737–738.

[37] F. Kundel, L. Tosatto, D. R. Whiten, D. C. Wirthensohn, M. H. Horrocks, D. Klenerman, *FEBS J.* **2018**, DOI 10.1111/febs.14409.

[38] B. Winner, R. Jappelli, S. K. Maji, P. A. Desplats, L. Boyer, S. Aigner, C. Hetzer, T. Loher, M. Vilar, S. Campioni, et al., *Proc. Natl. Acad. Sci. U. S. A.* **2011**, *108*, 4194–4199.

[39] E. Rockenstein, S. Nuber, C. R. Overk, K. Ubhi, M. Mante, C. Patrick, A. Adame, M. Trejo-Morales, J. Gerez, P. Picotti, et al., *Brain* **2014**, *137*, 1496–1513.

[40] N. Cremades, S. I. A. I. A. Cohen, E. Deas, A. Y. Y. Abramov, A. Y. Y. Chen, A. Orte, M. Sandal, R. W. W. Clarke, P. Dunne, F. A. A. Aprile, et al., *Cell* **2012**, *149*, 1048–59.

[41] T. F. Outeiro, P. Putcha, J. E. Tetzlaff, R. Spoelgen, M. Koker, F. Carvalho, B. T. Hyman, P. J. McLean, *PLoS One* **2008**, *3*, e1867.

[42] D. P. Karpinar, M. B. G. Balija, S. Kügler, F. Opazo, N. Rezaei-Ghaleh, N. Wender, H.-Y. Kim, G. Taschenberger, B. H. Falkenburger, H. Heise, et al., *EMBO J.* **2009**, *28*, 3256–3268.

[43] E. S. Luth, I. G. Stavrovskaya, T. Bartels, B. S. Kristal, D. J. Selkoe, *J. Biol. Chem.* **2014**, *289*, 21490–21507.

[44] T. Fagerqvist, T. Näsström, E. Ihse, V. Lindström, C. Sahlin, S. M. F. Tucker, A. Kasaryan, M. Karlsson, F. Nikolajeff, H. Schell, et al., *Amyloid Int. J. Exp. Clin. Investig. Off. J. Int. Soc. Amyloidosis* **2013**, *20*, 233–244.

[45] Z. S. Martin, V. Neugebauer, K. T. Dineley, R. Kayed, W. Zhang, L. C. Reese, G. Taglialatela, *J. Neurochem.* **2012**, *120*, 440–452.

[46] T. J. Kaufmann, P. M. Harrison, M. J. E. Richardson, T. J. T. Pinheiro, M. J. Wall, *J. Physiol.* **2016**, *594*, 2751–2772.

[47] H. LeVine, *Protein Sci.* **1993**, *2*, 404–10.

[48] A. I. Sulatskaya, A. A. Maskevich, I. M. Kuznetsova, V. N. Uversky, K. K. Turoverov, *PLoS One* **2010**, *5*, e15385.

[49] T. P. J. Knowles, C. A. Waudby, G. L. Devlin, S. I. A. Cohen, A. Aguzzi, M. Vendruscolo, E. M. Terentjev, M. E. Welland, C. M. Dobson, *Science* **2009**, *326*, 1533–1537.

[50] S. I. A. A. Cohen, M. Vendruscolo, C. M. Dobson, T. P. J. J. Knowles, *J. Mol. Biol.* **2012**, *421*, 160–171.

[51] H. Naiki, K. Higuchi, K. Nakakuki, T. Takeda, *Lab. Invest.* **1991**, *65*, 104–110.

[52] J. Brelstaff, M. G. Spillantini, A. M. Tolkovsky, *Neural Regen. Res.* **2015**, *10*, 1746–1747.

[53] H. Tong, Y. Hong, Y. Dong, M. Häußler, J. W. Y. Lam, Z. Li, Z. Guo, Z. Guo, B. Zhong Tang, *Chem. Commun.* **2006**, *0*, 3705–3707.

[54] Y. Li, V. Lubchenko, P. G. Vekilov, *Rev. Sci. Instrum.* **2011**, *82*, 053106.

[55] P. Juszczyk, A. S. Kołodziejczyk, Z. Grzonka, *Acta Biochim. Pol.* **2005**, *52*, 425–431.

[56] A. Orte, N. R. Birkett, R. W. Clarke, G. L. Devlin, C. M. Dobson, D. Klenerman, *Proc. Natl. Acad. Sci. U. S. A.* **2008**, *105*, 14424–14429.

[57] J. Bieschke, A. Giese, W. Schulz-Schaeffer, I. Zerr, S. Poser, M. Eigen, H. Kretzschmar, *Proc. Natl. Acad. Sci. U. S. A.* **2000**, *97*, 5468–5473.

[58] A. Giese, B. Bader, J. Bieschke, G. Schaffar, S. Odoy, P. J. Kahle, C. Haass, H. Kretzschmar, *Biochem. Biophys. Res. Commun.* **2005**, *333*, 1202–1210.

[59] M. H. Horrocks, L. Rajah, P. Jönsson, M. Kjaergaard, M. Vendruscolo, T. P. J. Knowles, D. Klenerman, *Anal. Chem.* **2013**, *85*, 6855–6859.

[60] M. H. Horrocks, L. Tosatto, A. J. Dear, G. A. Garcia, M. Iljina, N. Cremades, M. Dalla Serra, T. P. J. Knowles, C. M. Dobson, D. Klenerman, *Anal. Chem.* **2015**, *87*, 8818–8826.

[61] L. Tosatto, M. H. Horrocks, A. J. Dear, T. P. J. Knowles, M. Dalla Serra, N. Cremades, C. M. Dobson, D. Klenerman, *Sci. Rep.* **2015**, *5*, 16696.

[62] E. Haustein, P. Schwille, *Curr. Opin. Struct. Biol.* **2004**, *14*, 531–540.

[63] D. Magde, E. Elson, W. W. Webb, *Phys. Rev. Lett.* **1972**, *29*, 705–708.

[64] D. Axelrod, *J. Cell Biol.* **1981**, *89*, 141–145.

[65] N. Zijlstra, C. Blum, I. M. J. Segers-Nolten, M. M. A. E. Claessens, V. Subramaniam, *Angew. Chem. Int. Ed. Engl.* **2012**, *51*, 8821–8824.

[66] E. Betzig, G. H. Patterson, R. Sougrat, O. W. Lindwasser, S. Olenych, J. S. Bonifacino, M. W. Davidson, J. Lippincott-Schwartz, H. F. Hess, *Science (80-.).* **2006**, *313*, 1642–1645.

[67] M. J. Rust, M. Bates, X. Zhuang, *Nat. Methods* **2006**, *3*, 793–795.

[68] S. W. Hell, J. Wichmann, *Opt. Lett.* **1994**, *19*, 780–782.

[69] A. Szymborska, A. de Marco, N. Daigle, V. C. Cordes, J. A. G. Briggs, J. Ellenberg, *Science* **2013**, *341*, 655–658.

[70] A. Sharonov, R. M. Hochstrasser, *Proc. Natl. Acad. Sci.* **2006**, *103*, 18911–18916.

[71] G. Giannone, E. Hosy, F. Levet, A. Constals, K. Schulze, A. I. Sobolevsky, M. P. Rosconi, E. Gouaux, R. Tampé, D. Choquet, et al., *Biophys. J.* **2010**, *99*, 1303–1310.

[72] R. Jungmann, C. Steinhauer, M. Scheible, A. Kuzyk, P. Tinnefeld, F. C. Simmel, *Nano Lett.* **2010**, *10*, 4756–4761.

[73] R. Jungmann, M. S. Avendaño, J. B. Woehrstein, M. Dai, W. M. Shih, P. Yin, *Nat. Methods* **2014**, *11*, 313–318.

[74] M. N. Bongiovanni, J. Godet, M. H. Horrocks, L. Tosatto, A. R. Carr, D. C. Wirthensohn, R. T. Ranasinghe, J.-E. Lee, A. Ponjavic, J. V. Fritz, et al., *Nat. Commun.* **2016**, *7*, ncomms13544.

[75] V. L. Anderson, W. W. Webb, *BMC Biotechnol.* **2011**, *11*, 125.

[76] K. P. R. Nilsson, *FEBS Lett.* **2009**, *583*, 2593–2599.

[77] M. H. Horrocks, S. F. Lee, S. Gandhi, N. K. Magdalinou, S. W. Chen, M. J. Devine, L. Tosatto, M. Kjaergaard, J. S. Beckwith, H. Zetterberg, et al., *ACS Chem. Neurosci.* **2016**, DOI 10.1021/acschemneuro.5b00324.

[78] D. A. White, A. K. Buell, T. P. J. Knowles, M. E. Welland, C. M. Dobson, *J. Am. Chem. Soc.* **2010**, *132*, 5170–5175.

[79] R. Henderson, P. N. Unwin, *Nature* **1975**, *257*, 28–32.

[80] R. Henderson, J. M. Baldwin, T. A. Ceska, F. Zemlin, E. Beckmann, K. H. Downing, *J. Mol. Biol.* **1990**, *213*, 899–929.

[81] S. W. Chen, S. Drakulic, E. Deas, M. Ouberai, F. A. Aprile, R. Arranz, S. Ness, C. Roodveldt, T. Guilliams, E. J. De-Genst, et al., *Proc. Natl. Acad. Sci. U. S. A.* **2015**, *112*, E1994-2003.

[82] A. W. P. Fitzpatrick, B. Falcon, S. He, A. G. Murzin, G. Murshudov, H. J. Garringer, R. A. Crowther, B. Ghetti, M. Goedert, S. H. W. Scheres, *Nature* **2017**, *547*, 185–190.

[83] M. Schmidt, A. Rohou, K. Lasker, J. K. Yadav, C. Schiene-Fischer, M. Fändrich, N. Grigorieff, *Proc. Natl. Acad. Sci.* **2015**, *112*, 11858–11863.

[84] P. K. Hansma, V. B. Elings, O. Marti, C. E. Bracker, *Science (80-.).* **1988**, *242*, 209–216.

[85] C. Canale, B. Torre, D. Ricci, P. C. Braga, in *At. Force Microsc. Biomed. Res.*, Humana Press, **2011**, pp. 31–43.

[86] C. Haass, D. J. Selkoe, *Nat. Rev. Mol. Cell Biol.* **2007**, *8*, 101–112.

[87] D. J. Selkoe, *Trends Cell Biol.* **1998**, *8*, 447–53.

[88] R. J. O'Brien, P. C. Wong, *Annu. Rev. Neurosci.* **2011**, *34*, 185–204.

[89] H. A. Pearson, C. Peers, *J. Physiol.* **2006**, *575*, 5–10.

[90] M. Sakono, T. Zako, *FEBS J.* **2010**, *277*, 1348–1358.

[91] A. N. Santos, M. Ewers, L. Minthon, A. Simm, R.-E. Silber, K. Blennow, D. Prvulovic, O. Hansson, H. Hampel, *J. Alzheimer's Dis. JAD* **2012**, *29*, 171–176.

[92] P. Flagmeier, S. De, D. C. Wirthensohn, S. F. Lee, C. Vincke, S. Muyldermans, T. P. J. J. Knowles, S. Gandhi, C. M. Dobson, D. Klenerman, *Angew. Chemie Int. Ed.* **2017**, *56*, 7750–7754.

[93] K. Pauwels, T. L. Williams, K. L. Morris, W. Jonckheere, A. Vandersteen, G. Kelly, J. Schymkowitz, F. Rousseau, A. Pastore, L. C. Serpell, et al., *J. Biol. Chem.* **2012**, *287*, 5650–5660.

[94] G. M. Shankar, D. M. Walsh, D. Walsh, M. Rowan, H. Schoemaker, A. Draguhn, K. Wicke, V. Nimmrich, R. Bitner, J. Harlan, et al., *Mol. Neurodegener.* **2009**, *4*, 48.

[95] D. M. Walsh, A. Lomakin, G. B. Benedek, M. M. Condron, D. B. Teplow, *J. Biol. Chem.* **1997**, *272*, 22364–22372.

[96] D. M. Walsh, D. M. Hartley, Y. Kusumoto, Y. Fezoui, M. M. Condron, A. Lomakin, G. B. Benedek, D. J. Selkoe, D. B. Teplow, *J. Biol. Chem.* **1999**, *274*, 25945–52.

[97] R. W. Hepler, K. M. Grimm, D. D. Nahas, R. Breese, E. C. Dodson, P. Acton, P. M. Keller, M. Yeager, H. Wang, P. Shughrue, et al., *Biochemistry* **2006**, *45*, 15157–15167.

[98] J. Laurén, D. A. Gimbel, H. B. Nygaard, J. W. Gilbert, S. M. Strittmatter, *Nature* **2009**, *457*, 1128–1132.

[99] L. Yu, R. Edalji, J. E. Harlan, T. F. Holzman, A. P. Lopez, B. Labkovsky, H. Hillen, S. Barghorn, U. Ebert, P. L. Richardson, et al., *Biochemistry* **2009**, *48*, 1870–1877.

[100] M. Hoshi, M. Sato, S. Matsumoto, A. Noguchi, K. Yasutake, N. Yoshida, K. Sato, *Proc. Natl. Acad. Sci.* **2003**, *100*, 6370–6375.

[101] A. Noguchi, S. Matsumura, M. Dezawa, M. Tada, M. Yanazawa, A. Ito, M. Akioka, S. Kikuchi, M. Sato, S. Ideno, et al., *J. Biol. Chem.* **2009**, *284*, 32895–32905.

[102] D. M. Walsh, M. Townsend, M. B. Podlisny, G. M. Shankar, J. V Fadeeva, O. El Agnaf, D. M. Hartley, D. J. Selkoe, *J. Neurosci.* **2005**, *25*, 2455–2462.

[103] M. B. Podlisny, B. L. Ostaszewski, S. L. Squazzo, E. H. Koo, R. E. Rydell, D. B. Teplow, D. J. Selkoe, *J. Biol. Chem.* **1995**, *270*, 9564–9570.

[104] S. Lesné, M. T. Koh, L. Kotilinek, R. Kayed, C. G. Glabe, A. Yang, M. Gallagher, K. H. Ashe, *Nature* **2006**, *440*, 352–357.

[105] J. C. Stroud, C. Liu, P. K. Teng, D. Eisenberg, *Proc. Natl. Acad. Sci. U. S. A.* **2012**, *109*, 7717–7722.

[106] M. Ahmed, J. Davis, D. Aucoin, T. Sato, S. Ahuja, S. Aimoto, J. I. Elliott, W. E. Van Nostrand, S. O. Smith, *Nat. Struct. Mol. Biol.* **2010**, *17*, 561–7.

[107] J. D. Harper, C. M. Lieber, P. T. Lansbury Jr., *Chem. Biol.* **1997**, *4*, 951–959.

[108] A. Parbhu, H. Lin, J. Thimm, R. Lal, *Peptides* **2002**, *23*, 1265–1270.

[109] M. Bartolini, M. Naldi, J. Fiori, F. Valle, F. Biscarini, D. V. Nicolau, V. Andrisano, *Anal. Biochem.* **2011**, *414*, 215–225.

[110] E. A. Yates, E. M. Cucco, J. Legleiter, *ACS Chem. Neurosci.* **2011**, *2*, 294–307.

[111] F. S. Ruggeri, J. Adamcik, J. S. Jeong, H. A. Lashuel, R. Mezzenga, G. Dietler, *Angew. Chemie Int. Ed.* **2015**, *54*, 2462–2466.

[112] J.-X. Lu, W. Qiang, W.-M. Yau, C. D. Schwieters, S. C. Meredith, R. Tycko, *Cell* **2013**, *154*, 1257–1268.

[113] M. T. Colvin, R. Silvers, Q. Z. Ni, T. V. Can, I. Sergeyev, M. Rosay, K. J. Donovan, B. Michael, J. Wall, S. Linse, et al., *J. Am. Chem. Soc.* **2016**, *138*, 9663–9674.

[114] W. Qiang, W.-M. Yau, J.-X. Lu, J. Collinge, R. Tycko, *Nature* **2017**, *541*, 217–221.

[115] D. Eisenberg, M. Jucker, *Cell* **2012**, *148*, 1188–1203.

[116] L. Gremer, D. Schölzel, C. Schenk, E. Reinartz, J. Labahn, R. B. G. Ravelli, M. Tusche, C. Lopez-Iglesias, W. Hoyer, H. Heise, et al., *Science (80-.).* **2017**, *358*, 116–119.

[117] H. Ding, P. T. Wong, E. L. Lee, A. Gafni, D. G. Steel, *Biophys. J.* **2009**, *97*, 912–21.

[118] P. Narayan, S. Meehan, J. A. Carver, M. R. Wilson, C. M. Dobson, D. Klenerman, *Biochemistry* **2012**, *51*, 9270–9276.

[119] P. Narayan, A. Orte, R. W. Clarke, B. Bolognesi, S. Hook, K. A. Ganzinger, S. Meehan, M. R. Wilson, C. M. Dobson, D. Klenerman, *Nat. Struct. Mol. Biol.* **2012**, *19*, 79–83.

[120] P. Narayan, K. M. Holmström, D.-H. Kim, D. J. Whitcomb, M. R. Wilson, P. St. George-Hyslop, N. W. Wood, C. M. Dobson, K. Cho, A. Y. Abramov, et al., *Biochemistry* **2014**, *53*, 2442–2453.

[121] P. Narayan, K. A. Ganzinger, J. McColl, L. Weimann, S. Meehan, S. Qamar, J. A. Carver, M. R. Wilson, P. St. George-Hyslop, C. M. Dobson, et al., *J. Am. Chem. Soc.* **2013**, *135*, 1491–1498.

[122] M. Iljina, G. A. Garcia, A. J. Dear, J. Flint, P. Narayan, T. C. T. Michaels, C. M. Dobson, D. Frenkel, T. P. J. Knowles, D. Klenerman, *Sci. Rep.* **2016**, *6*, 28658.

[123] R. R. Murphy, G. Danezis, M. H. Horrocks, S. E. Jackson, D. Klenerman, *Anal. Chem.* **2014**, *86*, 8603–8612.

[124] G. S. Kaminski Schierle, S. van de Linde, M. Erdelyi, E. K. Esbjörner, T. Klein, E. Rees, C. W. Bertoncini, C. M. Dobson, M. Sauer, C. F. Kaminski, *J. Am. Chem. Soc.* **2011**, *133*, 12902–12905.

[125] W. I. Zhang, G. Antonios, A. Rabano, T. A. Bayer, A. Schneider, S. O. Rizzoli, *J. Alzheimers. Dis.* **2015**, *46*, 1007–1020.

[126] S. Fritschi, F. Langer, S. Kaeser, L. Maia, E. Portelius, D. Pinotsi, D. Winkler, W. Maetzler, K. Keyvani, P. Spitzer, et al., *Brain* **2014**, DOI 10.1093/brain/awu255.

[127] J. Brelstaff, B. Ossola, J. J. Neher, T. T. Klingstedt, K. P. R. Nilsson, M. Goedert, M. G. Spillantini, A. M. Tolkovsky, *Front. Neurosci.* **2015**, *9*, 184.

[128] A. Aslund, C. J. Sigurdson, T. Klingstedt, S. Grathwohl, T. Bolmont, D. L. Dickstein, E. Glimsdal, S. Prokop, M. Lindgren, P. Konradsson, et al., *ACS Chem. Biol.* **2009**, *4*, 673–84.

[129] T. Klingstedt, A. Aslund, R. A. Simon, L. B. G. Johansson, J. J. Mason, S. Nyström, P. Hammarström, K. P. R. Nilsson, *Org. Biomol. Chem.* **2011**, *9*, 8356–70.

[130] T. Klingstedt, H. Shirani, K. O. Andreas, N. J. Cairns, C. J. Sigurdson, M. Goedert, K. P. R. Nilsson, **2013**, 10179–10192.

[131] E. Hellstrand, B. Boland, D. M. Walsh, S. Linse, *ACS Chem. Neurosci.* **2010**, *1*, 13–18.

[132] G. Meisl, J. B. Kirkegaard, P. Arosio, T. C. T. Michaels, M. Vendruscolo, C. M. Dobson, S. Linse, T. P. J. Knowles, *Nat. Protoc.* **2016**, *11*, 252–272.

[133] G. Meisl, X. Yang, B. Frohm, T. P. J. Knowles, S. Linse, G. G. Glenner, C. W. Wong, J. Hardy, D. Allsop, T. P. J. Knowles, et al., *Sci. Rep.* **2016**, *6*, 18728.

[134] P. Arosio, T. C. T. Michaels, S. Linse, C. Månsson, C. Emanuelsson, J. Presto, J. Johansson, M. Vendruscolo, C. M. Dobson, T. P. J. Knowles, *Nat. Commun.* **2016**, *7*, 10948.

[135] A. Munke, J. Persson, T. Weiffert, E. De Genst, G. Meisl, P. Arosio, A. Carnerup, C. M. Dobson, M. Vendruscolo, T. P. J. Knowles, et al., *Proc. Natl. Acad. Sci. U. S. A.* **2017**, *114*, 6444–6449.

[136] M. J. Savage, J. Kalinina, A. Wolfe, K. Tugusheva, R. Korn, T. Cash-Mason, J. W. Maxwell, N. G. Hatcher, S. J. Haugabook, G. Wu, et al., *J. Neurosci.* **2014**, *34*, 2884–2897.

[137] R. Jakes, M. G. Spillantini, M. Goedert, *FEBS Lett.* **1994**, *345*, 27–32.

[138] M. G. Spillantini, M. L. Schmidt, V. M. Lee, J. Q. Trojanowski, R. Jakes, M. Goedert, *Nature* **1997**, *388*, 839–840.

[139] M.-C. Chartier-Harlin, J. Kachergus, C. Roumier, V. Mouroux, X. Douay, S. Lincoln, C. Levecque, L. Larvor, J. Andrieux, M. Hulihan, et al., *Lancet* **2004**, *364*, 1167–1169.

[140] A. B. Singleton, M. Farrer, J. Johnson, A. Singleton, S. Hague, J. Kachergus, M. Hulihan, T. Peuralinna, A. Dutra, R. Nussbaum, et al., *Science* **2003**, *302*, 841.

[141] M. H. Polymeropoulos, C. Lavedan, E. Leroy, S. E. Ide, A. Dehejia, A. Dutra, B. Pike, H. Root, J. Rubenstein, R. Boyer, et al., *Science* **1997**, *276*, 2045–2047.

[142] R. Krüger, W. Kuhn, T. Müller, D. Woitalla, M. Graeber, S. Kösel, H. Przuntek, J. T. Epplen, L. Schöls, O. Riess, *Nat. Genet.* **1998**, *18*, 106–108.

[143] J. J. Zarranz, J. Alegre, J. C. Gómez-Esteban, E. Lezcano, R. Ros, I. Ampuero, L. Vidal, J. Hoenicka, O. Rodriguez, B. Atarés, et al., *Ann. Neurol.* **2004**, *55*, 164–173.

[144] C. Proukakis, C. G. Dudzik, T. Brier, D. S. MacKay, J. M. Cooper, G. L. Millhauser, H. Houlden, A. H. Schapira, *Neurology* **2013**, *80*, 1062–1064.

[145] A. P. Kiely, Y. T. Asi, E. Kara, P. Limousin, H. Ling, P. Lewis, C. Proukakis, N. Quinn, A. J. Lees, J. Hardy, et al., *Acta Neuropathol.* **2013**, *125*, 753–769.

[146] P. Pasanen, L. Myllykangas, M. Siitonen, A. Raunio, S. Kaakkola, J. Lyytinen, P. J. Tienari, M. Pöyhönen, A. Paetau, *Neurobiol. Aging* **2014**, *35*, 2180.e1-5.

[147] D. Eliezer, E. Kutluay, R. Bussell, G. Browne, *J. Mol. Biol.* **2001**, *307*, 1061–1073.

[148] R. Bussell, D. Eliezer, *J. Mol. Biol.* **2003**, *329*, 763–778.

[149] H. Han, P. H. Weinreb, P. T. Lansbury, *Chem. Biol.* **1995**, *2*, 163–169.

[150] B. I. Giasson, I. V Murray, J. Q. Trojanowski, V. M. Lee, *J. Biol. Chem.* **2001**, *276*, 2380–2386.

[151] W. Hoyer, D. Cherny, V. Subramaniam, T. M. Jovin, *Biochemistry* **2004**, *43*, 16233–16242.

[152] V. N. Uversky, *J. Biomol. Struct. Dyn.* **2003**, *21*, 211–234.

[153] R. Bussell, D. Eliezer, *J. Biol. Chem.* **2001**, *276*, 45996–46003.

[154] E. A. Greenbaum, C. L. Graves, A. J. Mishizen-Eberz, M. A. Lupoli, D. R. Lynch, S. W. Englander, P. H. Axelsen, B. I. Giasson, *J. Biol. Chem.* **2005**, *280*, 7800–7807.

[155] J. Li, V. N. Uversky, A. L. Fink, *Biochemistry* **2001**, *40*, 11604–11613.

[156] M.-B. Fares, N. Ait-Bouziad, I. Dikiy, M. K. Mbefo, A. Jovičić, A. Kiely, J. L. Holton, S.-J. Lee, A. D. Gitler, D. Eliezer, et al., *Hum. Mol. Genet.* **2014**, *23*, 4491–4509.

[157] D. Ghosh, M. Mondal, G. M. Mohite, P. K. Singh, P. Ranjan, A. Anoop, S. Ghosh, N. N. Jha, A. Kumar, S. K. Maji, *Biochemistry* **2013**, *52*, 6925–6927.

[158] D. Ghosh, S. Sahay, P. Ranjan, S. Salot, G. M. Mohite, P. K. Singh, S. Dwivedi, E. Carvalho, R. Banerjee, A. Kumar, et al., *Biochemistry* **2014**, *53*, 6419–6421.

[159] H. A. Lashuel, B. M. Petre, J. Wall, M. Simon, R. J. Nowak, T. Walz, P. T. Lansbury, *J. Mol. Biol.* **2002**, *322*, 1089–1102.

[160] L. Giehm, D. I. Svergun, D. E. Otzen, B. Vestergaard, *Proc. Natl. Acad. Sci. U. S. A.* **2011**, *108*, 3246–3251.

[161] N. Lorenzen, S. B. Nielsen, A. K. Buell, J. D. Kaspersen, P. Arosio, B. S. Vad, W. Paslawski, G. Christiansen, Z. Valnickova-Hansen, M. Andreasen, et al., *J. Am. Chem. Soc.* **2014**, *136*, 3859–3868.

[162] B. D. van Rooijen, M. M. A. E. Claessens, V. Subramaniam, *FEBS Lett.* **2008**, *582*, 3788–3792.

[163] M. S. Celej, R. Sarroukh, E. Goormaghtigh, G. Fidelio, J.-M. Ruysschaert, V. Raussens, *Biochem. J.* **2012**, DOI 10.1042/BJ20111924.

[164] R. Cappai, S.-L. Leck, D. J. Tew, N. A. Williamson, D. P. Smith, D. Galatis, R. A. Sharples, C. C. Curtain, F. E. Ali, R. A. Cherny, et al., *FASEB J. Off. Publ. Fed. Am. Soc. Exp. Biol.* **2005**, *19*, 1377–1379.

[165] L. Fonseca-Ornelas, C. Schmidt, A. R. Camacho-Zarco, C. O. Fernandez, S. Becker, M. Zweckstetter, *Chemistry* **2017**, *23*, 13010–13014.

[166] D. E. Ehrnhoefer, J. Bieschke, A. Boeddrich, M. Herbst, L. Masino, R. Lurz, S. Engemann, A. Pastore, E. E. Wanker, *Nat. Struct. Mol. Biol.* **n.d.**, *15*, 558–566.

[167] L. Pieri, K. Madiona, R. Melki, *Sci. Rep.* **2016**, *6*, 24526.

[168] M. S. Planchard, S. E. Exley, S. E. Morgan, V. Rangachari, *Protein Sci. A Publ. Protein Soc.* **2014**, *23*, 1369–1379.

[169] K. M. Danzer, D. Haasen, A. R. Karow, S. Moussaud, M. Habeck, A. Giese, H. Kretzschmar, B. Hengerer, M. Kostka, *J. Neurosci.* **2007**, *27*, 9220–9232.

[170] N. Cremades, S. W. Chen, C. M. Dobson, in *Int. Rev. Cell Mol. Biol.* (Ed.: M. Sandal), Academic Press, **2017**, pp. 79–143.

[171] C. D. Borsarelli, L. J. Falomir-Lockhart, V. Ostatná, J. A. Fauerbach, H.-H. Hsiao, H. Urlaub, E. Paleček, E. A. Jares-Erijman, T. M. Jovin, *Free Radic. Biol. Med.* **2012**, *53*, 1004–1015.

[172] W. Ariesandi, C.-F. Chang, T.-E. Chen, Y.-R. Chen, *PLoS One* **2013**, *8*, e53487.

[173] D. M. Williams, T. L. Pukala, *Mass Spectrom. Rev.* **2013**, *32*, 169–187.

[174] A. K. Frimpong, R. R. Abzalimov, V. N. Uversky, I. A. Kaltashov, *Proteins* **2010**, *78*, 714–722.

[175] E. Illes-Toth, M. R. Ramos, R. Cappai, C. Dalton, D. P. Smith, *Biochem. J.* **2015**, *468*, 485–493.

[176] A. S. Phillips, A. F. Gomes, J. M. D. Kalapothakis, J. E. Gillam, J. Gasparavicius, F. C. Gozzo, T. Kunath, C. MacPhee, P. E. Barran, *Analyst* **2015**, *140*, 3070–3081.

[177] C. W. T. Leung, F. Guo, Y. Hong, E. Zhao, R. T. K. Kwok, N. L. C. Leung, S. Chen, N. N. Vaikath, O. M. El-Agnaf, Y. Tang, et al., *Chem. Commun. (Camb).* **2015**, *51*, 1866–1869.

[178] V. B. Kovalska, M. Y. Losytskyy, O. I. Tolmachev, Y. L. Slominskii, G. M. J. Segers-Nolten, V. Subramaniam, S. M. Yarmoluk, *J. Fluoresc.* **2012**, *22*, 1441–1448.

[179] J. I. Gallea, M. S. Celej, *J. Biol. Chem.* **2014**, *289*, 26733–26742.

[180] S. Nath, J. Meuvis, J. J. Hendrix, S. A. Carl, Y. Engelborghs, *Biophys. J.* **2010**, *98*, 1302–1311.

[181] B. D. van Rooijen, K. A. van Leijenhorst-Groener, M. M. a. E. Claessens, V. Subramaniam, *J. Mol. Biol.* **2009**, *394*, 826–833.

[182] M. Kostka, T. Högen, K. M. Danzer, J. Levin, M. Habeck, A. Wirth, R. Wagner, C. G. Glabe, S. Finger, U. Heinzelmann, et al., *J. Biol. Chem.* **2008**, *283*, 10992–11003.

[183] J. Levin, T. Högen, A. S. Hillmer, B. Bader, F. Schmidt, F. Kamp, H. A. Kretzschmar, K. Bötzel, A. Giese, *J. Parkinsons. Dis.* **2011**, *1*, 205–216.

[184] M. Caruana, T. Högen, J. Levin, A. Hillmer, A. Giese, N. Vassallo, *FEBS Lett.* **2011**, *585*, 1113–1120.

[185] E. Sierecki, N. Giles, Q. Bowden, M. E. Polinkovsky, J. Steinbeck, N. Arrioti, D. Rahman, A. Bhumkar, P. R. Nicovich, I. Ross, et al., *Sci. Rep.* **2016**, *6*, 37630.

[186] M. Iljina, G. A. Garcia, M. H. Horrocks, L. Tosatto, M. L. Choi, K. A. Ganzinger, A. Y. Abramov, S. Gandhi, N. W. Wood, N. Cremades, et al., *Proc. Natl. Acad. Sci. U. S. A.* **2016**, *113*, E1206-15.

[187] T. Tokuda, M. M. Qureshi, M. T. Ardah, S. Varghese, S. A. S. S. Shehab, T. Kasai, N. Ishigami, A. Tamaoka, M. Nakagawa, O. M. A. A. El-Agnaf, *Neurology* **2010**, *75*, 1766–1772.

[188] X. Wang, S. Yu, F. Li, T. Feng, *Neurosci. Lett.* **2015**, *599*, 115–119.

[189] K. M. Danzer, L. R. Kranich, W. P. Ruf, O. Cagsal-Getkin, A. R. Winslow, L. Zhu, C. R. Vanderburg, P. J. McLean, *Mol. Neurodegener.* **2012**, *7*, 42.

[190] M. Delenclos, T. Trendafilova, D. R. Jones, S. Moussaud, A.-M. Baine, M. Yue, W. D. Hirst, P. J. McLean, *Front. Neurosci.* **2015**, *9*, 511.

[191] H. Dimant, S. K. Kalia, L. V. Kalia, L. N. Zhu, L. Kibuuka, D. Ebrahimi-Fakhari, N. R. McFarland, Z. Fan, B. T. Hyman, P. J. McLean, *Acta Neuropathol. Commun.* **2013**, *1*, 6.

[192] K. Eckermann, S. Kügler, M. Bähr, *Biochim. Biophys. Acta* **2015**, *1852*, 1658–1664.

[193] R. F. Roberts, R. Wade-Martins, J. Alegre-Abarrategui, *Brain A J. Neurol.* **2015**, *138*, 1642–1657.

[194] N. Plotegher, E. Gratton, L. Bubacco, *Biochim. Biophys. Acta* **2014**, *1840*, 2014–2024.

[195] J. Levin, A. S. Hillmer, T. Högen, P. J. McLean, A. Giese, *Biochem. Biophys. Res. Commun.* **2016**, *477*, 76–82.

[196] N. Cremades, S. I. A. Cohen, E. Deas, A. Y. Abramov, A. Y. Chen, A. Orte, M. Sandal, R. W. Clarke, P. Dunne, F. A. Aprile, et al., *Cell* **2012**, *149*, 1048–59.

[197] W. Hoyer, D. Cherny, V. Subramaniam, T. M. Jovin, *J. Mol. Biol.* **2004**, *340*, 127–139.

[198] S. Thirunavukkuarasu, E. A. Jares-Erijman, T. M. Jovin, *J. Mol. Biol.* **2008**, *378*, 1064–1073.

[199] D. M. Walsh, E. Thulin, A. M. Minogue, N. Gustavsson, E. Pang, D. B. Teplow, S. Linse, *FEBS J.* **2009**, *276*, 1266–81.

[200] S. L. Shammas, G. a. Garcia, S. Kumar, M. Kjaergaard, M. H. Horrocks, N. Shivji, E. Mandelkow, T. P. J. Knowles, E. Mandelkow, D. Klenerman, *Nat. Commun.* **2015**, *6*, 7025.

[201] J. Schnitzbauer, M. T. Strauss, T. Schlichthaerle, F. Schueder, R. Jungmann, *Nat. Protoc.* **2017**, *12*, 1198–1228.

[202] M. H. Horrocks, S. F. Lee, S. Gandhi, M. Iljina, L. Tosatto, C. M. Dobson, D. Klenerman, *Biophys. J.* **2014**, *106*, 268a.

[203] F. Kundel, S. De, P. Flagmeier, M. H. Horrocks, M. Kjaergaard, S. L. Shammas, S. E.

Jackson, C. M. Dobson, D. Klenerman, *ACS Chem. Biol.* **2018**, *13*, 636–646.

[204] F. S. Ruggeri, S. Vieweg, U. Cendrowska, G. Longo, A. Chiki, H. A. Lashuel, G. Dietler, *Sci. Rep.* **2016**, *6*, DOI 10.1038/srep31155.

[205] C. Haass, M. G. Schlossmacher, A. Y. Hung, C. Vigo-Pelfrey, A. Mellon, B. L. Ostaszewski, I. Lieberburg, E. H. Koo, D. Schenk, D. B. Teplow, *Nature* **1992**, *359*, 322–5.

[206] O. M. A. El-Agnaf, S. A. Salem, K. E. Paleologou, M. D. Curran, M. J. Gibson, J. a Court, M. G. Schlossmacher, D. Allsop, *FASEB J.* **2006**, *20*, 419–425.

[207] K. Blennow, H. Hampel, M. Weiner, H. Zetterberg, *Cerebrospinal Fluid and Plasma Biomarkers in Alzheimer Disease*, Nature Publishing Group, **2010**.

[208] B. Olsson, R. Lautner, U. Andreasson, A. Öhrfelt, E. Portelius, M. Bjerke, M. Hölttä, C. Rosén, C. Olsson, G. Strobel, et al., *Lancet Neurol.* **2016**, *15*, 673–684.

[209] H. Zetterberg, K. Blennow, *J. Alzheimer's Dis.* **2013**, *33*, S361–S369.

[210] K. Sämgård, H. Zetterberg, K. Blennow, O. Hansson, L. Minthon, E. Londos, *Int. J. Geriatr. Psychiatry* **2010**, *25*, 403–410.

[211] Å. K. Wallin, K. Blennow, H. Zetterberg, E. Londos, L. Minthon, O. Hansson, *Neurology* **2010**, *74*, 1531–1537.

[212] T. Tapiola, I. Alafuzoff, S. K. Herukka, L. Parkkinen, P. Hartikainen, H. Soininen, T. Pirttilä, *Arch. Neurol.* **2009**, *66*, 382–389.

[213] K. Buerger, M. Ewers, T. Pirttilä, R. Zinkowski, I. Alafuzoff, S. J. Teipel, J. DeBernardis, D. Kerkman, C. McCulloch, H. Soininen, et al., *Brain* **2006**, *129*, 3035–3041.

[214] M. Tabaton, M. G. Nunzi, R. Xue, M. Usiak, L. Autilio-Gambetti, P. Gambetti, *Biochem.Biophys.Res.Commun.* **1994**, *200*, 1598–1603.

[215] W. E. Van Nostrand, S. L. Wagner, W. R. Shankle, J. S. Farrow, M. Dick, J. M. Rozemuller, M. a Kuiper, E. C. Wolters, J. Zimmerman, C. W. Cotman, *Proc. Natl. Acad. Sci. U. S. A.* **1992**, *89*, 2551–2555.

[216] K. Blennow, N. Mattsson, M. Schöll, O. Hansson, H. Zetterberg, *Trends Pharmacol. Sci.* **2015**, *36*, 297–309.

[217] R. Motter, C. Vigo-Pelfrey, D. Kholodenko, R. Barbour, K. Johnson-Wood, D.

Galasko, L. Chang, B. Miller, C. Clark, R. Green, *Ann. Neurol.* **1995**, *38*, 643–648.

[218] A. M. Fagan, M. A. Mintun, R. H. Mach, S. Y. Lee, C. S. Dence, A. R. Shah, G. N. LaRossa, M. L. Spinner, W. E. Klunk, C. A. Mathis, et al., *Ann. Neurol.* **2006**, *59*, 512–519.

[219] J. Dumurgier, S. Schraen, A. Gabelle, O. Vercruysse, S. Bombois, J.-L. Laplanche, K. Peoc'h, B. Sablonnière, K. V Kastanenka, C. Delaby, et al., *Alzheimers. Res. Ther.* **2015**, *7*, 1–9.

[220] P. Lewczuk, N. Lelental, P. Spitzer, J. M. Maler, J. Kornhuber, *J. Alzheimer's Dis.* **2014**, *43*, 183–191.

[221] N. Andreasen, C. Hesse, P. Davidsson, L. Minthon, a Wallin, B. Winblad, H. Vanderstichele, E. Vanmechelen, K. Blennow, *Arch. Neurol.* **1999**, *56*, 673–80.

[222] A. Olsson, H. Vanderstichele, N. Andreasen, G. De Meyer, A. Wallin, B. Holmberg, L. Rosengren, E. Vanmechelen, K. Blennow, *Clin. Chem.* **2005**, *51*, 336–345.

[223] H. Zetterberg, U. Andreasson, O. Hansson, G. Wu, S. Sankaranarayanan, M. E. Andersson, P. Buchhave, E. Londos, R. M. Umek, L. Minthon, et al., *Arch. Neurol.* **2008**, *65*, 1102–1107.

[224] J. Wiltfang, H. Esselmann, M. Bibl, A. Smirnov, M. Otto, S. Paul, B. Schmidt, H. W. Klafki, M. Maler, T. Dyrks, et al., *J. Neurochem.* **2002**, *81*, 481–496.

[225] A. Leinenbach, J. Pannee, T. Dülffer, A. Huber, T. Bittner, U. Andreasson, J. Gobom, H. Zetterberg, U. Kobold, E. Portelius, et al., *Clin. Chem.* **2014**, *60*, 987–994.

[226] O. Hansson, J. Seibyl, E. Stomrud, H. Zetterberg, J. Q. Trojanowski, T. Bittner, V. Lifke, V. Corradini, U. Eichenlaub, R. Batrla, et al., *Alzheimer's Dement.* **2018**, DOI 10.1016/j.jalz.2018.01.010.

[227] B. Olsson, R. Lautner, U. Andreasson, A. Öhrfelt, E. Portelius, M. Bjerke, M. Hölttä, C. Rosén, C. Olsson, G. Strobel, et al., *Lancet Neurol.* **2016**, *15*, 673–684.

[228] W. E. Klunk, H. Engler, A. Nordberg, Y. Wang, G. Blomqvist, D. P. Holt, M. Bergström, I. Savitcheva, G. F. Huang, S. Estrada, et al., *Ann. Neurol.* **2004**, *55*, 306–319.

[229] C. R. Jack, J. R. Barrio, V. Kepe, *Acta Neuropathol.* **2013**, *126*, 643–657.

[230] C. C. Rowe, S. Pejoska, R. S. Mulligan, G. Jones, J. G. Chan, S. Svensson, Z. Cselenyi,

C. L. Masters, V. L. Villemagne, *J. Nucl. Med.* **2013**, *54*, 880–886.

[231] B. J. Bacskai, M. P. Frosch, S. H. Freeman, S. B. Raymond, J. C. Augustinack, K. A. Johnson, M. C. Irizarry, W. E. Klunk, C. A. Mathis, S. T. DeKosky, et al., *Arch. Neurol.* **2007**, *64*, 431–434.

[232] A. Lockhart, J. R. Lamb, T. Osredkar, L. I. Sue, J. N. Joyce, L. Ye, V. Libri, D. Leppert, T. G. Beach, *Brain* **2007**, *130*, 2607–2615.

[233] M. D. Ikonomovic, W. E. Klunk, E. E. Abrahamson, C. A. Mathis, J. C. Price, N. D. Tsopelas, B. J. Lopresti, S. Ziolko, W. Bi, W. R. Paljug, et al., *Brain* **2008**, *131*, 1630–1645.

[234] S. Hall, Y. Surova, A. Öhrfelt, K. Blennow, H. Zetterberg, O. Hansson, O. Hansson, *Mov. Disord.* **2016**, *31*, 898–905.

[235] B. Mollenhauer, C. J. Caspell-Garcia, C. S. Coffey, P. Taylor, L. M. Shaw, J. Q. Trojanowski, A. Singleton, M. Frasier, K. Marek, D. Galasko, et al., *Neurology* **2017**, *89*, 1959–1969.

[236] N. K. Majbour, N. N. Vaikath, P. Eusebi, D. Chiasserini, M. Ardah, S. Varghese, M. E. Haque, T. Tokuda, P. Auinger, P. Calabresi, et al., *Mov. Disord.* **2016**, *31*, 1535–1542.

[237] T. Stewart, C. Liu, C. Ginghina, K. C. Cain, P. Auinger, B. Cholerton, M. Shi, J. Zhang, *Am. J. Pathol.* **2014**, *184*, 966–975.

[238] S. F. Moore, R. a. Barker, *Park. Relat. Disord.* **2014**, *20*, S104–S107.

[239] M. Fändrich, *J. Mol. Biol.* **2012**, *421*, 427–440.

[240] S. Ceru, S. J. Kokalj, S. Rabzelj, M. Skarabot, I. Gutierrez-Aguirre, N. Kopitar-Jerala, G. Anderluh, D. Turk, V. Turk, E. Zerovnik, *Amyloid* **2008**, *15*, 147–59.

[241] N. Le Bastard, P. P. De Deyn, S. Engelborghs, *Clin. Chem.* **2015**, *61*, 734–43.

[242] J. Klener, K. Hofbauerová, A. Bartoš, J. Říčný, D. Rípová, V. Kopecký, *Clin. Chem. Lab. Med.* **2014**, *52*, 657–64.

[243] J. B. Toledo, H. Zetterberg, A. C. van Harten, L. Glodzik, P. Martinez-Lage, L. Bocchio-Chiavetto, L. Rami, O. Hansson, R. Sperling, S. Engelborghs, et al., *Brain* **2015**, *138*, awv199.

[244] M. Calero, A. Rostagno, E. Matsubara, B. Zlokovic, B. Frangione, J. Ghiso, *Microsc. Res. Tech.* **2000**, *50*, 305–15.

[245] J.-C. Lambert, S. Heath, G. Even, D. Campion, K. Sleegers, M. Hiltunen, O. Combarros, D. Zelenika, M. J. Bullido, B. Tavernier, et al., *Nat. Genet.* **2009**, *41*, 1094–1099.

[246] D. Harold, R. Abraham, P. Hollingworth, R. Sims, A. Gerrish, M. L. Hamshere, J. S. Pahwa, V. Moskvina, K. Dowzell, A. Williams, et al., *Nat. Genet.* **2009**, *41*, 1088–93.

[247] P. Narayan, A. Orte, R. W. Clarke, B. Bolognesi, S. Hook, K. a Ganzinger, S. Meehan, M. R. Wilson, C. M. Dobson, D. Klenerman, *Nat. Struct. Mol. Biol.* **2011**, *19*, 79–83.

[248] R. S. Desikan, W. K. Thompson, D. Holland, C. P. Hess, J. B. Brewer, H. Zetterberg, K. Blennow, O. A. Andreassen, L. K. McEvoy, B. T. Hyman, et al., *JAMA Neurol.* **2014**, *71*, 180–7.

[249] J. J. Yerbury, S. Poon, S. Meehan, B. Thompson, J. R. Kumita, C. M. Dobson, M. R. Wilson, *FASEB J.* **2007**, *21*, 2312–2322.

[250] K. D. Van Dijk, W. Jongbloed, J. A. Heijst, C. E. Teunissen, H. J. Groenewegen, H. W. Berendse, W. D. J. van de Berg, R. Veerhuis, *Park. Relat. Disord.* **2013**, *19*, 1079–1083.

[251] C. L. Maarouf, T. G. Beach, C. H. Adler, H. A. Shill, M. N. Sabbagh, T. Wu, D. G. Walker, T. A. Kokjohn, A. E. Roher, A. P. Consortium, *Neurol. Res.* **2012**, *34*, 669–676.

[252] G. N. Yin, H. W. Lee, J. Y. Cho, K. Suk, *Brain Res.* **2009**, *1265*, 158–170.

[253] A. M. Lidström, C. Hesse, L. Rosengren, P. Fredman, P. Davidsson, *J. Alzheimer's Dis.* **2001**, *3*, 435–442.

[254] H. P. Vranová, J. Mareš, M. Nevrlý, D. Stejskal, J. Zapletalová, P. Hluštík, P. Kaňovský, *J. Neural Transm.* **2010**, *117*, 1177–1181.

[255] S. Salloway, R. Sperling, N. C. Fox, K. Blennow, W. Klunk, M. Raskind, M. Sabbagh, L. S. Honig, A. P. Porsteinsson, S. Ferris, et al., *N. Engl. J. Med.* **2014**, *370*, 322–333.

[256] R. Vandenberghe, J. O. Rinne, M. Boada, S. Katayama, P. Scheltens, B. Vellas, M. Tuchman, A. Gass, J. B. Fiebach, D. Hill, et al., *Alzheimers. Res. Ther.* **2016**, *8*, 18.

[257] D. M. Walsh, I. Klyubin, J. V Fadeeva, W. K. Cullen, R. Anwyl, M. S. Wolfe, M. J. Rowan, D. J. Selkoe, *Nature* **2002**, *416*, 535–539.

[258] I. Klyubin, V. Betts, A. T. Welzel, K. Blennow, H. Zetterberg, A. Wallin, C. A. Lemere, W. K. Cullen, Y. Peng, T. Wisniewski, et al., *J. Neurosci.* **2008**, *28*, 4231–4237.

[259] J. J. Yerbury, M. R. Wilson, *Cell Stress Chaperones* **2010**, *15*, 115–121.

[260] A. Drews, J. Flint, N. Shivji, P. Jönsson, D. Wirthensohn, E. De Genst, C. Vincke, S. Muyldermans, C. Dobson, D. Klenerman, *Sci. Rep.* **2016**, *6*, DOI 10.1038/srep31910.

[261] T. Yang, T. T. O'Malley, D. Kanmert, J. Jerecic, L. R. Zieske, H. Zetterberg, B. T. Hyman, D. M. Walsh, D. J. Selkoe, *Alzheimer's Res. Ther.* **2015**, *7*, DOI 10.1186/s13195-015-0100-y.

[262] B. Babakinejad, P. Jönsson, A. López Córdoba, P. Actis, P. Novak, Y. Takahashi, A. Shevchuk, U. Anand, P. Anand, A. Drews, et al., *Anal. Chem.* **2013**, *85*, 9333–9342.

[263] H. P. Vranová, E. Hényková, M. Kaiserová, K. Menšíková, M. Vaštík, J. Mareš, P. Hluštík, J. Zapletalová, M. Strnad, D. Stejskal, et al., *J. Neurol. Sci.* **2014**, *343*, 120–124.

[264] L. A. Miles, G. A. N. Crespi, L. Doughty, M. W. Parker, *Sci. Rep.* **2013**, *3*, DOI 10.1038/srep01302.

[265] E. Liu, M. E. Schmidt, R. Margolin, R. Sperling, R. Koeppe, N. S. Mason, W. E. Klunk, C. A. Mathis, S. Salloway, N. C. Fox, et al., *Neurology* **2015**, *85*, 692–700.

[266] J. A. Varela, M. Rodrigues, S. De, P. Flagmeier, S. Gandhi, C. M. Dobson, D. Klenerman, S. F. Lee, *Angew. Chemie Int. Ed.* **2018**, DOI 10.1002/anie.201710779.

[267] W. F. Goure, G. A. Krafft, J. Jerecic, F. Hefti, *Alzheimer's Res. Ther.* **2014**, *6*, DOI 10.1186/alzrt272.

[268] I. Nasir, S. Linse, C. Cabaleiro-Lago, *ACS Chem. Neurosci.* **2015**, *6*, 1436–1444.

[269] R. Silvers, M. T. Colvin, K. K. Frederick, A. C. Jacavone, S. Lindquist, S. Linse, R. G. Griffin, *Biochemistry* **2017**, *56*, 4850–4859.

[270] V. H. Finder, I. Vodopivec, R. M. Nitsch, R. Glockshuber, *J. Mol. Biol.* **2010**, *396*, 9–18.

[271] P. Arosio, T. Cedervall, T. P. J. Knowles, S. Linse, *Anal. Biochem.* **2016**, *504*, 7–13.

[272] D. Sehlin, H. Englund, B. Simu, M. Karlsson, M. Ingelsson, F. Nikolajeff, L. Lannfelt, F. E. Pettersson, *PLoS One* **2012**, *7*, e32014.

[273] R. V Ward, K. H. Jennings, R. Jepras, W. Neville, D. E. Owen, J. Hawkins, G. Christie, J. B. Davis, A. George, E. H. Karran, et al., *Biochem. J.* **2000**, *348 Pt 1*, 137–44.

[274] I. Benilova, E. Karran, B. De Strooper, *Nat. Neurosci.* **2012**, *15*, 349–57.

[275] P. Cizas, R. Budvytyte, R. Morkuniene, R. Moldovan, M. Broccio, M. Lösche, G. Niaura, G. Valincius, V. Borutaite, *Arch. Biochem. Biophys.* **2010**, *496*, 84–92.

[276] S. Maeda, N. Sahara, Y. Saito, M. Murayama, Y. Yoshiike, H. Kim, T. Miyasaka, S. Murayama, A. Ikai, A. Takashima, *Biochemistry* **2007**, *46*, 3856–3861.

[277] A. T. Petkova, R. D. Leapman, Z. Guo, W.-M. Yau, M. P. Mattson, R. Tycko, *Science* **2005**, *307*, 262–5.

[278] M. T. Heneka, M. J. Carson, J. El Khoury, G. E. Landreth, F. Brosseron, D. L. Feinstein, A. H. Jacobs, T. Wyss-Coray, J. Vitorica, R. M. Ransohoff, et al., *Lancet Neurol.* **2015**, *14*, 388–405.

[279] C. H. Latta, H. M. Brothers, D. M. Wilcock, *Neuroscience* **2015**, *302*, 103–111.

[280] K. Ji, G. Akgul, L. P. Wollmuth, S. E. Tsirka, *PLoS One* **2013**, *8*, e56293.

[281] M. E. Bamberger, M. E. Harris, D. R. McDonald, J. Husemann, G. E. Landreth, *J. Neurosci.* **2003**, *23*, 2665–2674.

[282] D. M. Paresce, R. N. Ghosh, F. R. Maxfield, *Neuron* **1996**, *17*, 553–65.

[283] C. R. Stewart, L. M. Stuart, K. Wilkinson, J. M. Van Gils, J. Deng, A. Halle, K. J. Rayner, L. Boyer, R. Zhong, W. A. Frazier, et al., *Nat. Immunol.* **2010**, *11*, 155–161.

[284] Y. Liu, S. Walter, M. Stagi, D. Cherny, M. Letiembre, W. Schulz-Schaeffer, H. Heine, B. Penke, H. Neumann, K. Fassbender, *Brain* **2005**, *128*, 1778–1789.

[285] F. J. Sheedy, A. Grebe, K. J. Rayner, P. Kalantari, B. Ramkhelawon, S. B. Carpenter, C. E. Becker, H. N. Ediriweera, A. E. Mullick, D. T. Golenbock, et al., *Nat. Immunol.* **2013**, *14*, 812–820.

[286] J. B. El Khoury, K. J. Moore, T. K. Means, J. Leung, K. Terada, M. Toft, M. W. Freeman, A. D. Luster, *J. Exp. Med.* **2003**, *197*, 1657–1666.

[287] H. Akiyama, S. Barger, S. Barnum, B. Bradt, J. Bauer, G. M. Cole, N. R. Cooper, P. Eikelenboom, M. Emmerling, B. L. Fiebich, et al., *Neurobiol. Aging* **2000**, *21*, 383–421.

[288] K. Yamamoto, T. Arakawa, N. Ueda, S. Yamamoto, *J.Biol.Chem.* **1995**, *270*, 31315–31320.

[289] J. R. Cardinaux, I. Allaman, P. J. Magistretti, *Glia* **2000**, *29*, 91–97.

[290] A. C. McKee, N. W. Kowall, J. S. Schumacher, M. F. Beal, *Amyloid* **1998**, *5*, 1–9.

[291] S. W. Barger, A. D. Harmon, *Nature* **1997**, *388*, 878–881.

[292] S. W. Barger, D. Horster, K. Furukawa, Y. Goodman, J. Krieglstein, M. P. Mattson, *Proc. Natl. Acad. Sci.* **1995**, *92*, 9328–9332.

[293] E. Tarkowski, N. Andreasen, A. Tarkowski, K. Blennow, *J. Neurol. Neurosurg. Psychiatry* **2003**, *74*, 1200–1205.

[294] G. S. Paranjape, L. K. Gouwens, D. C. Osborn, M. R. Nichols, *ACS Chem. Neurosci.* **2012**, *3*, 302–311.

[295] A. Aslund, C. J. Sigurdson, T. Klingstedt, S. Grathwohl, T. Bolmont, D. L. Dickstein, E. Glimsdal, S. Prokop, M. Lindgren, P. Konradsson, et al., *ACS Chem. Biol.* **2009**, *4*, 673–84.

[296] W. Qi, A. Zhang, T. A. Good, E. J. Fernandez, *Biochemistry* **2009**, *48*, 8908–8919.

[297] H. Stark, *Methods Enzymol.* **2010**, *481*, 109–126.

[298] L. M. Jungbauer, C. Yu, K. J. Laxton, M. J. LaDu, *J. Mol. Recognit.* **2009**, *22*, 403–13.

[299] S.-Y. Zhang, E. Jouanguy, S. Ugolini, A. Smahi, G. Elain, P. Romero, D. Segal, V. Sancho-Shimizu, L. Lorenzo, A. Puel, et al., *Science* **2007**, *317*, 1522–7.

[300] A. W. P. Fitzpatrick, G. T. Debelouchina, M. J. Bayro, D. K. Clare, M. A. Caporini, V. S. Bajaj, C. P. Jaroniec, L. Wang, V. Ladizhansky, S. A. Müller, et al., *Proc. Natl. Acad. Sci. U. S. A.* **2013**, *110*, 5468–73.

[301] S. E. Nasrabady, B. Rizvi, J. E. Goldman, A. M. Brickman, *Acta Neuropathol. Commun.* **2018**, *6*, 22.

10 Table of Tables

11 Table of Figures